1-1-2017

Time-Dependent Spectropolarimetric Modeling of Interacting Core Collapse Supernovae

Leah N. Huk
University of Denver

Time-Dependent Spectropolarimetric Modeling of Interacting Core Collapse Supernovae

A Dissertation

Presented to

the Faculty of Natural Sciences and Mathematics

University of Denver

In Partial Fulfillment

of the Requirements for the Degree

Doctor of Philosophy

by

Leah N. Huk

June 2017

Advisor: Prof. Jennifer L. Hoffman

Author: Leah N. Huk
Title: Time-Dependent Spectropolarimetric Modeling of Core Collapse Supernovae
Advisor: Prof. Jennifer L. Hoffman
Degree Date: June 2017

Abstract

Explosive deaths of massive stars in core collapse supernovae are rare events that are only observed with any frequency at large intergalactic distances. This makes identification of progenitors difficult and massive star evolution a challenge to pin down. This dissertation addresses the question of how the properties of the circumstellar environment around supernovae can be used to identify progenitors via their mass loss history. Massive stars all lose mass through a variety of mechanisms that are characteristic of their mass, age, and binarity. This gives rise to a wide range of circumstellar environments which with supernovae may interact, producing multi-component emission lines with polarization profiles that are degenerately dependent on the properties of the medium and change over time. My dissertation approaches this problem computationally by modeling the polarized Hα emission lines for CSM with combinations of different morphologies and optical parameters.

My dissertation work fits these models against the polarized spectra of the Type IIn SNe 1997eg and 2010jl as a tool to diagnose their CSM properties and and constrain their mass loss histories. I find that both of these supernovae are preferentially fit by models with inclinations of close to 90° and high shock luminosities. This suggests that an inclination effect may be a requirement in whether an interacting SNe presents observationally as a IIn.

Acknowledgements

There are many people I wish to thank for their help and guidance: my committee members and all our colleagues at the University of Arizona and the SNSPOL team for their participation, my adviser Dr. Jennifer Hoffman for her seemingly endless patience and for being such a great teacher, Manisha Shrestha and Andrew Fullard for aiding me in learning Fortran and developing the model code, Charee Peters, Dr. Keivan Stassun, and Dr. Cathy Durso for their roles in the development of statistical methods. I also thank Taylor Firman, Jonathan Huihui, Justin Petucci, and their advisers Dr. Kingshuk Ghosh and Dr. Mercedes Calbi for sharing their computing resources, and Ben Fotovich and Barbara Stephen for always being so kind and helpful. I would like to finish giving professional thanks by acknowledging Dr. Douglas Leonard for his mentoring and belief in me, though I was not his student, and his aid in my pursuit of graduate school.

In the personal realm, I would like to thank my many wonderful friends for their continued love and presence: Alex Dixon, Alisha Yackley Nethero, Cristina Terracciano, Tristan Wolfe, and Rachel Bennet for their priceless friendship and camaraderie; if there's any one thing I'm grateful for in this graduate school experience, its having made them as friends. Lastly, I wish to thank my family: the Griffith and Baldwin families, my grandparents, my sister Rachel, and my father Geoffrey for their support throughout my life and over the past few years. Most importantly, I'm eternally grateful to my beloved husband Shawn and son Sawyer. During the darkest times, I persevered for you.

Table of Contents

List of Tables

List of Figures

List of Abbreviations

BSG	Blue Supergiant
CCSN	Core Collapse Supernova
CSM	Circumstellar Material
DU	University of Denver
FWHM	Full Width at Half Maximum
ISP	Interstellar Polarization
LBV	Luminous Blue Variable
LRIS	Low Resolution Imaging Spectrometer
RLOF	Roche-Lobe Overflow
RSG	Red Supergiant
SN	Supernova
SNR	Signal-to-noise Ratio
SNSPOL	Supernova Spectropolarimetry (Project)
TACC	Texas Advanced Computing Center
UPGMC	Unweighted Pair Group Method with Centroid averaging
WR	Wolf-Rayet
XSEDE	Extreme Science and Engineering Discovery Environment
YSG	Yellow Supergiant

Chapter 1

Introduction

1.1 Background

Stars in our universe are powered by the conversion of lighter atomic nuclei to heavier ones via fusion processes in their cores, transforming and releasing the energy as light at rates that increase with their initial mass. Throughout the main sequence lifetime, radiation released by these reactions creates pressure that balances against the force of gravity and maintains hydrostatic equilibrium, only ceasing once all the available elemental fuel in the core is depleted. For a low-mass star like our sun, broken hydrostatic equilibrium heralds a slow and gentle death as its outer layers, light in weight and sparse from radial growth during late evolution, escape from the pull of gravity and float freely away. For the most massive stars ($\geq 8M_{\odot}$) however, the consequences are catastrophic (Arnett 1969; Tinsley 1975).

Stars of at least $10M_{\odot}$ are able to generate temperatures and pressures high enough to burn silicon into nickel, which radioactively decays into iron (Heger et al. 2003). These two metals have higher nuclear binding energies then any other element and cannot be fused as an energy source (Fewell 1995). An inert nickel and iron core grows as silicon burns in a shell around it and heralds the stars imminent

demise. Dropping radiation pressure frees gravity to compress the core to electron degeneracy under the weight of the envelope. When the degenerate mass of the inner core exceeds the Chandrasekhar limit of $\sim 1.4 M_{\odot}$ it is no longer able to support the weight of the layers above it and collapses so quickly, with the outer core descending atop it, that the envelope does not have time to respond. The implosion ceases only when the inner core is crushed to the point of neutron degeneracy, at which point the outer core layers rebound and form a shock front that stalls for a moment and then accelerates, violently ejecting the envelope. This event is called a Core Collapse Supernova (CCSN).

Among the brightest and most energetic phenomena observed by astronomers, the nuclei synthesized in the explosion and core of the progenitor and the solid dusts that coalesce in the ejected remains are carried outward by the shock and distributed throughout the surrounding regions of space. A nearby gas cloud might be triggered by the disturbance and, freshly enriched with heavier elements, condense into a nursery of new star and planet formation. In this way, CCSNe do not solely mark the destructive deaths of massive stars; they are a required part of the cosmic life cycle of matter, vital to the formation of stars, planets and organic life. Our ability to observe them in distant galaxies provides a way for astronomers to study stellar evolution at large distances and into the cosmological reaches of the past.

Studying CCSNe is important for many reasons, and yet our understanding of these events is still far from complete. What exact mechanisms enable the rebound shock to accelerate and trigger the explosion after stalling under the weight of the outer core? How do the conditions that initialize core collapse vary among massive stars of different properties and in different environments? What exact roles do initial mass, multiplicity, and metallicity have on the life of a massive star that influence when in its evolution it will collapse. How do they determine what the observable properties of the explosion will look like? The answers to these questions

have major implications for our understanding of stellar and galactic evolution and therefore cosmology as a whole, but are unfortunately difficult to answer because massive stars comprise only a very small fraction of all stars in existence. Examining massive star death at a distance provides additional sources of information about this population that we otherwise would not have access to.

1.2 Core Collapse Supernovae

1.2.1 CCSN classification and progenitor identification

The current classification scheme describing CCSNe hinges primarily on the behavior of these objects light curves and the characteristics of their spectra at maximum light (Filippenko 1997; Turatto 2003; Turatto et al. 2007). Divisions into groups were first defined by the most obvious spectral differences such as the presence or absence of hydrogen, helium, silicon, etc, and relative amounts of energy released over time as seen in their light curves (Baade and Zwicky 1934; Zwicky 1964). By the middle of the 20th century it was widely accepted that gravitational core collapse of massive stars were the mechanism behind the events (Burbidge et al. 1957). Lack of understanding about the underlying physical and environmental properties leading to such wide CCSNe variation led to a convoluted taxonomic system based on properties of their observed light without clear or consistent association with their cause. Figure 1.1 provides a basic overview of the criteria for each SN type and highlights how the taxonomic organization developed as a side effect of the history of observation.

The general hypothesis that SNe types might each be constrained to arise from a very specific progenitor star type dominated the field for quite some time. Older single-star evolution models for stars of initial mass in the 8–25 $M_{\odot}$ range indicated they should undergo core collapse and explode during a red supergiant (RSG) phase,

which is observed to be true in the case of II-P and II-L events (Smartt 2009). SNe II-P have been definitively linked to red supergiants with initial masses in the range of 8–18 $M_{\odot}$ (Van Dyk et al. 2003). SNe II-L are associated with red and yellow supergiants occupying a narrow band of mass just above the SN II-P progenitors, approximately 18–23 $M_{\odot}$; in this range, faster stellar winds cause greater mass loss than in the lower-mass group (Elias-Rosa et al. 2010; Smith et al. 2011a).

However, the principle that stellar mass and age of the progenitor alone are the sole driving factors influencing explosion observables is misleading when applied to interacting, peculiar, transitional, and hydrogen deficient CCSN types. Discovery of the progenitor of SN 1987A, a *blue* supergiant progenitor of $\sim 18M_{\odot}$, defied modeling predictions by exploding in a post-RSG phase and complicated our understanding of massive star evolution (Arnett et al. 1989). The progenitor is believed to have had mass–loss rates higher then predicted for its mass due to unusually high metallicity and a potential binary companion, factors not accounted for in the models successful for predicting II-P and II-L progenitors (Smartt 2009). In the case of transitional and hydrogen deficient SNe, mass estimates, wind speeds, and total mass loss rates among members vary widely enough that they elude association with a single progenitor type. For transitional IIb and at least *some* fraction of Ibc SNe, low abundances or complete lack of hydrogen combined with low measured wind speeds and low mass loss rates can only be explained by Roche-Lobe Overflow (RLOF) mass loss from a binary companion (Claeys et al. 2011). This agrees with the progenitor detection of the type IIb SN 1993J, confirmed as a K-type red supergiant with a binary companion (Aldering et al. 1994; Van Dyk et al. 2002). For other Ib and Ic events a single very massive evolved Wolf-Rayet (WR) star fits the progenitor requirements when wind-driven mass loss is extreme enough to remove all of the outer envelope, but only if it is associated with a high-metallicity host galaxy or if it survives an efficient eruptive LBV phase. Otherwise, SNe Ic also

necessitate a binary companion to strip the envelope to such a severe degree (Smith et al. 2011a).

The combined effects of multiplicity, metallicity, cluster membership, galactic location, orientation and inclination, rotation, and magnetic fields can all have a large but non-linear impact on a progenitors mass loss behavior that alters its evolution and explosion characteristics and how they might be perceived. Initial mass and evolutionary age alone are not enough and clearly there are a great many environmental and congenital progenitor parameters that should be considered when attempting to account for the differences our empirical taxonomy does not adequately address. (Vink et al. 2005)

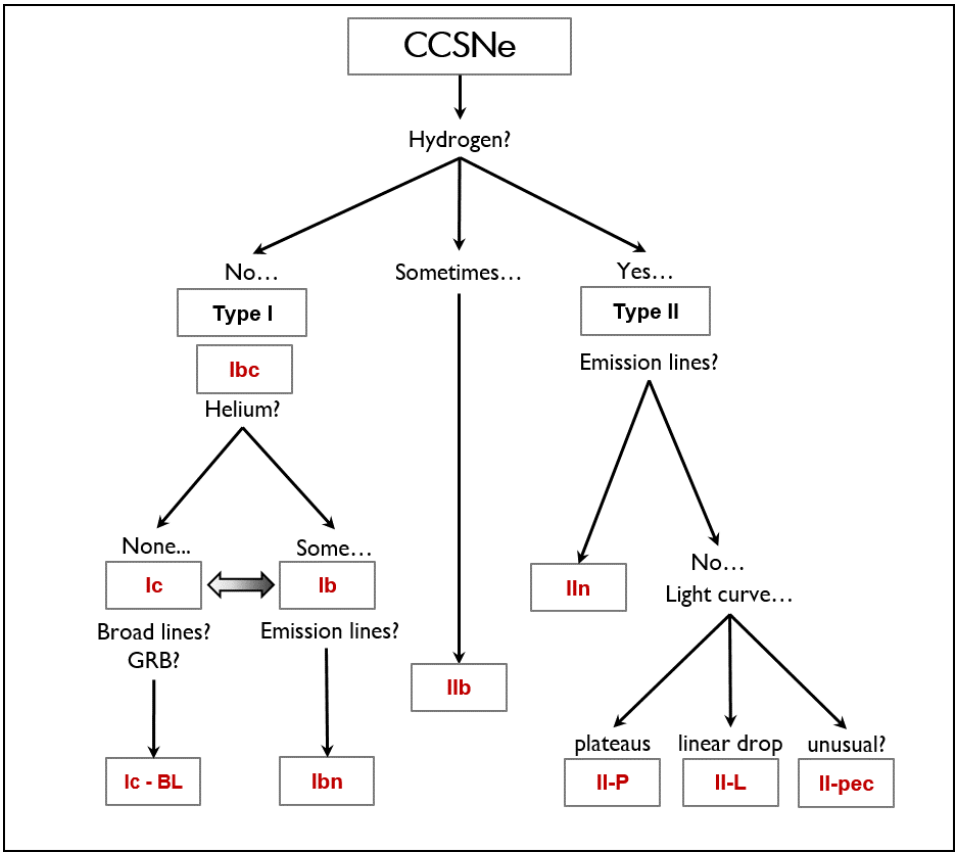

Figure 1.1: The traditional classification scheme for core collapse supernovae evolved from the identification of characteristics in the observed spectra and light curves, based on figure from Turatto et al. (2003).

1.2.2 Interacting CCSNe and the Type IIn classification

Supernovae that interact with pre-existing circumstellar material (CSM) are particularly prone to misclassification and misinterpretation. Interacting SNe, more traditionally labeled in the catch-all class of "SNe IIn," are a highly heterogeneous group defined by a lack of absorption lines in the spectrum and the presence of strong, narrow emission lines, particularly of hydrogen, which are evidence for the interaction between the ejecta and some surrounding CSM (Filippenko 1997; Chugai et al. 2004). As with the other SN types, many years of research were spent focused on whether or not a single progenitor star channel (in this case, luminous blue variables stars or LBVs) is solely responsible for producing IIn events (Gal-Yam et al. 2005; Dwarkadas 2011; Smith et al. 2011b). LBVs were confirmed progenitors for the IIne SN 2005gl (Gal-Yam et al. 2007), SN 2010jl. Bilinski et al. (2015) looked at constraining outburst properties of IIn progenitors. The added difficulty with diagnosing the origins of classic IIn's is that the interaction signals from the CSM and shock often persist over times that exceed the luminosity lifetime of the SN hidden behind them.

Collision of the ejecta with the CSM creates a compressional disturbance in the form of a shock region that develops when the speed of the ejecta ($\sim 1 - 3 \times 10^3$ km s^{-1}) is greater then the sound speed of the medium ($\sim$ 20 km s^{-1}) (cite: Owocki2008, Cassinelli?) The spectra observed in SNe type IIn are driven by the dynamics of this shock structure and its boundary regions, causing wide variation in the shape, strength, and persistence of the emission line components over time, as well as in the rise and dropoff behavior of their light curves (Miller et al. 2010; Arcavi et al. 2012; Kiewe et al. 2012). At the earliest times, the CSM undergoes initial photoionization, which renders it optically thick. The resulting "photosphere" is seen as a smooth, blue continuum populated with emission lines having two components: a broad Lorentzian base caused by electron scattering of

line photons moving through the optically thick region, and narrow cores from line photons of the photoionized gas above. [**I think you should define "broad" and "narrow" in terms of velocities –jlh**] At peak luminosity, the photosphere moves backward into the shock region, where the fast-moving shocked gas radiates strong intermediate width line components with velocities of $1 - 3 \times 10^3$ km s^{-1}.

The advent of long time-domain observations of individual events and the increasing sensitivity of multi-wavelength spectroscopy has allowed for better and more complete observations of interaction behavior. This has muddied the criteria for classifying SNe that show interaction. At least one SN of every other subtype has been observed to show signatures of interaction at some time during its evolution (Patat et al. 2001; Smith et al. 2011a). The type II-P SN 2007od studied by Inserra et al. (2011) and II-L SN 2013ej studied by Bose et al. (2015) both had interaction signatures that were weak and fleeting. In contrast, the strength of a developing post-discovery interaction phase observed in SN 2001em by Schinzel et al. (2009) was dramatic and persistent enough to completely alter its classification from a Ib/c to a IIn. There are also SNe classified as IIn where interaction is weak enough that a spectral resemblance to other subtypes is apparent. SN 2005ip was a low-luminosity IIn that aside from the emission lines more closely resembled a II-L spectrum than it did other SNe IIn (Smith et al. 2009). These cases are all part of a building mountain of evidence that a stand alone class of interacting SNe with explosion dynamics and progenitors inherently unique from other SNe is a flawed view.

All massive stars undergo some degree of mass loss driven by winds, outbursts, or stripping by a companion. All CCSNe are therefore surrounded by at least some gas expelled prior to explosion. Enough evidence now exists to suggest that interaction signatures are a continuous environmental factor that can occur in conjunction with any kind of SNe progenitor. Rather then form their own class, interaction should

be an optional taxonomic designation with the ability to be added piecewise to any other SNe type for which it happens to be present (Smith 2016).

1.2.3 Massive Star Progenitors

The mass loss behavior of a star can be characterized by its rate ($M_\odot$ yr^{-1}) and velocity (km s^{-1}). Different classes of massive progenitors occupy distinct regions of the mass loss parameter space When the known ranges of these quantities are plotted for each, as show in 1.2 from Smith (2016). One can therefore infer an identification of a massive star if estimates of these values can be made.

As all massive stars lose mass in one or more of these mechanisms, CCSNe with accompanying interaction signature can be produced by any massive progenitor that accumulates sufficient mass loss prior to explosion. BSG and LBV stars are simply more likely to produce the conditions necessary for strong interaction as opposed to massive stars of other kinds. WR, RSG and YHG stars with enhanced wind mass loss or binary companions are capable of producing the more tenuous or extended mass loss behavior that is characteristic of weak or transitionally interacting events (Smith 2016).

Progenitor identification for all SNe is already difficult without precise pre-explosion images. As these images do not readily exist, most of the time inferences are drawn using only the spectrum and light curves, as discussed previously. Interpreting observations of strongly interacting type IIn SNe is doubly so, with the knowledge that a wide range of progenitor scenarios can produce interaction and that the underlying ejecta is obscured by it. Recent modeling by Leloudas et al. (2015) attempted to deconvolve the emission signal from that of the underlying photosphere, finding that correct classification for SNe II-P is possible when the emission flux is no more than 2 magnitudes greater then that of the ejecta but this still does not help address cases where interaction is very strong and bright.

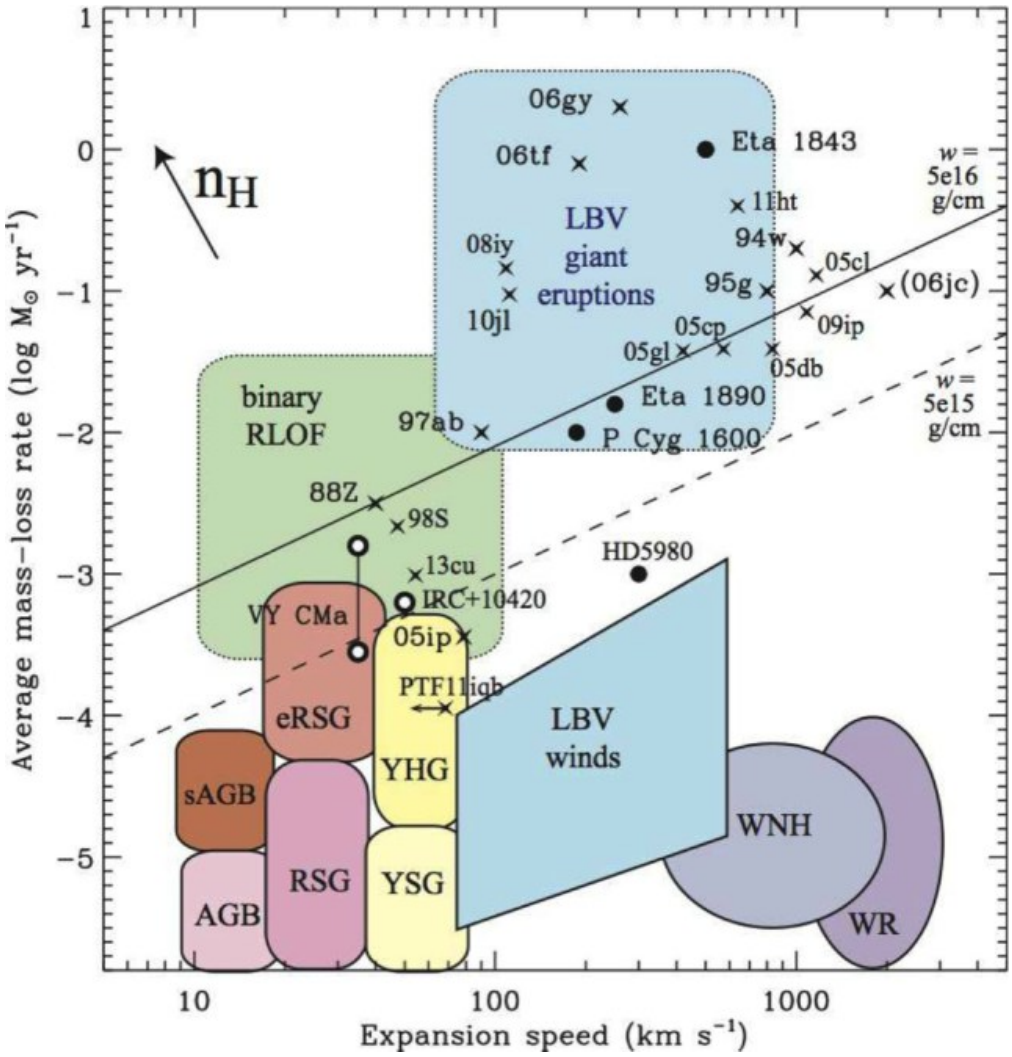

Figure 1.2: Expansion speed is plotted versus the average mass loss rate for different mechanisms and populations of massive stars, which occupy distinct areas of the parameter space. Mass-loss rates are plotted on a log scale; the number of solar masses expelled per year in RLOF and eruptions is orders of magnitudes higher than that of winds of any star. Figure reproduced with permission from Smith (2016).

The CSM that characterizes type IIn and other interacting SNe arises from wind-, outburst-, or companion-driven mass loss during the progenitor star's late evolutionary stages. Its properties probe the pre-explosion nature of the progenitor and its study makes it an excellent tool for assisting in progenitor identification for all SNe types, most critically for interacting types. The fact that the interaction emission is polarized is a key part of this effort because of its ability to encode geometric information.

1.3 Optical Polarimetry

1.3.1 Polarization of light

Light is electromagnetic energy produced via the acceleration of charged particles; it radiates in space at a constant speed c (in a vacuum, $c = 3 \times 10^8$ m s^{-1}). Discrete quanta of light are called photons and behave like waves and particles simultaneously. A photon travels through space as a transverse plane wave composed of synchronous $\vec{E}$ and $\vec{B}$ field oscillations that are orthogonal to one another and to the direction of propagation. Its intensity is given by the wave amplitude, which quantifies its power density and the relative brightness with which it is perceived. The wavelength (λ) and frequency ($\nu = \frac{c}{\lambda}$) are determined by the phase length of the field vibrations and their energy.

Large numbers of particles undergoing thermal collisions experience rapid acceleration fluctuations and collectively emit a continuous blackbody (Planck) spectrum of light with a peak wavelength and intensity that depend on the gas temperature. Additionally, a bound electron falling to a lower energy level in an atom generates a photon with energy specific to the potential difference in the transition and a wavelength and frequency that are therefore characteristic of the atomic species. Both light emission mechanisms are present in the SNe I consider.

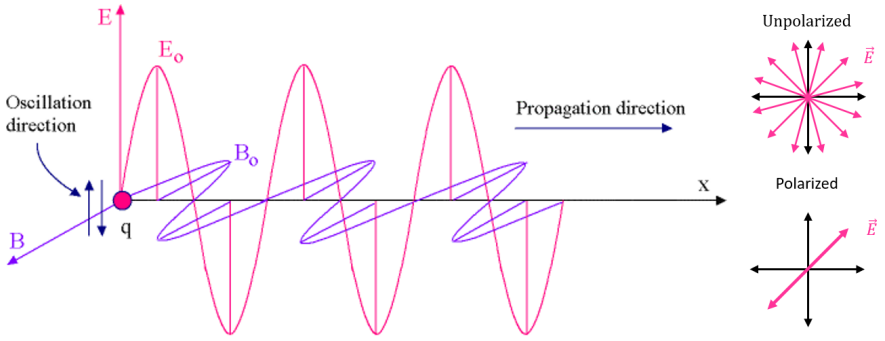

Figure 1.3: Orientation of $\vec{E}$ and $\vec{B}$ fields in light wave are aligned with the dipole of the moving charge (left, retrieved from: http://www.pstcc.edu/nbs/WebPhysics/Chapter%20034.htm). Photons in a beam of unpolarized light have randomly oriented $\vec{E}$ fields that cancel, while a beam of fully polarized light have $\vec{E}$ fields constrained to vibrate in a particular direction in the plane of propagation (right).

The alignment of a photon's $\vec{E}$ field vector with respect to the plane perpendicular to the direction of propagation is called polarization. Photons produced in blackbody emission generally have electric field vectors that are randomly oriented. The $\vec{E}$ field vectors of a beam of such photons cancel one another, resulting in light with zero net polarization. Interactions with matter, however, may cause a portion of photons in a beam to align in a specific direction. Such light is said to be polarized.

1.3.2 Stokes formalism

General plane waves must have solutions of the form

$$\vec{E} = \vec{E_0} e^{i(\vec{k}\cdot\vec{r} - \omega t)}$$

For a light wave, the electric field oscillates in the plane perpendicular to the direction of propagation, such that $\vec{k} \cdot \vec{r} = 0$. In the following derivation, I assume

a Cartesian coordinate system with the wave propagating in the $\hat{z}$ direction and $\vec{E_0} = \varepsilon_1\hat{x} + \varepsilon_2\hat{y}$. Using $e^{-i\theta} = cos\theta - i\sin\theta$ and taking only real components of $\vec{E}$,

$$\begin{aligned}
\vec{E} &= \varepsilon_1 e^{i(\vec{k}\cdot\vec{r} - \omega t + \phi_1)}\hat{x} + \varepsilon_2 e^{i(\vec{k}\cdot\vec{r} - \omega t + \phi_2)}\hat{y} \\
&= \varepsilon_1 e^{-i(\omega t - \phi_1)}\hat{x} + \varepsilon_2 e^{-i(\omega t - \phi_2)}\hat{y} \\
&= \varepsilon_1[\cos(\omega t - \phi_1) - i\sin(\omega t - \phi_1)]\hat{x} + \varepsilon_2[\cos(\omega t - \phi_2) - i\sin(\omega t - \phi_2)]\hat{y} \\
\mathrm{Re}(\vec{E}) &= \varepsilon_1\cos(\omega t - \phi_1)\hat{x} + \varepsilon_2\cos(\omega t - \phi_2)\hat{y} \\
E_x &= \varepsilon_1\cos(\omega t - \phi_1) \\
E_y &= \varepsilon_2\cos(\omega t - \phi_2)
\end{aligned}$$

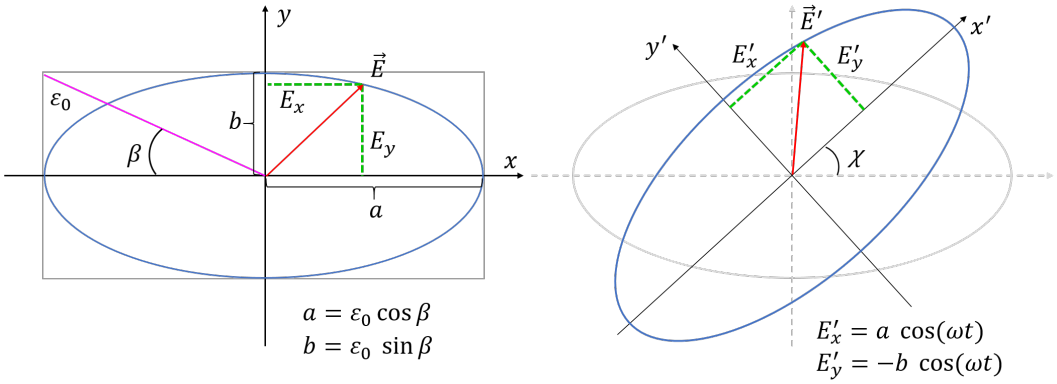

Figure 1.4: $\vec{E}$ field components describe an ellipse in reference coordinates (left) and rotated by the polarization angle χ in true coordinates (right). See Fig. 7.4 in Jackson (1998) and Fig. 2.4 in Rybicki and Lightman (1986).

These equations mathematically describe an electric field vector whose rotation with time traces out an ellipse (Fig. 1.4) with shape parameters ε_0 and β defining its size and ellipticity. In general, $\vec{E}^2 = E_x^2 + E_y^2$, while in coordinates rotated by

an angle χ, $\vec{\overline{E}}'^2 = E_x'^2 + E_y'^2$. Substituting for the semi-major axes a and b yields

$$\begin{array}{lll} a = \varepsilon_0 \cos\beta & & E_x' = a\cos\omega t \quad = \varepsilon_0 \cos\beta \cos\omega t \\ & \Longrightarrow & \\ b = \varepsilon_0 \sin\beta & & E_y' = -b\sin\omega t \quad = -\varepsilon_0 \sin\beta \sin\omega t. \end{array}$$

$\vec{\overline{E}}^2$ is related to $\vec{\overline{E}}'^2$ through the angle χ. We can obtain expressions for E_x and E_y in terms of the ellipse parameters and phase rotation alone. If we rotate the primed components back into the original coordinates and insert the magnitude of the electric vibrations in x and y and any phase differences, we can obtain expressions described only by the ellipse parameters ε, β, and χ. These equations are called "Stokes parameters" and conveniently summarize the polarization behavior of a light beam.

$$S = \begin{pmatrix} I \\ Q \\ U \\ V \end{pmatrix} \equiv \begin{pmatrix} \varepsilon_1^2 + \varepsilon_2^2 \\ \varepsilon_1^2 - \varepsilon_2^2 \\ 2\varepsilon_1\varepsilon_2 \cos(\phi_1 - \phi_2) \\ 2\varepsilon_1\varepsilon_2 \sin(\phi_1 - \phi_2) \end{pmatrix} = \begin{pmatrix} \varepsilon_0^2 \\ \varepsilon_0^2 \cos(2\beta)\cos(2\chi) \\ \varepsilon_0^2 \cos(2\beta)\sin(2\chi) \\ \varepsilon_0^2 \sin(2\beta) \end{pmatrix}$$

For a quasi-monochromatic light wave, the polarized intensity I_{pol} is equal to the Stokes parameters Q, U, and V added in quadrature. The quantity I_{pol} divided by the total intensity of the beam I is the degree of polarization Π, often represented as a percentage denoted by p. The angle χ is called the "polarization angle" or "position angle" and is also represented by θ.

$$\begin{aligned} {I^2}_{pol} &= Q^2 + U^2 + V^2 \\ p = \Pi &\equiv \frac{\sqrt{Q^2 + U^2 + V^2}}{I} \\ \theta = \chi &= \frac{1}{2}\arctan\left(\frac{U}{Q}\right) \end{aligned}$$

Light is linearly polarized when the ellipse angle $\beta = 0$ or $\pm\,\pi$, which forces the ellipse to lie flattened along its semi-minor or semi-major axis in the reference frame. Substituting those values results in a Stokes V parameter of zero and degeneracy among χ angles oriented 180° from one another. Thus, the polarization of a linearly polarized light wave is fully specified by either (p, θ) or by (Q, U). I will use these representations interchangeably.

$$S = \begin{pmatrix} \varepsilon_0^2 \\ \varepsilon_0^2 \cos(2\chi) \\ \varepsilon_0^2 \sin(2\chi) \\ 0 \end{pmatrix} \implies \begin{pmatrix} 1 \\ 1 \\ 0 \\ 0 \end{pmatrix} \begin{pmatrix} 1 \\ 0 \\ 1 \\ 0 \end{pmatrix} \begin{pmatrix} 1 \\ -1 \\ 0 \\ 0 \end{pmatrix} \begin{pmatrix} 1 \\ 0 \\ -1 \\ 0 \end{pmatrix}$$

$$\text{for } \chi = \begin{bmatrix} n\pi & n + \frac{1}{4}\pi & n + \frac{1}{2}\pi & n + \frac{3}{4}\pi \\ \updownarrow & \nearrow\!\!\swarrow & \longleftrightarrow & \nwarrow\!\!\searrow \end{bmatrix}$$

In the linear case the fractional polarization p only depends on Q and U, which can be expressed in terms of p and θ as fractions of the total light.

$$p = \frac{\sqrt{Q^2 + U^2}}{I}$$
$$q = \frac{Q}{I} = p\cos 2\theta$$
$$u = \frac{U}{I} = p\sin 2\theta$$

1.3.3 Spectropolarimetry

There are many different polarigenic mechanisms in astronomy. Discussion here will focus on the most common sources relevant to this work: electron and resonance scattering of light passing through a medium of gas or dust.

Free electrons in an ionized gas are stimulated by photons that pass too closely. Energy from the photon causes the electron to vibrate as a dipole in the same direction as its $\vec{E}$ field. The electron radiates its own photon due to the acceleration which is linearly polarized along the same axis. This process, Thomson scattering, is independent of the frequency of the incident light and affects all wavelengths equally across a continuum.

Polarization produced by scattering from dust particles is highly complex. Like the Thomson case, dust scattering behavior affects the entire continuum, but the amount of polarization produced is highly dependent on wavelength and hinges on the composition, size, shape, and alignment of individual dust grains (Clarke 2009). The relationship between wavelength and polarization produced by interstellar dust was first characterized by Serkowski (1973). Dust formation necessitates lower temperatures to form, as atoms in a gas of high temperature are too energetic to coalesce into dust particles. The circumstellar environments around CCSNe at early times are not conducive to dust formation and the effects of dust on scattering and polarization are therefore not included in this work.

Something very different happens when photons encounter atoms of a gas with spectral lines matching their frequencies. An atom in a ground or low energy state that encounters one of these "Goldilocks" line photons absorbs it and becomes excited, de-exciting and re-emitting the photon in a different direction some time later. This is resonance scattering and affects only those photons with wavelengths in resonance with energy level potentials very close to those of the scattering material. For atoms moving at low speeds the wavelength of the re-emitted photon is very close to the original incident photon. Atoms moving with appreciable velocity re-emit photons with wavelength discrepancies described by the Doppler effect (Henney 1994). This has the effect of widening the spectral line by an amount that is proportional to the velocity of the scattering material.

Unlike continuum effects, polarization across spectral lines contains information about the arrangement and optical properties of materials of different composition within an overall structure. It is utilized in areas of research such as galaxies, stars, the sun and solar system, nebulae, and the interstellar medium as a tool to examine how the structures of these objects vary with composition. Supernovae are no exception, and the use of spectropolarimetry to reconstruct the properties of their ejecta and CSM is now commonplace.

1.3.4 Polarimetry of CCSNe

Light from the ejecta of a CCSNe that interacts with asymmetric distributions of CSM of is polarized via several different scattering mechanisms depending on its specific composition and optical properties (Kasen et al. 2003; Wang and Wheeler 2008; Tanaka et al. 2017). Early supernova polarimetry research focused on the extent to which the spectral continuum was polarized due to large-scale asphericity of the ejecta (Höflich 1991; Wang et al. 1997). Advances in instrumentation have made possible higher-resolution spectropolarimetric observations that allow us to use the polarization in spectral lines to reconstruct the more complex distribution of elements within the ejecta and CSM.

Polarization work is not limited to SNe with strong interaction. Studying observations of polarization of lines in SNe was pioneered by Jeffery (1987) in his work on SN 1987A in which he identified separate asymmetric photosphere and scattering atmospheric regions and was able to characterize the CSM as an oblate spheroid. Leonard et al. (2006) observed a marked increase in the line polarization of the type II-P SN 2004dj around day 90, which he attributed to the exposure of highly disordered inner core material upon thinning of the relatively spherical photosphere, evidence for the asymmetry of the interior explosion and shock propagation. Reilly et al. (2016) found significant polarization over the course of 50 days in lines of

calcium, helium, and sodium corresponding to two discretely separate regions in the ejecta of type Ib iPFT 13bvn. Spectropolarimetry has been particularly revealing for transitional SNe IIb. Maund et al. (2007) and Stevance et al. (2016) were able to analyze SN 2001ig and 2008aq pre, mid, and post explosion, finding geometric similarities to other IIb and differences among helium lines they believe are indicators of the extent of stripping from RLOF.

Early modeling of SNe was focused on polarization produced by the overall global asymmetry of the ejecta. These models relied heavily on the Sobolev approximation which only allows for single scattering of photons. Models of the radiative transfer and polarization in SNe atmospheres by Dessart and Hillier (2011) have yielded some important clues as to how polarization signatures are produced, despite their one dimensional limitations. Namely that the polarization levels in SNe heavily depend on density and ionization of the scattering regions and implies that changes in polarization over time aren't necessarily due to changes in asymmetry. Profiles arising from varying scattering region parameters are degenerate; there is more than one combination of characteristics capable of producing the same line polarization feature. Similarly, reliance on the Sobolev approximation only allows for single scattering. There are only 4 spectropolarimetric studies of strongly interacting SNe classified as type IIn to date: SN 1998S by Leonard and Filippenko (2000) and Wang in 2001; SN 1997eg by Hoffman et al. (2008); SN 2006tf by Smith et al. (2008); SN 2010jl by Patat in 2011 and Bauer et al. (2012).

The code developed for this work uses full radiative transfer with multiple scattering to examine how the flux spectrum of a SN becomes polarized as it radiates through a variety of stationary CSM configurations. The three dimensional capability allows for geometries of multiple broken asymmetries, such as the addition of high density clumps, and the modeling of $Q-U$ loop behavior. It includes resonance line scattering of the Hα core and electron scattering of the entire spectrum to ex-

amine effects on the level of polarization in both the line and continuum. Multiple light source components are able to emit from distributed regions as well as from the central ejecta photosphere. While in the context of this research project it is focused on reproducing polarization signatures in strongly interacting SNe, as a model it is still highly applicable for progenitors of any SNe types in order to investigate their mass loss histories.

1.4 This Work

The specific goal of this work is to constrain progenitor mass loss for SNe of type IIn by quantifying geometrical information contained in their polarized Hα line profiles. A large grid of computational models was created to explore which regions of the CSM parameter space reproduce physically realistic polarized lines. Polarized Hα emission profiles from the type IIn SNe 1997eg and 2010jl are fit to the model grid as a function of time in order to constrain their individual mass loss history and potential progenitor types.

1.5 Outline

Chapter 2 will give an overview of the modeling code SLIP and discuss the parameters and characteristics of the model grids used to fit observational data. This is followed by discussion of how this model data was obtained and reduced, the process for fitting the models to the data, and the statistical methods developed to sort and quantify the results obtained from the fitting processes. Chapter 3 will discuss the observational history of the type IIn SN 1997eg, describing the sources of the data used in the model comparison and relevant conclusions by previous authors, and then discuss in detail the results of the model fits to the spectra from this supernova. Chapter 4 follows the same format for a second supernova, the

type IIn SN 2010jl. In Chapter 5 the results are interpreted within the context of current understanding of this group of SNe and the massive stars that are potential progenitors.

Chapter 2

SLIP and Spectropolarimetric Modeling

2.1 Introduction to *SLIP*

Supernova LIne Polarizaton, or *SLIP*, is a three-dimensional radiative transfer code developed by Hoffman et al., *in prep.* (referred to as Paper I) to simulate the way polarized Hα line profiles are created in a supernova surrounded by CSM. *SLIP* uses the Monte Carlo radiative transfer methods described by Wood et al. (1996) and Whitney (2011) to track individual photons as they scatter through surrounding circumstellar configurations of pure hydrogen gas. The code performs full radiative transfer without relying on the Sobolev approximation; see Paper I for a detailed description. It does not take into account any expansion of the scattering regions, which must also affect the resulting line profiles; however, the stationary model is still useful as a first approximation, particularly in cases of low CSM expansion velocity. This is an area of current development with the code, with plans for implementation in late 2017.

Table 2.1: Fixed Parameters of All Geometric Models

Fixed model parameters	Disk	Toroid	Ellipsoid
Radius of central source ($R_\odot$)	1.00	1.00	1.00
Outer CSM radius ($R_\odot$)	15.16	15.16	10.11–15.16
Ellipsoid semi-major axis ($R_\odot$)	–	–	15.16
Ellipsoid semi-minor axis ($R_\odot$)	–	–	10.11
CSM, shock height ($R_\odot$)	3.03	3.03	–
Opening Angle (°)	11.29	11.29	–
CSM thickness ($R_\odot$)	7.58	1.08	1.08
Shock region thickness ($R_\odot$)	0.76	0.76	0.76

Because it relies on numerical integrations, *SLIP* has the capability to emit light from multiple regions in the model space, including regions of extended volume. This allows us to investigate contributions to the observed polarization from light arising from CSM gas ionized due to interaction. In this work, I capitalize on this capability, which has not previously been used in modeling SNe, to create two distinct sets of models. The two sets differentiate between weakly interacting SNe, for which the underlying spectrum of the ejecta can be deconvolved from that of the interaction, and strongly interacting SNe, for which it cannot. I refer to the weakly-interacting models as "central-source" and the strongly-interacting models as "distributed-source."

In the central-source models presented here, I construct the "photosphere" of the supernova ejecta as a finite spherical source at the center of the model grid, with a radius of 1 $R_\odot$. For the emitted spectrum, I use the Hα region (between 5950 Åand 7030 Å) of a synthetic type II-P supernova spectrum generated with the PHOENIX stellar atmosphere code (Hauschildt and Baron 1999; P. Nugent, *priv. comm.*). This source is surrounded by an extended scattering region of pure hydrogen, representing the CSM, whose parameters are detailed in Table 2.1. Within the inner radius of each CSM configuration, I define a radially thin "shock" region to represent the

Table 2.2: Varied Parameters of Model Grid

Varied model parameters	Considered range
Geometry	Ellipsoid, Disk, Toroid
CSM Optical Depth	0.5, 1.0, 2.0
$L_{\rm CSM}/L_{\rm SN}$[1]	0.0, 0.1
$L_{\rm Sh}/L_{\rm SN}$[2]	0.01, 0.20, 1.0
CSM Temperature (10^3 K)	5, 20, 50
Angle (divided into 12 bins)	$0^\circ - 90^\circ$

[1] $L_{\rm CSM}$ and $L_{\rm Sh}$ are given as fractions of the source spectrum brightness.
[2] Distributed models with $L_{\rm Sh} = 1.0$ have the entire source spectrum emitted from their shock region.

interaction of the supernova's forward shock with the ambient CSM. This region both scatters and emits light (see below).

For the distributed source models, I assume the light emitted from the SN photosphere is entirely obscured by the emission arising from the ionized CSM. In this case, the code emits light entirely from the shock region, with no contribution from a central source. I created an input spectrum for this emission based on the Hα region of the observed spectrum of SN 1997eg at day 16 (Hoffman et al. 2008). I discuss the uncertainties associated with this assumption in Chapters 3 and 4.

I constructed two model grids by varying the parameters listed in Table 2.2. I considered two different axisymmetric morphologies for the CSM: a radially thin equatorial ring or "toroid" and a radially thick equatorial "disk"; these are depicted to scale in Fig. 2.1. Due to computational expense, the grids do not contain models with an ellipsoidal geometry.I considered CSM optical depths ranging from $0.5 - 2$ and CSM temperatures ranging from $10,000 - 50,000$ K. These temperatures are consistent with those obtained for the CSM of SN 1997eg by Hoffman et al. (2008), assuming the material is photoionized. Combinations of these optical depths and temperatures for each geometry produce a range of CSM mass and number densities consistent with observational estimates made by Fransson et al. (2014) for SN 1997eg and Borish et al. (2015) for SN 2010jl, as well as for other SNe IIn such as SN 1998Z

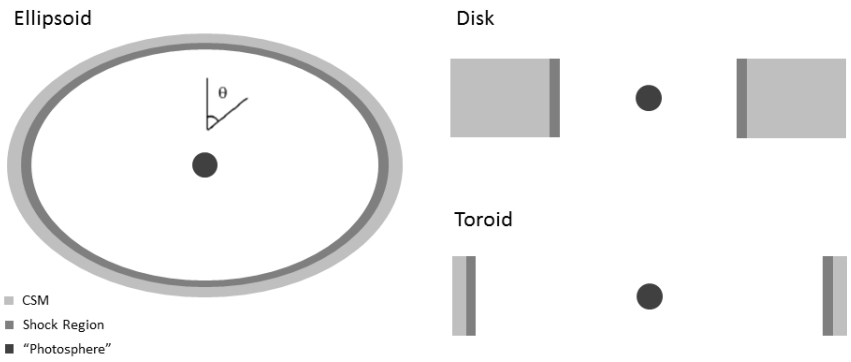

Figure 2.1: Cross-sectional representations in the x-z plane, to scale, of our three scattering geometries. Dimensions are listed in Table 2.1.

(Aretxaga et al. 1999). I adjusted the effective luminosities of the CSM and shock by varying the number of photons arising from these regions relative to the total number emitted ($L_{\rm CSM}$ and $L_{\rm Sh}$, respectively). By definition, distributed source models emit only from their shock regions and therefore have no variation in the $L_{\rm Sh}$ parameter. They thus comprise a smaller set of models then the central grid. A more detailed justification of the particular values used for each parameter can be found in Paper I.

Both the CSM and the shock region have constant particle densities throughout their volumes; photons may be emitted uniformly from the volume of either of these regions as well as from the central photosphere. The models I present here do not assume the warm CSM is heated directly by the supernova. Instead I assign the CSM a uniform temperature as an input parameter; its ionization fraction and emission and albedo spectra are then calculated as described in Paper I, assuming

local thermodynamic equilibrium. I list the resulting densities and other relevant parameters in Table 2.3. The shock region has a constant temperature of 50,000 K and is thus fully ionized; it emits only photons at the Hα rest wavelength (6562.79 Å) with a full width at half maximum (FWHM) of 160 km s^{-1}. This is consistent with the widths of the narrow lines in SN 1997eg (Salamanca et al. 2002; Hoffman et al. 2008) and results in a full width at half maximum (3.5 Å) smaller than the wavelength resolution of the observed spectra we use for comparison.

All of the CSM configurations in both grids are axisymmetric and also symmetric with respect to reflection across the $z = 0$ plane; this allows me to characterize each model by focusing only on one octant of the three-dimensional grid. Within one octant, outgoing photons are binned into 12 latitudinal bins with equal widths in the polar angle θ. For simplicity, I also assume that the axis of symmetry of the CSM configurations corresponds to the viewer's line of sight; that is, I place the observer at $\phi = 0$. Thus the only geometric degree of freedom per model is the inclination angle θ.

Omitting consideration of ϕ dependence prevents full investigation of how model parameters might affect the formation of so-called "$Q - U$ loops," which figure prominently in the polarization spectrum of SN 1997eg, as these phenomena likely form from the combined effects of two misaligned axes in the system (Hoffman et al. 2008). I have plans to run $\phi-$dependent models with 12 longitudinal bins of equal width in the azimuthal direction. Spherical, fully absorbing "clumps" of material will be added at the outer edge of the CSM at $(\theta, \phi) = (90°, 0°)$. Linear polarization of the spectra will be examined at 6 ϕ bins spanning $\pm 90°$ of the clump location bringing the total number of unique viewing locations and accompanying spectra to 72 for a single model Consideration of these more complex scenarios is planned for future work.

Table 2.3: CSM Characteristics

Geometry	Optical Depth	Temp. (K)	ρ (10^{-12} g cm^{-3})	σ (g cm^{-2})	n_e (10^{12} cm^{-3})	N_e (10^{23} cm^{-2})
Disk	0.5	10000	2.39	1.39	1.41	8.18
		20000	2.40	1.39	1.42	8.24
		50000	2.40	1.39	1.42	8.24
	1	10000	4.79	2.78	2.83	16.42
		20000	4.79	2.78	2.84	16.48
		50000	4.79	2.78	2.84	16.48
	2	10000	9.59	5.56	5.67	32.90
		20000	9.55	5.54	5.65	32.78
		50000	9.55	5.54	5.65	32.78
Toroid	0.5	10000	17.8	10.3	99.5	577.31
		20000	17.8	10.3	99.9	579.63
		50000	17.8	10.3	99.9	579.63
	1	10000	35.7	20.7	20.0	116.04
		20000	35.6	20.7	20.0	116.04
		50000	35.6	20.7	20.0	116.04
	2	10000	71.8	41.7	39.9	231.51
		20000	70.9	41.1	39.8	230.93
		50000	70.9	41.1	39.8	230.93

In order to compare my model results with observed data, I subdivide all spectra into wavelength bins of width 5 Å. The rest wavelength of the Hα emission line emitted from the CSM and shock regions lies at 6562.79 Å, less than an Angstrom from the wavelength bin edge at 6562.5 Å. When Hα photons are emitted within the code, they must be discretized such that the energy within the line is correctly distributed among wavelength bins. Emission lines from both regions have Gaussian profiles with widths resulting from Doppler broadening due to a velocity distribution of the particles, from thermal kinetic motion (within the near-stationary shock) and radial expansion velocity (within the CSM; Irwin 2007). To determine this division of line intensity I calculated the partial area under a Gaussian curve when intersected by a vertical line at some fractional σ from its central wavelength, a

value given by the *erf* function. The thermal CSM emission lines are described by a FWHM that depends on temperature, and I calibrate their total emission via the coefficients in Table 4.2 of Osterbrock and Ferland (2006), which describes the intensity (erg cm^3 s^{-1}) of Hα emission in a gas from recombination. Higher CSM temperatures result in an emission line divided more equally between the two neighboring bins. I include the FORTRAN routines I developed for this new code capability in Appendix B.

2.2 Data acquisition

In this dissertation, I present 108 central source and 36 distributed modelscreated using two different computing clusters to obtain the model data: DU's HPC Beowulf cluster, which consists of 180 CPUs with 2.44 GHz Intel Xeon processors, and the Texas Advanced Computing Center's (TACC) Stampede supercomputer, a member of the Extreme Science and Engineering Discovery Environment (XSEDE). Stampede consists of 6400 compute nodes each with two 2.7GHz Xeon E5-2680 8-core Sandy Bridge processors, for a total of 102,400 CPUs.

I ran each simulation at a spectral resolution of 5 Å per bin, with a total of 1.60×10^{11} and 2.13×10^{11} photons for disk and toroid geometries, respectively. *SLIP* models have Poisson distributed errors that are proportional to the square root of the counts in a given wavelength and viewing angle bin. Sound statistical comparison of the model grid to observed data necessitates that the models have uncertainty levels comparable not only to the observation, but also to one another. I discuss the specific signal requirements in Section 2.3.1 below. Larger optical depth and density values increase the number of photons absorbed by the CSM, particularly when coupled with lower temperature, resulting in diminished signal and greater uncertainties. Larger numbers of input photons are required in these cases. Parallelization of the code allows for the reduction of run times by splitting

the input photons over multiple processors, generally 32 CPUs each, for a total of $5 - 6.67 \times 10^9$ photons per core depending on the specific model parameters. This typically resulted in ~ 3070 hour run times per model on the DU cluster and $\sim 20 - 40$ hours per model on Stampede.

The ellipsoidal CSM geometry posed a rather extreme computational challenge, particularly when coupled with the high absorption rates of CSM with large optical depth. Because of its closed geometry, all emitted photons *must* pass through the CSM to escape, increasing run times significantly due to the greater number of scattering events. If optical depth is high and temperature low, escaping signal for ellipsoids is less than 1% of the initial photon count. I found two to three orders of magnitude more photons were necessary to achieve the necessary signal, but the time required to run them became exponentially prohibitive. Stampede has enough processors to handle such large simulations, but the restrictions on wall time and limits to the number of CPU hours per award grant make each model quite costly. The DU HPC is free and has no wall time restrictions, but there are not enough CPUs to reduce run times to a realistic or manageable level. For these reasons, I have not included a panel of ellipsoids in the model grids I present here.

2.3 Data reduction and analysis

In the following chapters, I present comparisons of my model results with observed data for two well-studied SNe IIn. Data for SN 1997eg were obtained with the Keck Low-Resolution Imaging Spectrometer in polarimetry mode (LRIS-P; Hoffman et al. 2008) at three epochs in 1997 and 1998; these data have a native resolution of 2 Å. Data for SN 2010jl were obtained with the SPOL spectropolarimeter at the MMT telescopes at 11 epochs between 2010 and 2012, with resolutions of 4 Å (Williams et al. *in prep.*).

2.3.1 Model data reduction

Because of the larger uncertainties inherent in polarization data, I rebinned both model and observed polarization spectra to 40 Å to further reduce uncertainties, as well as to smooth out any contribution from the weak Fe X λ6374 line in the observed data for SN 1997eg. To ensure reliable fitting, I ensured each model's average uncertainties in the 40 Å spectra were at or below 10% of the uncertainties in the LRIS data for SN 1997eg. These observed uncertainties average 5-10% of the total flux across a spectral line (Modjaz et al. 2011).

I found frequent variation in model signal and associated uncertainty levels as a function of the polar angle θ, due to changes in CSM density and opacity. It was difficult to obtain ideal levels of uncertainty in these bins without excessive over-reduction of errors in the others. In cases where a fraction of the viewing angle bins in θ had borderline signal-to-noise ratios (SNR), I used a second metric of χ^2 stability to determine whether the model was high-quality enough for inclusion in the grid. This method creates a "noise model" to assess whether uncertainties are small enough that variations within them would not appreciably affect a fit to observational data.

In this method, for every bin and for every data point in the associated model spectrum, I sampled 1000 random values from within a Gaussian distribution with a FWHM given by the uncertainty of the spectrum. In the large sample number limit, Poisson errors are well approximated by a Gaussian distribution, which also has the advantage of simplicity in implementation. I fit the grid of noise models via χ^2 minimization to the observed data from the first epoch SN 1997eg and calculated the standard deviation in the resulting χ^2_ν values. A standard deviation less then the square root of the mean χ^2_ν value of the original model indicates that the fit was not greatly affected by the level of uncertainty. The lowest realistic value for χ^2_ν is approximately 1; therefore a standard deviation of < 1 for any given mean value

indicates good stability. In practice, all *SLIP* models with borderline uncertainties produced noise models whose χ^2_ν values had standard deviations of $\lesssim 0.1 - 0.3$; I therefore accepted them for inclusion in the model grid.

After admitting models to the grid, I trimmed them in wavelength around the region of the Hα line from 6150 Å to 6750 Å. This wavelength region includes the widest components of the observed emission lines out to the continuum, while masking the contribution of any other nearby strong lines. I then normalized the model flux to the bluest point of the same range in the observed data to compare Hα emission line strengths.

2.3.2 Model fitting

To assess fits between my models and the observed data, I first performed a χ^2 minimization analysis to compare the polarization spectra from the *SLIP* models with the observed polarization from all epochs of SN 1997eg and SN 2010jl. Given a set of N observational data points x_i with uncertainties σ_i, and a set of model data μ_i, in which the model values are expected to be equal to the square of the observed uncertainties, the χ^2 metric is given as

$$\begin{aligned} \text{observation} &= \mathrm{x}_i \pm \sigma_i \\ \text{model} &= \mu_i \pm \xi_i \qquad\qquad \chi^2 = \sum_{i=1}^{N} \left(\frac{x_i - \mu_i}{\sigma_i} \right)^2 \\ \text{where } \sigma_i &= \sqrt{\mu_i} \end{aligned}$$

Interstellar polarization (ISP) contributions to the observed polarization of extragalactic sources are notoriously difficult to ascertain and are often hand-waved away by the observational SN community when estimation or measurement is not possible. ISP contributions to polarization are generally independent of wavelength, and should also be consistent between any two epochs of early SN observation. Because I am interested in matching the profile of polarization in the Hα region as it

varies across the line, I allow each spectrum to translate vertically in p with respect to the observed polarization data. The additional polarization shift that produces the lowest χ^2 value is recorded for each model at every epoch; it provides a potential constraint on the amount of ISP in an observed spectrum.

I have chosen to omit several points in each spectrum from the fitting process, reducing the total number of points from 16 to 11 for SN 1997eg and from 16 to 14 for SN 2010jl. Wavelengths in the "intermediate-width" portions of the Hα line ($1000 - 3000$ km s^{-1}) arise from the heating of CSM gas interior to the fast moving forward shock (Smith et al. 2008; Smith 2016). Because *SLIP* assumes stationary material, it cannot reproduce this line component. Thus, I omit wavelength points at 6510Å and 6590Å from all comparisons. Similarly, SN 1997eg displays an enhanced blue wing of polarization between 6350Å and 6430Å, which likely arises from a high-velocity CSM component (Hoffman et al. 2008). I omit these points as well in the case of SN 1997eg.

The number of degrees of freedom in my model fits is thus $N - n - 1$, where N is the number of wavelength elements and $n = 1$ reflects the single location parameter introduced by the model polarization shifting. Using this method to test the observed data against each model and viewing angle in the grid, I calculated the χ^2 and χ^2_ν (reduced χ^2) parameter for each case. Because number of degrees of freedom varies with the observational data, I present the results as reduced χ^2 values. I compare the calculated χ^2_ν values with the critical region of the χ^2_ν distribution for a significance level 0.05α =(defined numerically for each case in the appropriate subsection below). In essence, I am testing the hypothesis that the observed data arise from a parent population having the line profile of the model being tested. If the χ^2_ν values I calculate are outside the critical region, the model is rejected at the 3σ level.

The χ^2 test has limited power, particularly in cases where the model being fitted is nonlinear (Andrae et al. 2010). As an additional discriminator, I apply a one-dimensional Anderson-Darling test, a modification of the Kolmogorov-Smirnov test, to the normalized residuals of each model-data comparison to quantify the extent to which the residuals follow a Gaussian distribution with mean $\mu = 0$ and variance $\sigma^2 = 1$ (Stephens 1974). This test produces a numerical index A^2, which I compare with a critical value that depends on the distribution type, number of wavelength bins N, and desired level of confidence. For a normal distribution and confidence level $\alpha = 0.05$, $A^2_{D,n} = 0.68$. If A^2 is greater then this value, the residuals are rejected as not consistent with a Gaussian distribution.

My results indicate that the current implementation of *SLIP* does not include all physical considerations necessary to produce model spectra that consistently achieve χ^2_ν values below the critical level. There are limitations to what *SLIP* is able to reproduce given the assumptions it is currently built on. The models in this work are therefore aimed primarily at reproducing the correct levels of polarization in the continuum and narrow portions of the line. This does result in higher χ^2_ν values obtained from the fits to the polarization, particularly in the case of SN 1997eg.

It is not the intent of this work to identify a single best fitting model, but rather to identify values and combinations of parameters with the tendency to improve the χ^2_ν fit for each set of observational data. To do this, I order the models by ascending χ^2_ν value and remove outliers with very large χ^2_ν from the population using a one-sided median-absolute-deviation (MAD) test which is independent of sample size (Iglewicz and Hoaglin 1993). Outlier models with exceptionally poor fit are not the focus for analysis in a minimization process and their presence affects the clustering behavior of the non-outlier population. This process is illustrated in Fig. 2.2.

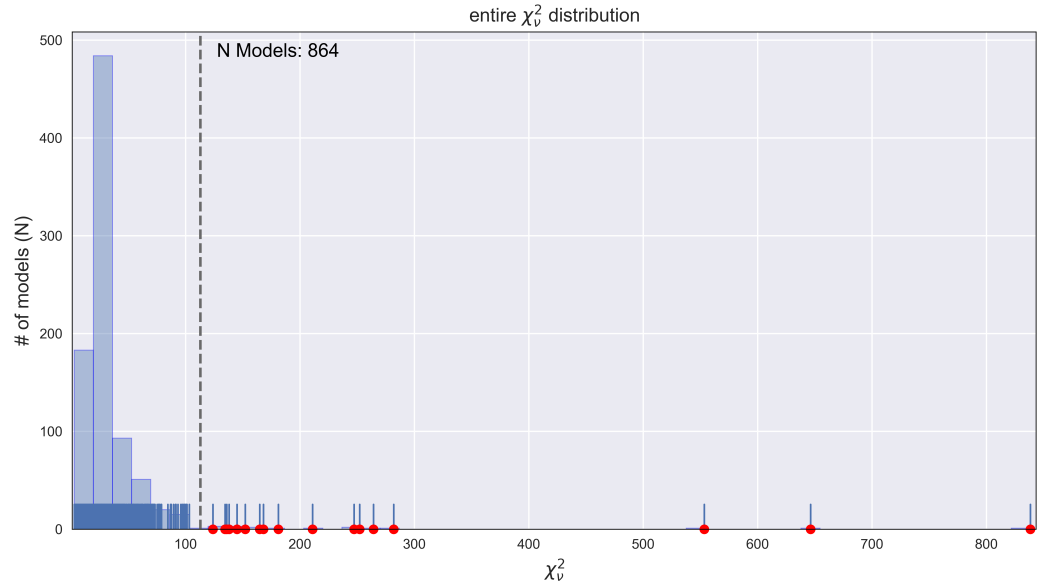

Figure 2.2: One-sided MAD test identifies models with very high χ^2_ν, marked by red points, for the first epoch of SN 1997eg.

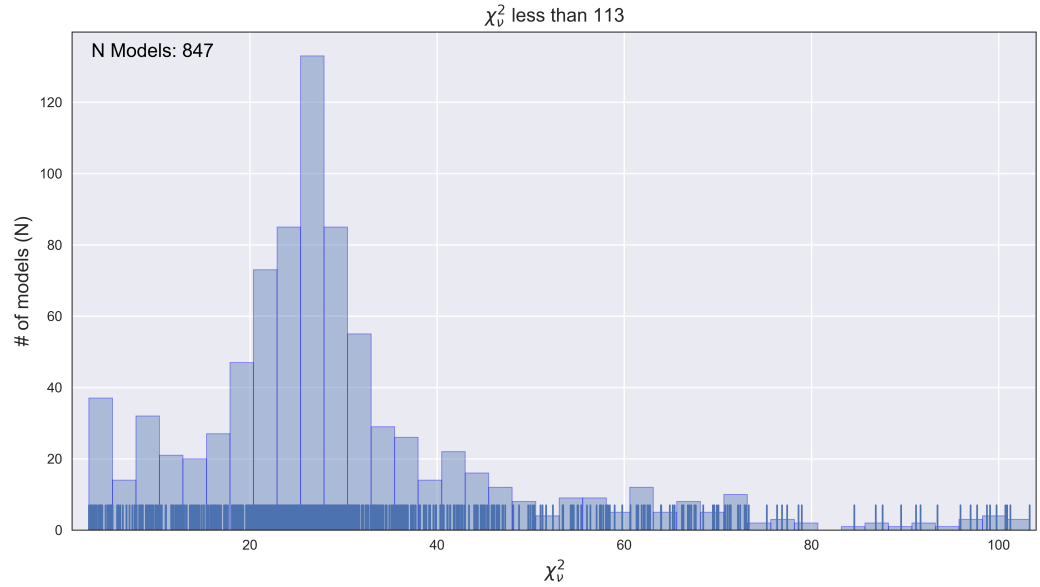

Figure 2.3: The distribution of χ^2_ν for epoch 1 of SN 1997eg after outliers are removed. A χ^2_ν cutoff value is determined and models below that value are considered for clustering.

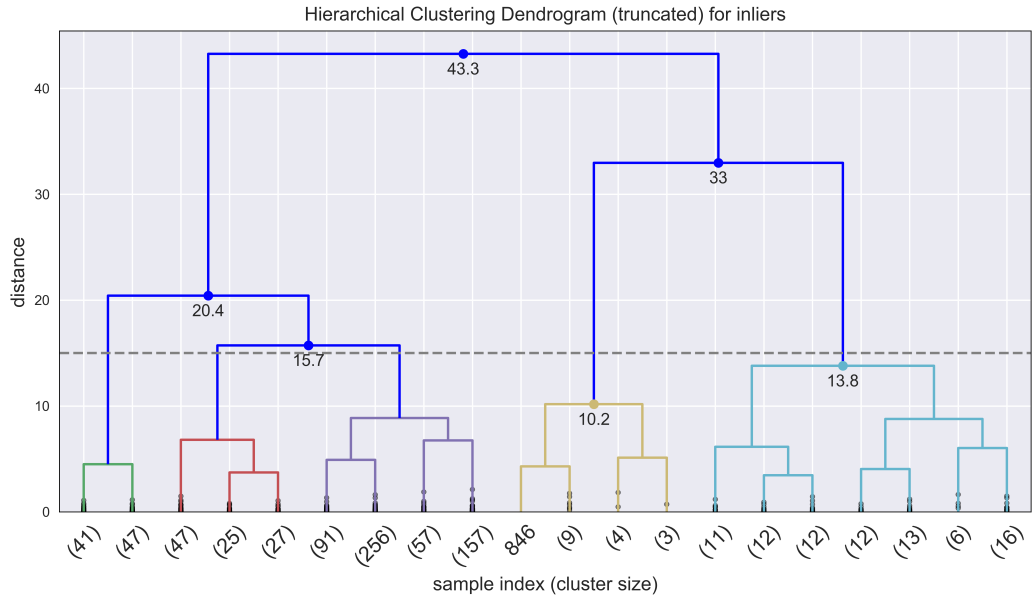

Figure 2.4: Truncated dendrogram of clusters identified by the UPGMC algorithm. The cutoff distance is chosen to optimize the relative distances of each group.

For the remaining distribution of models, illustrated in Fig. 2.3, I perform a hierarchical clustering analysis to identify which form a unique group with the lowest χ^2_ν values. I link the models using an unweighted pair group method with centroid averaging (UPGMC) algorithm, which calculates the euclidean distances between the centroids of each χ^2_ν cluster as they form to link two smaller ones together (Tan et al. 2005). Visual examination of the linkage in a dendrogram plot like the one in Fig. 2.4 allows for the selection of an appropriate cutoff distance to separate the clusters and isolate the one at the lower end of the χ^2_ν range. In general, an appropriate cutoff distance is one such that below it, branches form clusters with relatively equal vertical heights joining them to the next highest level. Final assignment to each cluster is then made using the cutoff value, and each group's population number, limiting values, and means are calculated. I visualize the cluster distributions by plotting them on top of the original parent distribution as seen in Fig. 2.5.

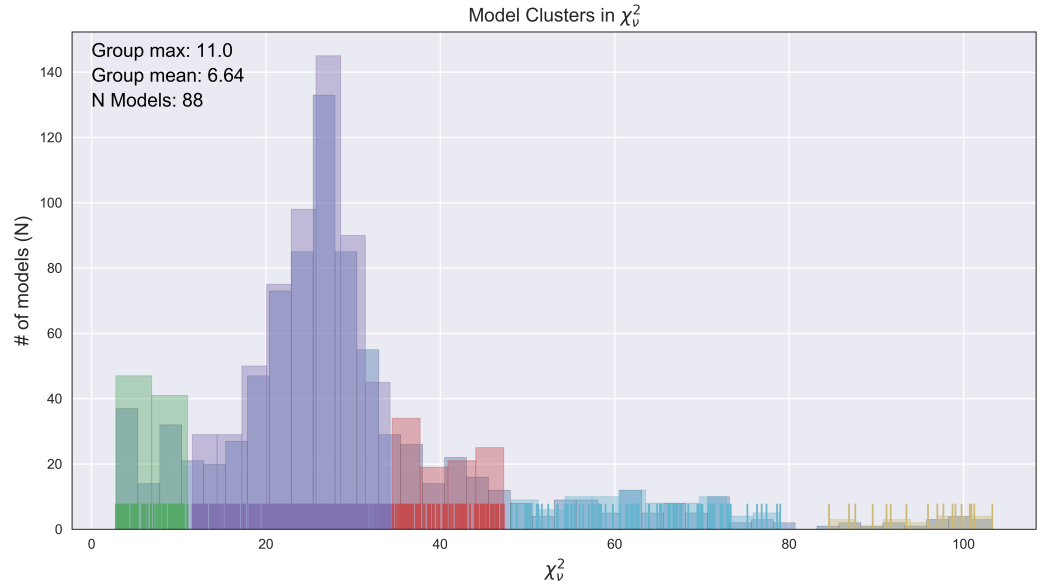

Figure 2.5: Locations of the clusters are visualized by plotting their histograms with varying color on top of the original distribution.

For each SN at each epoch, I examine the distribution of models between the inlier and low cluster populations in several ways in order to draw inferences about the interaction with the CSM over time. Key values examined between models of different parameters include: the flux emission strength ratio, henceforth called the emission ratio, a measure of the height of the emission line peak above the average of the first 10 points of the normalized continuum, and the percent polarization shift or polarization excess which is the amount of vertical translation required to minimize the fit for an individual model. I afford special consideration to models with χ^2_ν values within the lowest cluster, residuals that are normally distributed, and emission ratios that approximate observation. I will discuss these methods in subsequent chapters as I analyze the statistical behavior of the fits to each SN.

Requiring models to have emission ratios that exactly match observation as a constraint on the model space is problematic. Because *SLIP* does not yet include dynamic behavior in the shock and CSM, Hα line photons are not Doppler shifted

into the intermediate-width region, and thus the code produces narrow-line heights larger than is physically realistic. Models that match observed emission ratios in their current realization will produce much lower emission line ratios once a more realistic physical treatment is added to *SLIP*. To account for this, models with emission ratios *higher* than observation should be preferred.

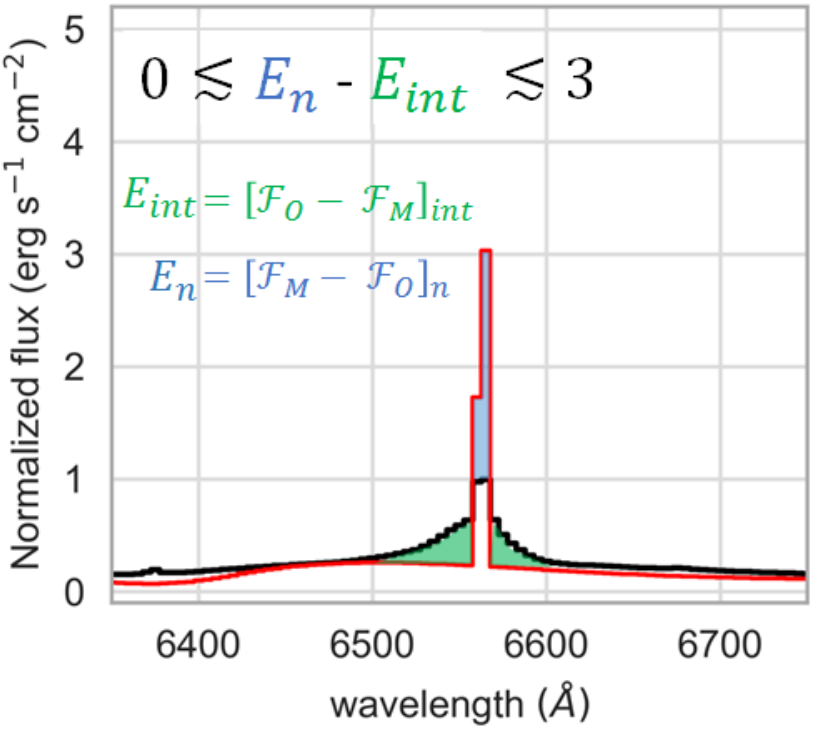

Figure 2.6: I calculate the flux emission ratio metric by subtracting the intermediate line flux deficit E_{int} from the excess narrow line flux E_n (§ 5.1). To find E_{int} (*green*), I subtract the model flux (*red*) from the observed flux (*black*) in the intermediate-width region. E_n (*blue*) is calculated by subtracting the observed flux from the model flux in the 6560 Å and 6565 Å bins.

Rather then select for models that match observation, I have adjusted this metric to identify a narrow emission-line height ratio which contains enough energy *both* to reproduce the observed narrow-line height *and* to fill in the observed energy in the intermediate-width region. I estimate the excess narrow line energy E_n by subtracting the observed flux from the model flux in the two wavelength bins corresponding

to the narrow region of the line at 6560 Å and 6565 Å. Similarly, I estimate the missing flux in the intermediate-width region of the line, E_{int}, by subtracting the model flux from the observed flux in the wavelength bins corresponding to velocities between $1000 - 3000$ km s^{-1} on both the blue and red sides. The new metric for identifying models with appropriate flux emission is then given by $0 \leq E_n - E_{int} \leq 3$. E_{int} must not exceed E_n if the model is to produce enough line photons to fill in the intermediate region after Doppler velocity shifting. I chose an upper limit of 3 for the value of the difference to account for the approximate nature of the calculation and provide a reasonable limit for which some models are able to be identified. This process is illustrated in Fig. 2.6.

Chapter 3

The geometrical evolution of SN 1997eg over time

3.1 Introduction to SN 1997eg

The bright Type IIn SN 1997eg was discovered by M. Aoki on 1997 December 4 (Nakano and Aoki 1997). The supernova resided in the host galaxy NGC 5012 and was likely between 1 and 2 months old at the time of discovery (Hoffman et al. 2008). In 1997 and 1998, A. Filippenkos group at UC Berkeley obtained several epochs of spectral and spectropolarimetric data on SN 1997eg using the LRIS spectrometer (Cohen 2005) at the Keck II 10-m telescope and the Kast double spectrograph (Miller and Stone 1993) at the Shane 3-m telescope at Lick Observatory. Table 3.1 lists the dates and other information about these observations; more details may be found in Hoffman et al. (2008).

SN 1997eg was very bright at the time of discovery, with an absolute magnitude $-19 < M_V < -18$ (Nakano and Aoki 1997). Its optical spectra consisted of a blue continuum containing many emission lines with multiple components, notably those of the hydrogen Balmer lines and He I. The strongest lines had broad compo-

Table 3.1: Observations of SN 1997eg

Epoch	Day[1]	UT Date	Instrument[2]	Range(Å)
1	16	1997 Dec 20	K2/LP	4296 - 6834
2	44	1998 Jan 17	K2/LP	4320 - 6860
3	93	1998 Mar 7	K2/LP	4314 - 6850

[1] Days since discovery, 1997 December 4 UT (HJD 2,450,787).
[2] L/K = Lick 3 m/Kast Double Spectrograph; K2/L = Keck II 10 m/Low Resolution Imaging Spectrometer (LRIS); K2/LP = Keck II 10 m/LRIS with Polarimeter.

nents with FWHM values of $\sim 10,000$ km s^{-1} and narrow components arising from ionization of the surrounding, nearly stationary CSM. Hoffman et al. (2008) made several estimates of the value of the ISP of 2.9%, 2.0%, and 1.4% and confirmed an earlier CSM density estimate of $1 \times 10^8 - 5 \times 10^7$ cm^{-3} made by Salamanca et al. (2002).

The polarization of hydrogen had a distinct enhanced blue wing and a lack of red enhancement. The region of the line with the enhancement had a polarization angle distinct from the rest that persisted over time. A non-spherical ejecta elongated along one or more axes separate from the CSM was suggested to explain the blue polarization enhancement for SN 1997eg by Hoffman et al. (2008). Any intermediate components arising from this region would then have variations in Q and U that would affect it's level of polarization in comparison. Breaking various axes of symmetry within the model structure to attempt to reproduce effects like this is of great interest, and the addition of asymmetric central source regions is of high priority in the development plans for the immediate future. To simultaneously explain the lack of red polarization enhancement, it was suggested that the surrounding CSM have an equatorially enhanced density inclined edge-on and blocking the view of the receding side.

3.2 Data reduction

To compare the SN 1997eg data with my model grid, I used the Hα line profiles from the epochs listed in Table 3.1 and depicted in Fig. 3.1. I first rebinned the raw spectra to 5 Å for the total flux fitting and 40 Å for the polarization fitting; see §2.3. The intrinsic resolution of these spectra is 2 Å (Table 3.1). The 5 Å binning allows me to sample the line with roughly 2 bins per resolution element, and 40 Å binning improves SNR for the polarization data while maintaining the overall line morphology. I set the blue limit for each spectrum at 6150 Å; the red limit varied from 6760–6865 Å depending on the wavelength range of the individual observations.

In order to keep a constant wavelength bin size when correcting the spectra for the galaxy's recession velocity (v = 2485 km s^{-1}; Hoffman et al. 2008), I applied the redshift correction for the Hα rest wavelength (54.3 Å) to the entire line rather than correcting each wavelength bin for its own redshift. This leads to a difference of no more than 3.4 Å at the line endpoints; with bin sizes of 5 Å or greater, the effect should be negligible. After flux normalization at 6150 Å (6130 Å for the 40-Å polarization spectra), fractional uncertainties in these spectra were approximately 0.4 (0.2).

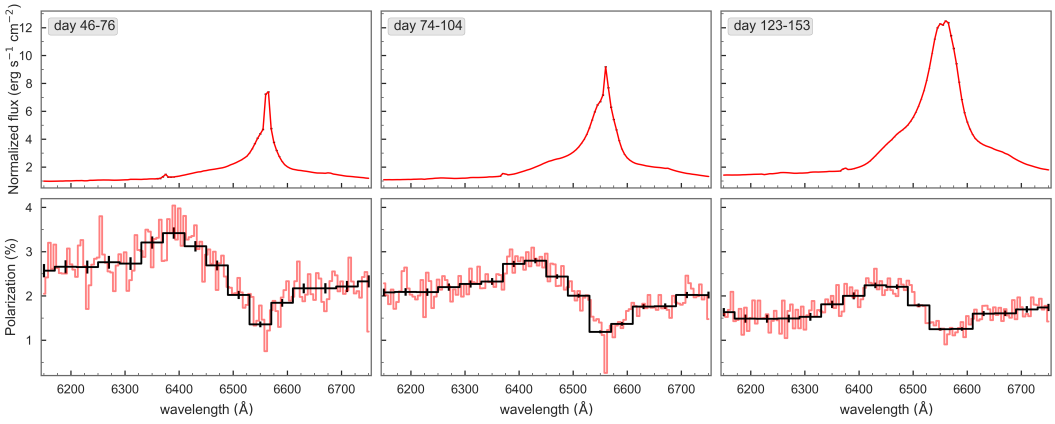

Figure 3.1: Observed flux and polarization data for SN 1997eg at days 16, 44, and 93 (§3.1). Fluxes (top) are normalized to the continuum. Percent polarization (bottom) is shown at 5 Å in red, over-plotted by the 40 Å re-binned spectrum in black.

3.3 Model fitting

In the sections below, I present the results of fitting each epoch of SN 1997eg against my grids of central-source and distributed-source models (described in §2.1). A small amount of uncertainty arises from choosing to use the first epoch of flux from SN 1997eg as the input spectrum for all distributed models. SN 1997eg showed variation in the emission height and shape over the three epochs that certainly affects the shape of the polarization at those later times. The overall line profiles are not entirely dissimilar, but there is still variation in the emission strength and in the size and presence of shoulder components of different widths at all epochs. Use of a single input spectrum for the distributed case is a necessary assumption, however, to avoid having to run a completely new distributed grid for each epoch. I discuss the effects of these uncertainties in appropriate sections below.

I plot combinations of χ^2_ν, flux emission ratio, and polarization shift (discussed in § 2.3.2) for both the entire distribution of models as well as those population of models identified as the cluster with the smallest χ^2_ν values. I vary color to highlight different input parameter values. The best fitting cluster is demarcated by a horizontal grey line in figures with χ^2_ν on the y-axis. Flux emission ratio figures contain a vertical grey line indicating the observed ratio. A red box highlights the area containing models with both low χ^2_ν and appropriate flux emission. For figures depicting the polarization shift, I calculate the average shift of models in the lower cluster and plot it as a vertical dashed line. For each parameter, histograms illustrate changes in the distribution of parameter values among the cluster group. Varying the color of the points reveals several interesting correlations between χ^2_ν, emission ratio, and polarization shift with different model parameters.

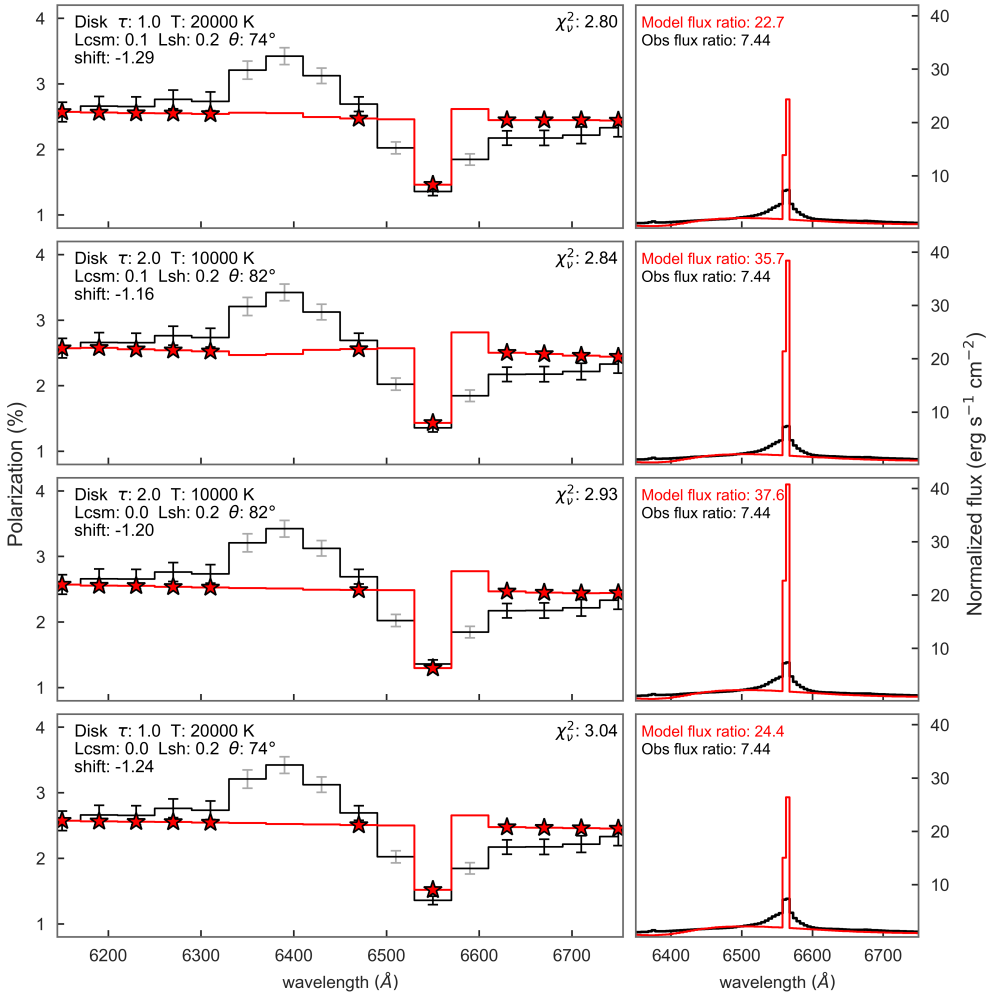

Figure 3.2: Polarization (left) and flux (right) spectra of the four best-fitting disk models (red) in the central-source grid. The observed spectra of SN 1997eg at Epoch 1 are shown in black. Wavelength points included in the fit are marked by red stars.

3.4 Central-source model results

3.4.1 Epoch 1

In Epoch 1, SN 1997eg has an observed flux emission ratio of 7.44 ± 0.06. The best fitting of this group are a set of 4 disk models with χ^2_ν of 2.8 – 3.04, followed by a set of 4 toroid models with χ^2_ν of 3.15 – 3.41. Their parameters are shown in Table 3.2 and flux and polarization spectra are shown in Figs. 3.2 and 3.3. The

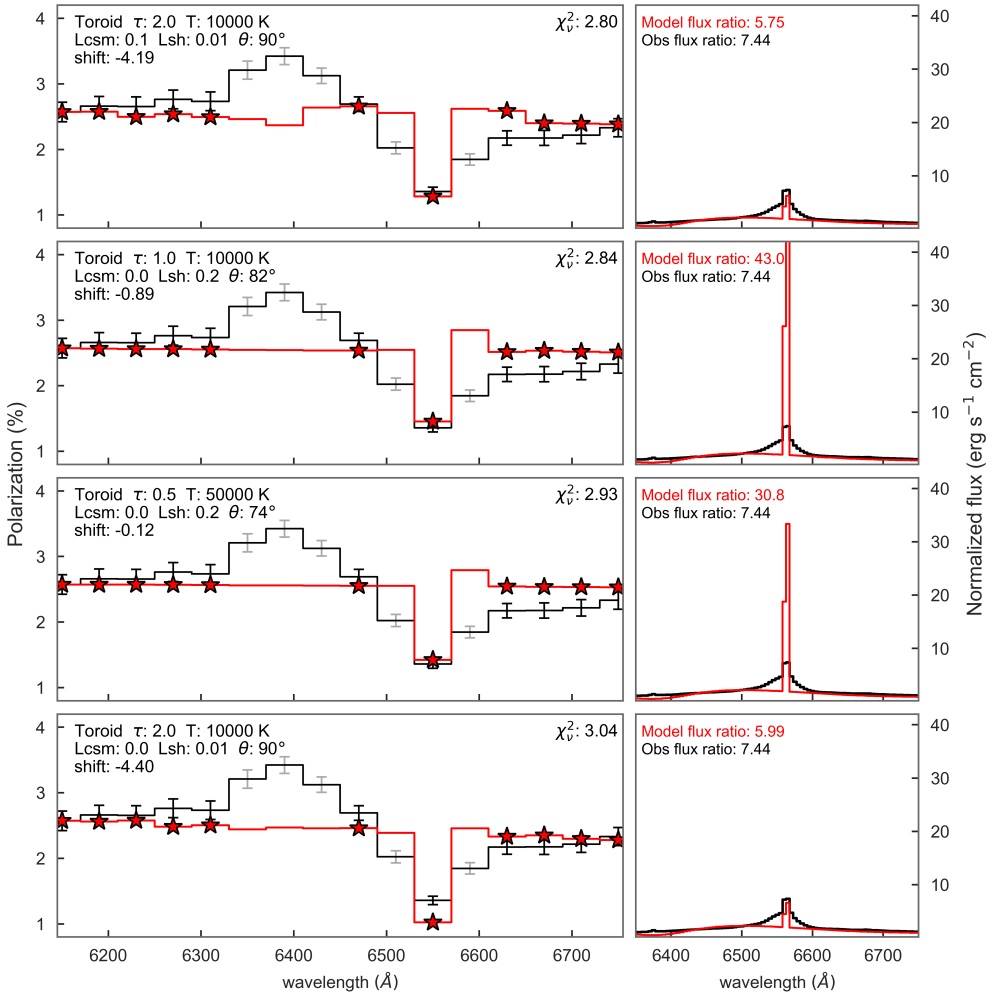

Figure 3.3: Polarization (left) and flux (right) spectra of the four best-fitting toroid models (red) in the central-source grid. The observed spectra of SN 1997eg at Epoch 1 are shown in black. Wavelength points included in the fit are marked by red stars.

combinations of parameters are paired in interesting ways. The two disk models with an optical depth of 1.0 have identical 10,000 K temperatures and inclinations of 74°, while those with an optical depth of 2.0 have temperatures of 20,000 K and a higher inclination of 82°. All four have high $L_{\rm Sh}$ values, but their values of $L_{\rm CSM}$ vary; the CSM brightness appears to have a minimal effect on the fits for these models.

Table 3.2: Central Models with Best-Fitting Polarization, Epoch 1 of SN 1997eg

Parameters	Models							
Geometry	disk	disk	disk	disk	tor.	tor.	tor.	tor.
Optical Depth	1.0	2.0	2.0	1.0	2.0	1.0	0.5	2.0
$L_{\rm CSM}/L_{\rm SN}$	0.1	0.1	0.0	0.0	0.1	0.0	0.0	0.0
$L_{\rm Sh}/L_{\rm SN}$	0.20	0.20	0.20	0.20	0.01	0.20	0.20	0.01
Temp. (10^3 K)	20	10	10	20	10	10	50	10
Inclination (°)	74	82	82	74	90	82	74	90
ρ (10^{-12} g cm^{-3})	4.79	9.59	9.59	4.79	71.8	35.7	17.8	71.8
$n_{\rm e}$ (10^{12} cm^{-3})	2.84	5.67	5.67	2.84	40.0	20.0	10.0	40.0
Emission Ratio	22.8	35.8	37.6	24.4	5.76	43.1	30.8	5.99
Pol. Shift (%)	-1.29	-1.16	-1.20	-1.24	-4.19	-0.89	-0.12	-4.40
χ^2_ν	2.80	2.84	2.93	3.04	3.15	3.33	3.41	3.41
A^2	0.28	0.34	0.47	0.42	0.42	0.44	0.52	0.23

The four toroid models that follow display a similar pattern of matching parameters. The two with high optical depths of 2.0 also have low LSh, $T = 10,000$ K, and an edge-on (90°) inclination. Their CSM luminosities are split like those of the disk models, again with the higher $L_{\rm CSM}$ corresponding to a marginally better fit. The other two toroid models both have high LLSh and $L_{\rm CSM} = 0$. However, the model with an optical depth of 1.0 has a low temperature of 10,000 K and an inclination of 82°, while the other has an optical depth of 0.5, a high 50,000-K temperature and a lower inclination of 74°. The only two models of these 8 with the lowest χ^2_ν that come close to reproducing the flux emission ratio of the line peak to the continuum are the toroids with optical depth of 2.0.

Fig. 3.4 displays all the central-source models in emission ratio-polarization shift space. Two distinct groups of central-source models are identifiable in this population: one with emission ratios ranging from about $10 - 40$ times that of the continuum, and one with an average of about $4 - 5$ times that of the continuum, both above and below the observed emission ratio. Membership in the two populations is driven almost exclusively by the $L_{\rm Sh}$ parameter. As described in section 2.1, the

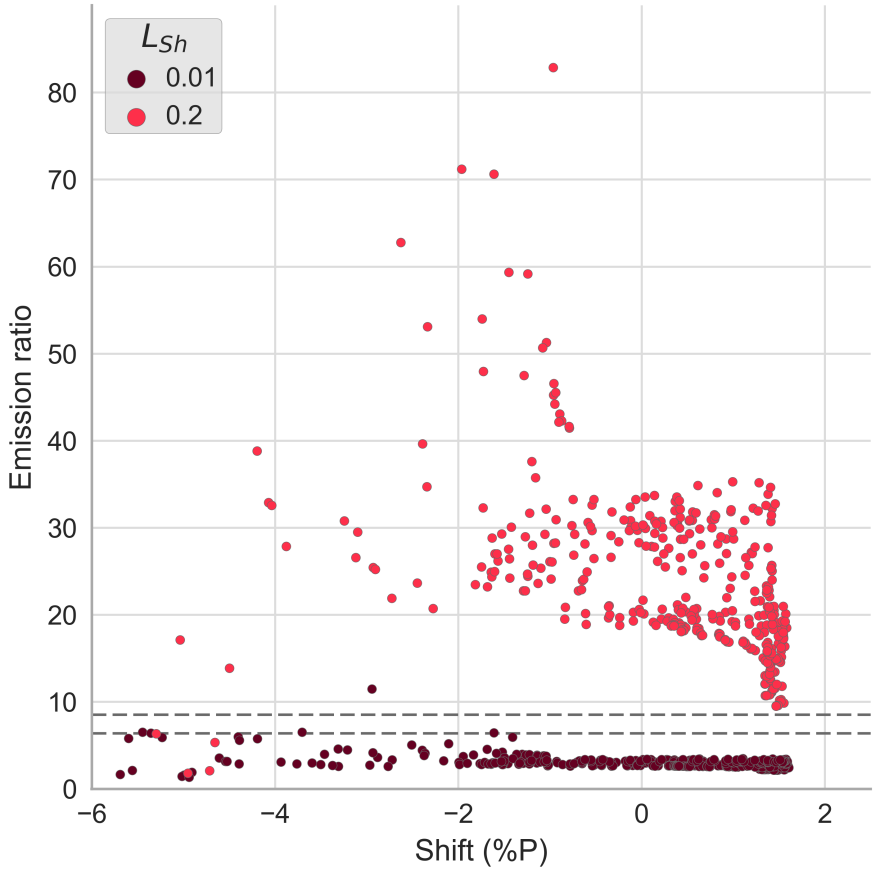

Figure 3.4: Polarization shift vs. emission ratio for all models. Two distinct populations are visible with distinct emission-ratio values. Models generating these populations are differentiated by their $L_{\rm sh}$ parameter values (point colors). The observed emission ratio of 7.44 for Epoch 1 of SN 1997eg is within the region bounded by the horizontal dashed grey lines.

shock region exclusively emits a large amount of line photons. It is therefore not entirely surprising that increasing the relative luminosity of this region would cause a large difference in the height of the model flux emission lines and an increase in its ratio to the continuum. This separation persists as χ^2_ν drops into the low cluster. There appears to be a preference for higher $L_{\rm Sh}$ among models with better fits in polarization. However, this does not appear to correspond to a good match to the observed flux emission ratio at first glance.

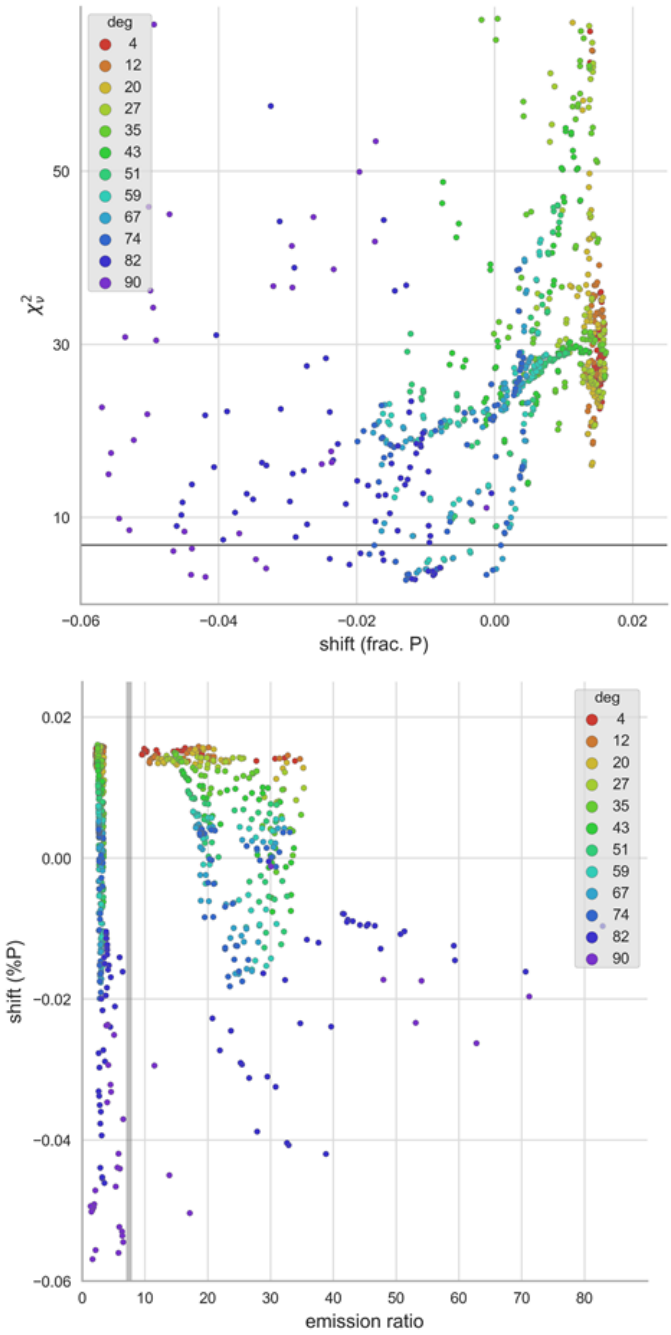

Figure 3.5: Top: χ^2_ν vs. polarization shift for all central-source models, colors corresponding to model viewing angle (0° is pole-on, 90° is edge-on). The grey horizontal line marks separation of the cluster with lowest χ^2_ν values. Bottom: Models with high inclination require a greater continuum shift downward in polarization (top), but also consistently produce the lowest χ^2_ν values (bottom)

Viewing angle, on the other hand, is strongly correlated with low values of χ^2_ν, as well as a greater negative shift in polarization. Fig. 3.5 shows all the central-source models color-coded by inclination angle. As inclination increases from 0° (pole-on) to 90° (edge-on), the models produce higher levels of continuum polarization, which require a larger negative shift to match the observed Epoch 1 spectrum. Additionally, the region of parameter space with low χ^2_ν is exclusively populated by the same high inclination models. High inclination results in a good match for the depolarization at line center; otherwise, these models would not fit so well once shifted downward at the blue end.

The density of the CSM in the models is driven primarily by geometry and optical depth. The disk models have a larger volume and therefore a lower density then toroids for equal optical depths. When models in the low χ^2_ν cluster are separated by geometry, $L_{\rm Sh}$, and inclination, patterns emerge for the models with the very lowest χ^2_ν values (discussed at the beginning of this section; Fig. 3.6). 46 models are identified as belonging to a cluster with the lowest χ^2_ν values, requiring an average polarization shift of -1.53%. No disk models with $L_{\rm Sh} = 0.01$ are present in this cluster. Models with the higher shock luminosity of 0.2 are further subdivided into two groups. Those inclined between $59° - 82°$ require a consistent reduction in polarization of about 1% but also produce an emission ratio that is too high. Two disk models at 90° produce the correct emission strength but require an inconsistent drop in polarization of 4.5% and 7.5%. Toroids of both $L_{\rm Sh}$ values are present, but they behave quite differently. Toroid geometries with $L_{\rm Sh} = 0.01$ reproduce the emission ratio well and are all inclined at $82° - 90°$, but there is some dispersion in their polarization shift from 1% to a little over 4%. Toroids with $L_{\rm Sh} = 0.2$, like the disks, are more consistent with their polarization shift but produce emission lines that are stronger than observed.

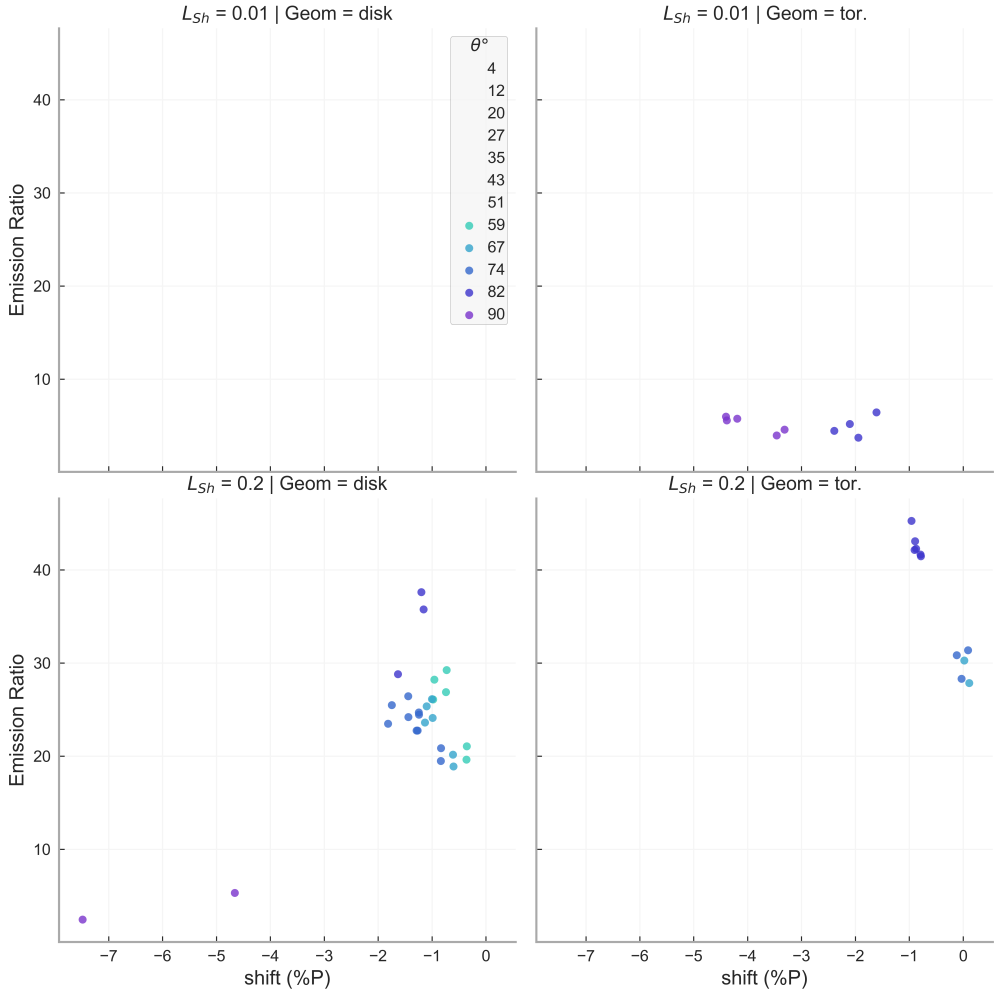

Figure 3.6: Polarization shift vs. emission ratio of models in the low χ^2_ν cluster, separated by geometry (columns) and shock luminosity (rows) and colored according to inclination angle. The low χ^2_ν cluster is comprised only of models with inclination over 59°, and the only toroidal geometries are constrained to 82° and 90°. The upper left panel is blank as there are no disk models with low $L_{\rm Sh}$ in the low χ^2_ν cluster.

3.4.2 Epoch 2

SN 1997eg has an observed flux emission ratio of 6.99 ± 0.05 for Epoch 2. There is a reduction in observational uncertainties in the second epoch of data for SN 1997eg. This results in lower χ^2_ν values overall.

The best fitting models in polarization are shown in Figure 3.7, and their parameters listed in Table 3.3. A comparison of the two models at the bottom of this figure

Table 3.3: Central Models with Best-Fitting Polarization, Epoch 2 of SN 1997eg

Parameters	Models							
Geometry	disk	disk	disk	tor.	disk	disk	tor.	tor.
Optical Depth	0.5	0.5	1.0	1.0	1.0	1.0	0.5	2.0
$L_{\rm CSM}/L_{\rm SN}$	0.1	0.0	0.0	0.0	0.1	0.0	0.1	0.0
$L_{\rm Sh}/L_{\rm SN}$	0.2	0.2	0.2	0.01	0.2	0.2	0.2	0.01
Temp. (10^3 K)	10	10	20	50	20	20	50	50
Inclination (°)	74	74	67	82	67	74	67	82
ρ (10^{-12} g cm^{-3})	2.39	2.39	4.79	35.6	4.79	4.79	17.8	70.9
$n_{\rm e}$ (10^{12} cm^{-3})	1.41	1.41	2.84	20.0	2.83	2.83	10.0	39.8
Emission Ratio	19.5	20.9	20.9	25.4	23.6	24.4	27.8	6.44
Pol. Shift (%)	-0.44	-0.44	-0.70	-1.71	-0.73	-0.84	0.50	-1.21
χ^2_ν	10.85	10.92	10.93	11.34	11.34	11.65	11.85	11.90
A^2	0.54	0.56	0.74	0.60	0.73	0.48	0.42	0.57

provides an interesting look at two models that produce a similar fit in polarization, but have very different physical parameters. A toroid with low shock luminosity, high temperature, and greater inclination produces a fit to the polarization that is nearly identical to the fit provided by a disk with high shock and CSM luminosity, 20,000 K temperature, and lower inclination angle. However, there is a substantial difference in flux emission. Greater depolarization across the line in the disk model results from a smaller escaping fraction of polarized line photons. In the disks, the overall amount of line emission is greater because of the high shock luminosity. For the toroids, the higher temperature means a taller emission spike from the shock and CSM, as well as a more transparent CSM which allows more line photons through. Despite emitting only a third of the flux, the toroid parameters result in the same net percentage of photons being polarized.

I identified a cluster of 58 models with χ^2_ν values below 20 when fitted against the second epoch. These models required an average polarization shift of $-1.04\pm0.24\%$. The same general trends with parameter values seen in Epoch 1 persist in Epoch 2, and the distributions look very similar. There is still a strong preference for

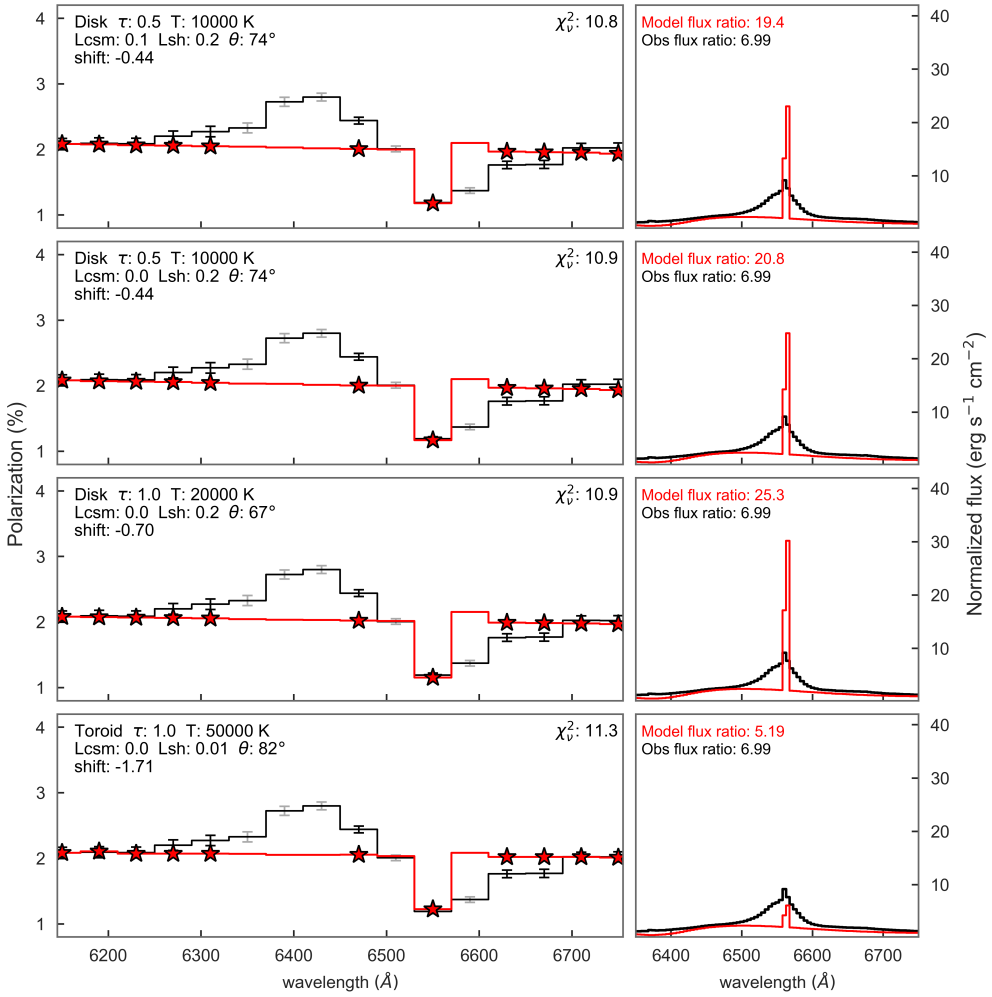

Figure 3.7: Polarization (left) and flux (right) spectra of the four best-fitting models (red) in the central-source grid. The observed spectra of SN 1997eg at Epoch 2 are shown in black. Wavelength points included in the fit are marked by red stars.

high shock luminosity despite the fact that it produces too much line flux. One notable difference between Epochs 1 and 2 is a change from a preference for lower (10,000 K) temperatures to higher ones (50,000 K for Epoch 2). This could indicate a brightening of the shock region, injecting more energy into the CSM and heating it. There is a corresponding preference for high shock luminosity among the low cluster, with the high value being 4 times more prevalent. The fits to the Epoch 1 data showed a strong preference for an optical depth of 0.5 among the low cluster

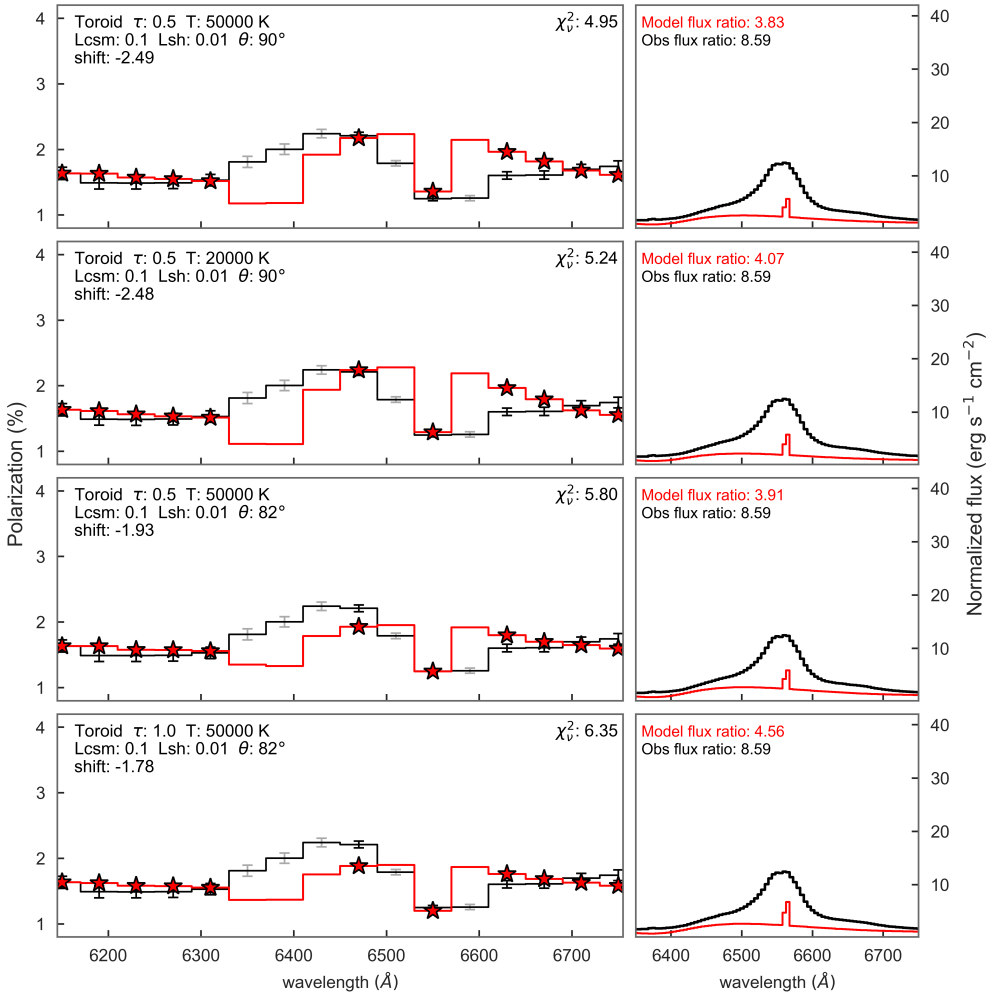

Figure 3.8: Polarization (left) and flux (right) spectra of the four best-fitting models (red) in the central-source grid. The observed spectra of SN 1997eg at Epoch 3 are shown in black. Wavelength points included in the fit are marked by red stars.

models, yet all the best-fitting models had $\tau = 1.0$ or 2.0. In the case of Epoch 2, models with the lowest χ^2_ν better reflect the overall distribution of the cluster, with more having lower optical depth values.

3.4.3 Epoch 3

The Hα flux emission line is considerably stronger compared to continuum levels and much wider in Epoch 3, with an observed flux emission ratio of 8.59 ± 0.04, and

the narrowest component of the line becoming much less prominent in comparison to the intermediate and broad components. Their parameters are listed in Table 3.4, the spectra of the 4 models with the lowest χ^2_ν are shown in Figure 3.8. The 8 best fitting models are predominantly toroids of optical depth 0.5 and 1.0, low shock luminosity. This is a departure from the trends seen for Epochs 1 and 2, for which the 8 models with the lowest χ^2_ν are predominantly disks with high shock luminosity. Also of note is that these 8 models are all inclined to 82° and 90° and have the higher CSM luminosity. These models all produce flux emission much lower than observation; the highest ratio among them is 5.04, compared to the observed of 8.6.

A total of 27 models are identified as belonging to a low χ^2_ν cluster, which require an average polarization shift of $-2.11 \pm 0.26\%$ to best fit the observed spectrum. The parameters of these models do widen to include some disks of similar optical depth and inclination to the toroids discussed above, all also of higher temperatures, as well as some of the same toroids but with lower inclinations between $59° - 74°$. Low cluster models with Gaussian residuals maintain the same parameter trends as the models with the lowest 8 χ^2_ν.

The level of polarization in the spectrum of SN 1997eg is lower in Epoch 3 then at previous times, between about $1 - 2\%$. This is interesting, given the generally high inclination and low flux emission of the best fitting models. Models with higher density and more extreme axial flattening are required in order to produce the appropriate percentages of polarized photons from the continuum and narrow line regions. These types of CSM scenarios are generally associated with larger levels of polarization, and indeed these models require a greater polarization shift to match the spectrum. This could indicate the revealing of inner regions of the ejecta that are more heavily inclined, but would also necessitate a larger change in the ISP contribution at late times.

Table 3.4: Central Models with Best-Fitting Polarization, Epoch 3 of SN 1997eg

Parameters	Models							
Geometry	tor.	tor.	tor.	tor.	tor.	tor.	tor.	disk
Optical Depth	0.5	0.5	0.5	1.0	0.5	1.0	1.0	2.0
$L_{\rm CSM}/L_{\rm SN}$	0.1	0.1	0.1	0.1	0.1	0.1	0.1	0.0
$L_{\rm Sh}/L_{\rm SN}$	0.01	0.01	0.01	0.01	0.01	0.01	0.01	0.01
Temp. (10^3 K)	50	20	50	50	20	50	20	50
Inclination (°)	90	90	82	82	82	90	82	82
ρ (10^{-12} g cm^{-3})	17.8	17.8	17.8	35.6	17.8	35.6	35.6	4.82
$n_{\rm e}$ (10^{12} cm^{-3})	10.0	10.0	10.0	20.0	10.0	20.0	20.0	2.84
Emission Ratio	3.83	4.07	3.91	4.56	4.10	5.05	3.33	2.86
Pol. Shift (%)	-2.49	-2.48	-1.93	-1.78	-1.68	-2.62	-1.46	-4.48
χ^2_ν	4.96	5.24	5.80	6.36	7.21	8.26	10.79	11.90
A^2	0.37	0.63	0.57	0.57	0.80	0.49	1.36	1.62

3.5 Distributed-source models

Distributed-source models do not generate sufficient depolarization across the narrow line region to successfully reproduce the polarization behavior of SN 1997eg at any epoch. The use of the flux spectrum from the first epoch of SN 1997eg as input does not give these models an advantage in fitting the flux emission ratios. While these models do closely reproduce the ratio of emission as seen in observations, there are no models at any epoch with enough excess area in the narrow portion of the line to feasibly fill in the intermediate and broad regions under the influence of Doppler shifting from the velocity of the CSM and shock regions. In general, the fits are also much poorer then for central source models. The lowest χ^2_ν values for fits from each epoch are 11.4, 26.2, and 15.4, respectively, which are quite poor. Additionally, almost no models identified as part of the lowest χ^2_ν cluster for each epoch have residuals consistent with a normal distribution by the A^2 metric. Regardless, I will briefly discuss the trends for these models and the properties of the few models with the lowest χ^2_ν values. The parameters for the 2 models from each epoch with the lowest χ^2_ν values are shown in Table 3.5, and their spectra are shown in Figure 3.9.

Table 3.5: Distributed Models with Best-Fitting Polarization, all Epochs of SN 1997eg

Parameters	Epoch 1		Epoch 2		Epoch 3	
Geometry	tor.	disk	tor.	disk	tor.	tor.
Optical Depth	2.0	2.0	2.0	2.0	2.0	2.0
$L_{\rm CSM}/L_{\rm SN}$	0.0	0.0	0.0	0.0	0.0	0.1
$L_{\rm Sh}/L_{\rm SN}$	1.0	1.0	1.0	1.0	1.0	1.0
Temp. (10^3 K)	50	50	50	50	50	50
Inclination (°)	90	82	90	82	90	90
ρ (10^{-12} g cm^{-3})	70.9	9.55	70.9	9.55	70.9	70.9
$n_{\rm e}$ (10^{12} cm^{-3})	39.8	5.65	39.8	5.65	39.8	39.8
Emission Ratio	12.2	7.79	12.2	7.79	12.2	10.1
Pol. Shift (%)	-1.06	-4.45	-0.67	-4.07	-1.14	-0.88
χ^2_ν	11.3	16.2	26.2	40.2	15.4	16.9
A^2	0.95	1.33	0.59	0.94	0.93	0.94

The same distributed model is the best-fitting in polarization in all three epochs by a decent margin. This model has toroidal CSM, low CSM luminosity, high optical depth of 2.0, high temperature of 50,000 K, and edge-on inclination of 90°. In Epochs 1 and 2, the second best model is a disk with the same optical depth, CSM luminosity, and temperature, with a slightly lower inclination of 82°. This model has some parameters in common with most models from Epoch 3, namely the toroidal CSM, high inclination, and high temperature. However, this distributed toroid differs in its higher optical depth and lack of CSM luminosity. I note that even though this model is of higher optical depth and density, it results in far higher flux emission ratios then those of the central grid. Despite the increase in escaping line photons at this inclination, the distributed model fits does a poorer job in fitting the depolarization near the line then its low optical depth central counterparts.

The lower depolarization in the distributed-source models can potentially be attributed to the fact that all photons in these models are emitted just interior to the CSM rather than from the center of the grid. Thus, for any given photon, there are fewer directions of propagation that lead to immediate escape without encountering

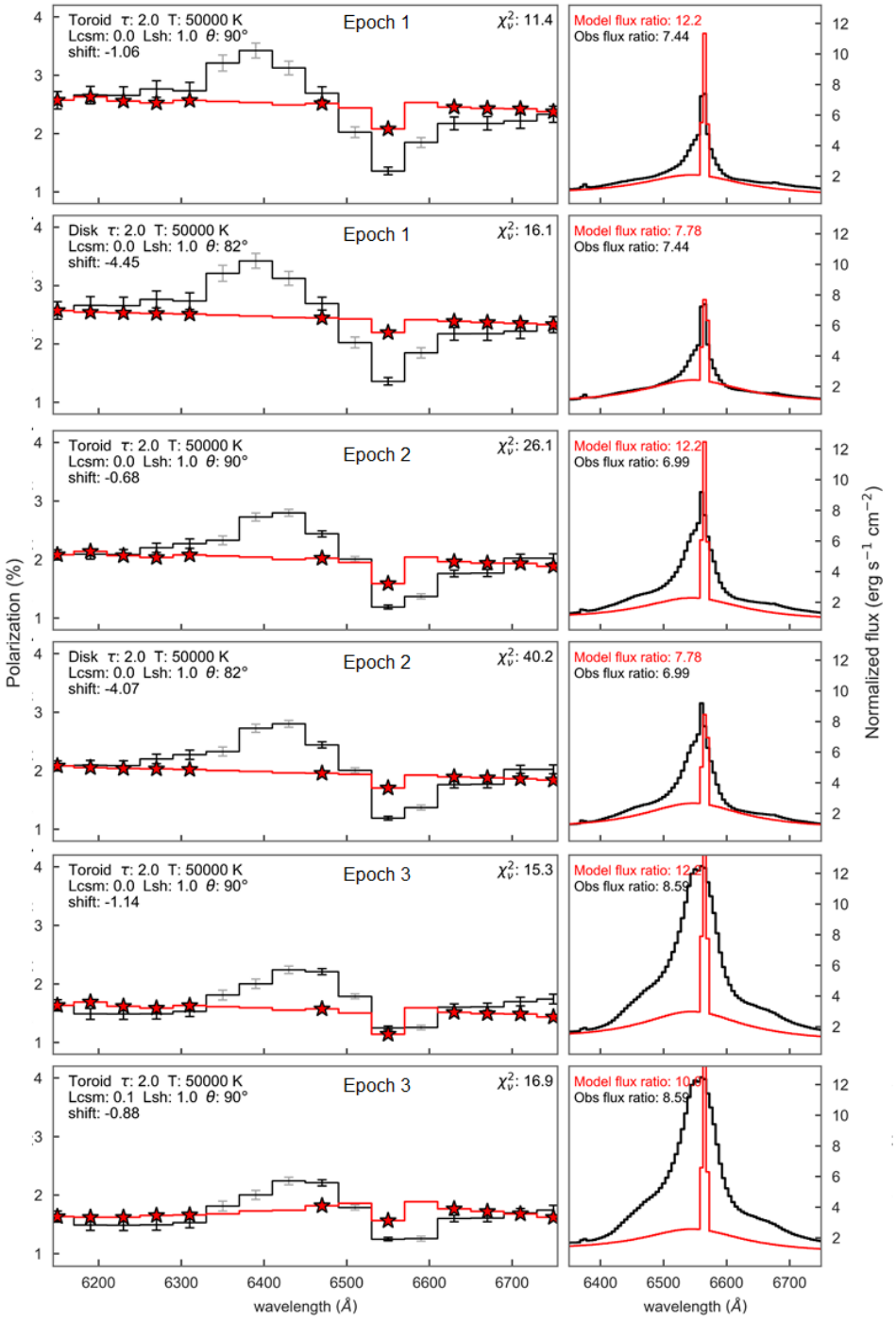

Figure 3.9: Polarization (left) and flux (right) spectra of the two best-fitting models (red) in the distributed-source grid at each epoch. The observed spectra of SN 1997eg are shown in black. Wavelength points included in the fit are marked by red stars.

the CSM. This means there is a greater probability for distributed-source photons to enter the CSM and become polarized than for central-source photons. In the distributed-source models, the fraction of line photons that are polarized increases compared to the total emitted, and the depolarization trough becomes shallower.

At 90° this effect is enhanced because at this inclination the projection of the contact surface between the CSM and shock regions in the line of sight is largest. More of the generated photons are directed along a path pointing radially outward along the thickest path of the CSM at 90°. Even though the CSM is of higher optical depth in the best-fitting model in the distributed case compared to central, the higher temperature and ionization fraction allow more line photons to pass through without being absorbed. Either too large a percentage of them are being scattered and polarized to match what is seen in the observed spectrum, or not enough are being emitted in the line region in the first place. The fact that the most recent changes to *SLIP* deal with a new mechanism for the emission of photons, I suspect the issue is with the latter. If it is true that emission from CSM interaction is the mechanism underlying the characteristics of a IIn spectrum then something is missing from the *SLIP* models concerning the way photon wavelengths are sampled and then emitted from the shock region.

3.6 Discussion

In Epoch 1, corresponding to day 16 post-discovery, a good fit in polarization can be achieved by models with inclinations greater than 60° where shock luminosity is high for both disk and toroidal geometries. In Epoch 2, day 44 post-discovery, the acceptable range of inclinations widens but the pattern of toroids being restricted to the highest two inclination bins persists. Disk models with high shock luminosity favor slightly lower inclinations and generate relatively consistent amounts of excess in continuum polarization, and equally favor optical depths of 0.5 to 1.0 over all

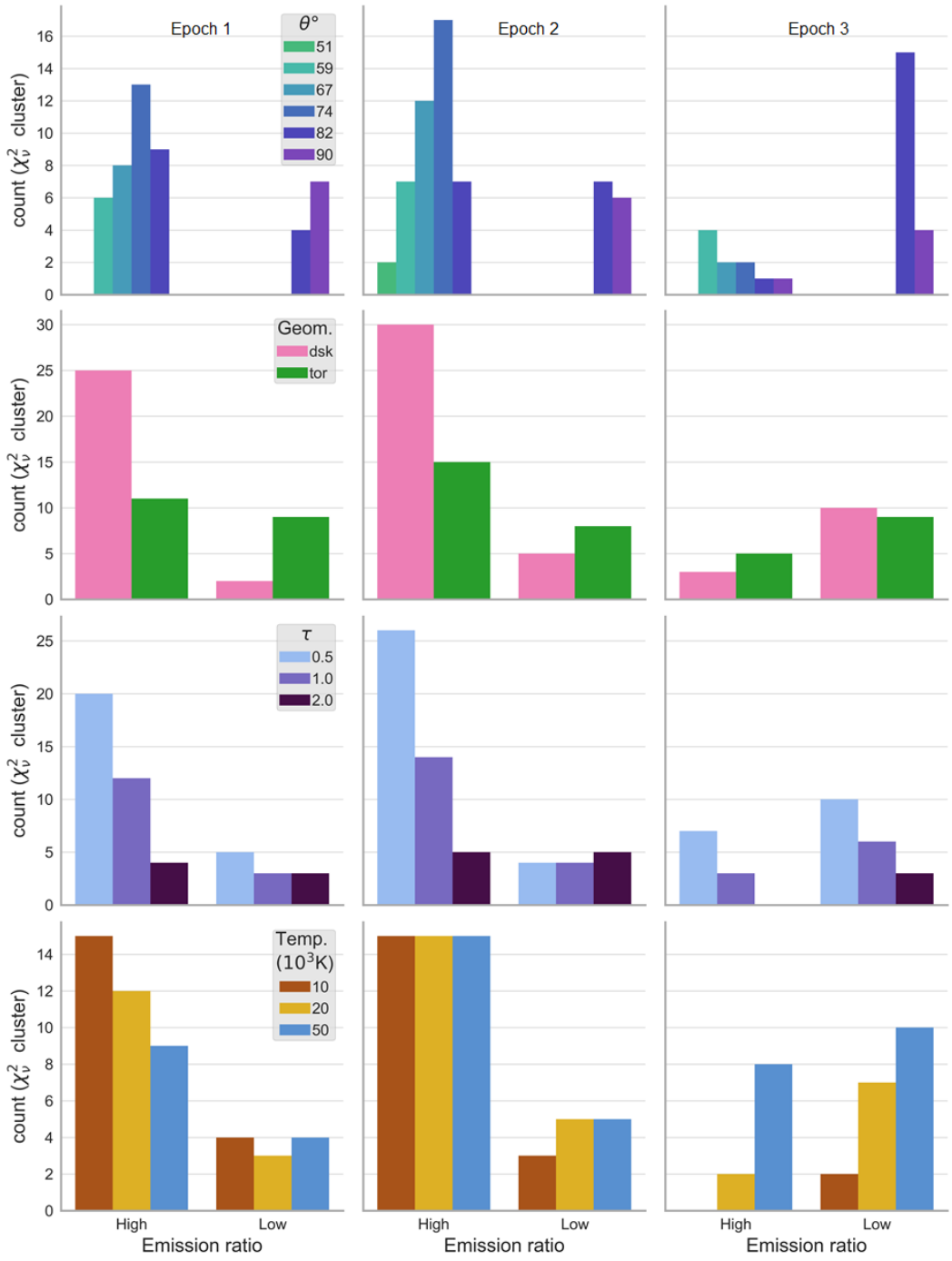

Figure 3.10: Occupation of parameter values by central-source models in the two subpopulations of the low χ^2_ν cluster for SN 1997eg; one with high emission ratios above the observed value are to the left of each axis, and those with low emission ratios are on the right. Epochs 1 to 3 are in columns from left to right. Inclination, CSM geometry, LSh, and optical depth are in rows from top to bottom.

three epochs. The best-fitting toroids tend to lower slightly in optical depth over time, from about 1.0 closer to 0.5. Temperatures tend to increase in both cases. The changes in distribution of several parameters over time (observational epoch) for models within the low χ^2_ν cluster are depicted in Fig. 3.10.

The bimodal nature of the trends in the lowest cluster of models suggests two different potential explanatory scenarios for SN 1997eg that are degenerate in the polarization behavior they produce, each with caveats relating to current model limitations and implications based on observations of SN 1997eg. Below I discuss both of these proposed scenarios.

1. *Toroidal CSM with low shock luminosity*: One scenario describing SN 1997eg, based on my model fits, is an equatorially confined CSM with a density defined by the toroidal models, viewed very close to edge on. The luminosity of the shock is low compared to the luminosity of the SN at the center, resulting in emission line strengths that are close to observations of SN 1997eg, but not high enough to meet the line area metric. The CSM thins slightly between day 16 and day 44 from higher density of approximately 3.5×10^{-11} g cm^{-3} associated with optical depth of 1.0, down toward the lower density of around 2×10^{-11} g cm^{-3} associated with optical depth of 0.5, which would correspond to some falling radial density profile. However this conflicts with the tendency toward increasing temperatures over time, suggesting the injection of more energy into the CSM from the shock region and requiring that the shock encounter clumps or higher density CSM.

Toroids with high shock luminosity produce an emission ratio that is too high to potentially be corrected for by Doppler velocity wavelength adjustments of photons in the spike. The excess intensity under the narrow line in the model is far greater then the intensity deficit under the intermediate wings of the observed polarization spectra which removes them from further consideration. Additionally, these models

Table 3.6: Models of Special Interest for Epochs 1 and 2 of SN 1997eg

Parameters	Epoch 1	Epoch 2					
Geometry	disk	disk	disk	disk	disk	disk	disk
Optical Depth	0.5	0.5	0.5	1.0	1.0	0.5	2.0
$L_{\rm CSM}/L_{\rm SN}$	0.1	0.1	0.1	0.1	0.1	0.1	0.1
$L_{\rm Sh}/L_{\rm SN}$	0.2	0.2	0.2	0.2	0.2	0.2	0.2
Temp. (10^3 K)	10	20	50	20	50	20	20
Inclination (°)	67	67	74	74	74	74	74
ρ (10^{-12} g cm^{-3})	2.39	2.40	2.40	4.79	4.79	2.40	9.55
$n_{\rm e}$ (10^{12} cm^{-3})	1.41	1.42	1.42	2.84	2.84	1.42	5.65
Emission Ratio	18.9	24.1	24.2	22.8	23.5	22.7	22.8
Pol. Shift (%)	-0.60	-0.59	-1.04	-0.89	-1.42	-0.86	-0.30
χ^2_ν	5.33	12.25	12.67	12.71	13.82	15.34	19.51
A^2	0.33	0.57	0.60	0.43	0.56	0.42	0.48

Models of special interest for each epoch

are inconsistent in the level of continuum polarization they produce and results in a very wide range in polarization shift.

2. *Disk with high shock luminosity*: The second scenario describing SN 1997eg is a CSM of density defined by the disk models illuminated by a shock with high luminosity and viewed at slightly lower inclinations between 67° and 90°. Disks in this range that produce consistent polarization excess are between 67° and 82° in inclination. There is not a significant change in the optical depth, with models of both optical depth 0.5 and 1.0, corresponding to mass densities of around $2-5\times10^{-12}$ g cm^{-3}.

I have identified several central-source models of particular interest for epochs 1 and 2 of SN 1997eg; these have χ^2_ν that place them in the low cluster, A^2 values below the critical value confirming Gaussian residuals, and emission ratios within the narrow to intermediate line area metric, all of which are discussed in section 2.3.2. Their parameters are tabulated in Table 3.6. The only models fitting these criteria are disks of high shock luminosity with inclination of $67° - 74°$. This effec-

tively eliminates the toroid scenario described above in favor of the disk scenario. I predict that the incorporation of Doppler velocity broadening effects will reduce the height of model emission spikes for all models, redistributing those photons into the intermediate-width regions of the line. This would result in better reproduction of the emission line strength in a greater portion of high LSh disk models that already fit well in polarization.

Models at inclinations closer to face-on produce low overall levels of polarization that necessitate their being shifted upward to match the observed polarization spectrum. By contrast, models at low inclination produce high levels of continuum polarization and must be shifted downward in the negative direction. Closer to face-on, there is no appreciable difference in the amount of polarization shift required between models of each geometry. At 90°, effects from geometry become apparent: disks produce higher polarization and require larger negative shifts, and this effect is more pronounced with increasing optical depth. Greater polarization arises either from a larger fraction of photons scattering multiply in the same direction, or less dilution by unpolarized photons (or both). At inclinations close to edge-on, the only appreciable difference between the CSM of disk and toroidal geometries is their density (Table 2.3). As disks are less dense then toroids for the same optical depth and temperature, more photons are able to penetrate the CSM with fewer interactions. Increasing the optical depth increases the number of scatters and the probability of absorption, both of which act to increase the fraction of escaping photons that are polarized.

For the central-source grid at all epochs, high shock emission and inclination are the parameters behind the large fraction of models that fit best in polarization. The models that best match the Hα emission strength are those with disk geometry, which are considerably less dense then toroids for the same optical depth and temperature due to their larger radial thickness. Increasing asymmetry at the higher

inclinations clearly plays a role in the over all level of polarization in a model, but there also appears to be a contribution from the density of these models that depends on the amount of material in the line of sight at each inclination. The effect of these CSM characteristics, as well as a discussion of the ISP estimates based on the parameters of the models of interest, are considered in Chapter 5.

Chapter 4

The geometrical evolution of SN 2010jl over time

4.1 Introduction to SN 2010jl

SN 2010j was an extremely luminous supernova discovered on 3 November 2010 by Newton and Puckett (2010) in the irregular galaxy UGC 5189A (redshift $z = 0.011$) in the constellation Leo. The first spectrum, taken on day 2 post-discovery, revealed characteristic strong emission lines of H and weaker He on a blue continuum, classifying it as a type IIn (Benetti et al. 2010). Follow-up investigation by Smith et al. (2011a) on Nov. 5 through Nov. 7 of 2010 estimated its peak luminosity at $M_V \sim 20.6$ and proposed an initial progenitor mass of at least 30 $M_\odot$. These authors also measured the narrow and intermediate-width components of the Hα line to have FWHM values of 160 km s^{-1} and 1800 km s^{-1}, respectively.

Observations by Patat et al. (2011) approximately 15 days post-discovery included the first early spectropolarimetric analysis. From their low-resolution flux spectra, these authors estimated the width of the narrow line to be 640 km s^{-1} and that of the intermediate-width line to be $2,400$ km s^{-1}; they also identified a broad

component with FWHM $10,500$ km s^{-1}. The Milky Way ISP contribution was estimated at $\leq 0.2\%$ due to the SN's line-of-sight direction out of the Galactic plane and away from the Galactic center. The host galaxy ISP was estimated at a maximum of 0.3%, placing the total ISP contribution at an upper limit of around 0.5%. These estimates were made via the equivalent widths of the D_2 components of Na I lines in both the spectra of SN 2010jl and that of two foreground stars near the position of UGC 5189A. Polarization of the continuum was relatively constant, averaging around 2% across the spectrum, with deep depolarizations across the Balmer and He I emission lines. Hα was symmetrically depolarized by -1.7% with a constant position angle in the intermediate and narrow regions of the line. The authors made comparisons to models from Höflich (1991) and attributed the early polarization behavior to electron scattering in an aspherical CSM with an axial ratio of ≤ 0.7.

Long term multi-wavelength studies provide observational estimates of several CSM wind characteristics. Fransson et al. (2014) examined photometry and spectrometry data for SN 2010jl over a time period spanning 1100 days post discovery in optical, ultraviolet, and near-infrared. Their work estimated a CSM expanding at a velocity of 105 km s^{-1} with a wind-like density profile of $\rho \sim r^{-2}$, and estimates the total mass lost at a lower limit of $3M_{\odot}$ at a rate of about $0.1M_{\odot}\mathrm{yr}^{-1}$. Examination of the narrow emission line ratios yield an electron density estimate of $3 \times 10^6 - 10^8$ cm^{-3}. Combined optical, ultraviolet, and X-ray studies by Ofek et al. (2014) find an ejected CSM mass in the range of 10 to 16 $M_{\odot}$ the bulk of which lies below a radius of approximately 2×10^{16} cm, but with a wider range of velocities between $70 - 300$ km s^{-1} and ejection time preceding explosion on the order of tens of years.

The SNSPOL collaboration carried out a multi-epoch spectropolarimetric campaign on SN 2010jl, obtaining 11 epochs of data between 2010 and 2012 with the SPOL spectropolarimeter at three University of Arizona telescopes (Williams et al.,

in prep.). In this work, I examine epochs 3 through 5 only, because their early-time evolution provides a useful comparison with those of SN 1997eg (Chapter 3). I present relevant information about these observations, corresponding to days 25–137 post-maximum, in Table 4.1.

4.2 Data reduction

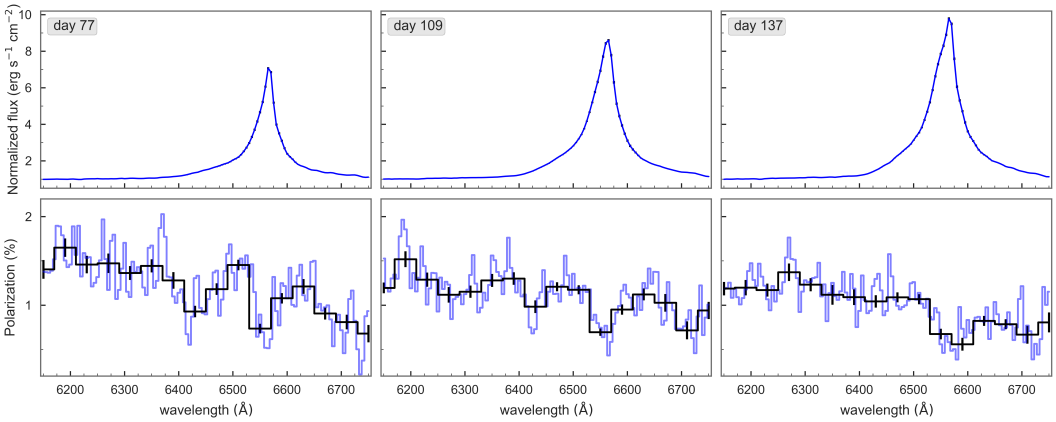

Figure 4.1: Observed flux (top) and polarization(bottom) data of the Hα line for both SNe at all three comparison epochs. Time increases from left to right with SN 1997eg (red) at days 46–76, 74–104, and 123–153, and SN 2010jl at days 77, 109, and 137 post-discovery. (§ 4.1). Fluxes (top) are normalized to the continuum at 6130 Å. Percent polarization (bottom) is shown at 5 Å in red, over-plotted by the 40-Å re-binned spectrum in black.

I carried out Hα line comparisons between SN 2010jl data and my *SLIP* model grid in a manner similar to the process for SN 1997eg (§3.3). I depict spectra from the epochs listed in Table 4.1 in Fig. 4.1. The intrinsic resolution of these spectra is 4 Å; I rebinned the raw spectra to a resolution of 5 Å for the total flux fitting and to 40 Å for the polarization fitting (§2.3). 40 Å binning improves SNR for the polarization data while maintaining the overall line morphology. For the best comparison with SN 1997eg results, I set the blue limit for each spectrum at 6150 Å and the red limit at 6750 Å. I normalized the flux spectra at the bluest point in order to compare the strength of emission relative to the continuum across epochs

Table 4.1: Early-Time SPOL Observations of SN 2010jl

Start Date (UT)	MJD	Days Post-max[a]	Aperture (″)	Q/U Exp. Time[b] (s)	Airmass
Epoch 1[c] , Day 25, 61” Kuiper					
2010 Nov 10 10:58:53	55510.96	23	4.1	240	1.42
2010 Nov 10 11:09:47	55510.96	23	4.1	240	1.37
2010 Nov 10 12:37:47	55511.03	23	4.1	240	1.13
2010 Nov 11 11:01:25	55511.96	24	4.1	480	1.39
2010 Nov 12 10:58:59	55512.96	25	4.1	480	1.38
2010 Nov 14 10:37:51	55514.94	27	4.1	240	1.45
2010 Nov 14 10:48:28	55514.95	27	4.1	240	1.40
2010 Nov 14 10:59:10	55514.96	27	4.1	240	1.35
2010 Nov 15 10:24:18	55515.93	28	4.1	480	1.50
Epoch 2, Day 45, 61” Kuiper					
2010 Dec 1 10:46:25	55531.95	44	4.1	720	1.18
2010 Dec 2 10:30:14	55532.94	45	4.1	720	1.21
2010 Dec 3 10:26:37	55533.93	46	4.1	800	1.21
Epoch 3, Day 77, 90” Bok					
2011 Jan 2 09:40:30	55563.90	76	4.1	480	1.10
2011 Jan 3 09:18:10	55564.89	77	4.1	480	1.12
2011 Jan 3 09:37:35	55564.90	77	4.1	480	1.10
Epoch 4, Day 109, 90” Bok					
2011 Feb 2 08:17:48	55594.84	107	4.1	720	1.08
2011 Feb 5 07:46:36	55597.82	110	4.1	720	1.09
2011 Feb 6 08:00:15	55598.83	111	4.1	720	1.08
Epoch 5, Day 137, 90” Bok					
2011 Mar 2 07:31:31	55622.81	135	4.1	720	1.12
2011 Mar 4 06:24:15	55624.77	137	4.1	720	1.08
2011 Mar 6 06:38:36	55626.78	139	4.1	720	1.09

Table reproduced with permission from Williams et al. (*in prep.*)

[a] Phases represent days after V-band maximum light (Stoll et al. 2011; Zhang et al. 2012, MJD = 55488;).

[b] Listed times represent the duration of a full Q or U sequence at all waveplate positions. The total exposure time is twice this value.

[c] Several nights' observations from a single telescope are combined into an “epoch”. Each epoch's nominal “Day” designation is the average of “Days Post-max” for all the component observations.

and with that of SN 1997eg. For the three epochs of SN 2010jl examined in this work, the emission line ratio is 7.12 ± 0.07, 8.52 ± 0.08, and 9.75 ± 0.10, respectively.

Due to the uncertain date of maximum light of SN 1997eg, the first 3 observational epochs of these two SNe may not be directly comparable. Adding $30 - 60$ days (Hoffman et al. 2008) to the post-discovery dates of the SN 1997eg observations puts their post-maximum times at 46–76 days (Epoch 1), $74 - 104$ days (Epoch 2), and $123 - 153$ days (Epoch 3). Thus they are likely most directly comparable with observational Epochs $3 - 5$ of SN 2010jl. Throughout this chapter, the epoch number denotes the sequential order of fits using those observations made when the age of SN 2010jl is closest to those of SN 1997eg.

4.3 Model fitting

SN 2010jl Hα flux emission ratios are very similar to those of SN 1997eg in the first two comparison epochs (§ 3.4). The line profiles in SN 2010jl are slightly smoother than in SN 1997eg, such that different line width components are not as readily distinguishable by eye; the intermediate-width component is less prominent then the one characterizing SN 1997eg at the epochs I investigated in Chapter 3. The depolarization across the line core is the most prominent feature of the SN 2010jl polarization spectra, which otherwise remain roughly constant across the fitted wavelength range. The exception occurs in Epoch 3, in which the continuum is less polarized toward the red end than the blue end and the core depolarization is less pronounced. SN 2010jl possesses no regions of enhanced polarization in the Hα region like those seen in SN 1997eg.

In the next section I discuss *SLIP* model fits to the selected epochs of SN 2010jl. The models are identical to those discussed in Chapters 2 and 3. This fact becomes particularly important in the case of the distributed-source models, which use the flux spectrum of Epoch 1 of SN 1997eg as the spectrum emitted from the shock

region. Figure 4.2 illustrates the flux and polarization spectra of both events across the three epochs. The Hα lines at Epochs 1 and 2 compare quite well in width and strength to those of SN 1997eg, making the choice of input spectrum for the distributed models a low concern at these epochs. However, there is a discernible difference between the two in the third comparison epoch, in which the Hα line of SN 1997eg is significantly stronger relative to the continuum and broader then that of SN 2010jl. This discrepancy is likely to cause more uncertainty in the emission ratio diagnostic in Epoch 3; an input spectrum that is wider and stronger than the observed spectra I attempt to fit may result in output emission line ratios that are too large, as a greater number of photons are emitted from the central line region. Use of a single input spectrum for the distributed case is a necessary assumption, however, to avoid having to run a completely new distributed grid for every supernova at every epoch.

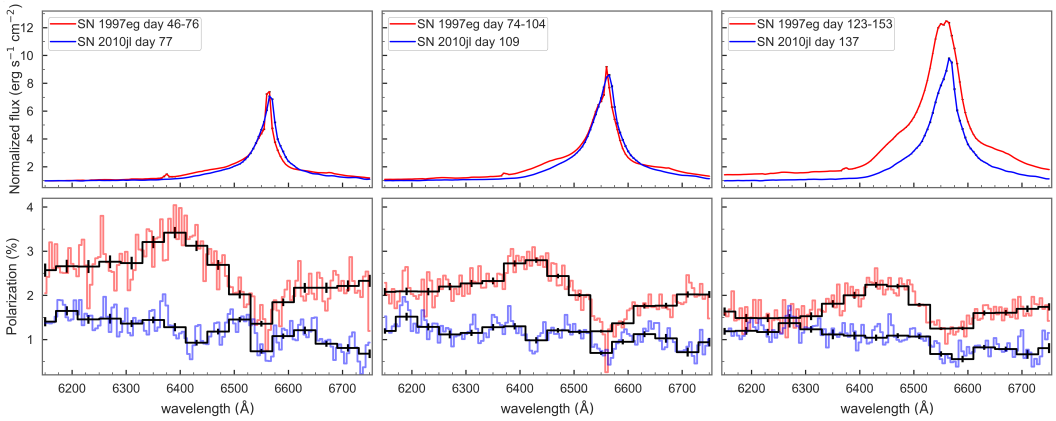

Figure 4.2: Observed flux (top) and polarization(bottom) data of the Hα line for both SNe at all three comparison epochs. Time increases from left to right with SN 1997eg (red) at days 46–76, 74–104, and 123–153, and SN 2010jl at days 77, 109, and 137 post-discovery. (§ 4.1). Fluxes (top) are normalized to the continuum at 6130 Å. Percent polarization (bottom) is shown at 5 Å in red, over-plotted by the 40-Å re-binned spectrum in black.

Overall trends in the relationships between the model fit parameters and the χ^2_ν for SN 2010jl are analogous to those seen in SN 1997eg (§ 3.4). For any given set of models with otherwise constant parameter values, increasing temperature produces

stronger emission lines in the flux spectrum and thus a greater emission ratio, while increasing viewing angle results in models requiring a larger negative polarization shift due to higher continuum polarization. For SN 2010jl as well as SN 1997eg, I find a well-constrained bimodal distribution of models that hinges on the value of $L_{\rm Sh}$. This produces two distinct populations: models with higher $L_{\rm Sh}$ produce much more flux in the Hα line than do those with the lower value, as illustrated in Fig. 4.3.

4.4 Central-source model fits

4.4.1 Epoch 1

Table 4.2: Central Models with Best-Fitting Polarization, Epoch 1 of SN 2010jl

Parameters	Models							
Geometry	disk	disk	disk	disk	disk	disk	disk	disk
Optical Depth	1.0	2.0	2.0	2.0	2.0	2.0	1.0	2.0
$L_{\rm CSM}/L_{\rm SN}$	0.0	0.0	0.1	0.1	0.0	0.1	0.1	0.0
$L_{\rm Sh}/L_{\rm SN}$	0.01	0.01	0.2	0.2	0.2	0.2	0.2	0.2
Temp. (10^3 K)	10	20	20	20	20	20	10	20
Inclination (°)	82	82	67	59	67	74	74	59
ρ (10^{-12} g cm^{-3})	4.79	9.55	9.55	9.55	9.55	9.55	4.79	9.55
$n_{\rm e}$ (10^{12} cm^{-3})	2.83	5.65	5.65	5.65	5.65	5.65	2.83	5.65
Emission Ratio	3.23	3.61	22.9	24.9	24.1	22.8	20.0	26.5
Pol. Shift (%)	-2.77	-3.51	-1.27	-1.21	-1.24	-1.32	-0.96	-1.12
χ^2_ν	5.70	5.76	7.40	7.47	7.68	7.68	7.73	7.78
A^2	0.49	0.69	0.84	0.63	0.71	0.94	0.62	0.56

I list the properties of the 8 best-fitting central-source models for Epoch 1 in Table 4.2 display the spectra of the first four in Fig. 4.4. These models are generally characterized by lower optical depths of 0.5 and 1.0 and inclinations of between 59° and 82°. All three temperatures are present among this group. However, those with the very lowest χ^2_ν values of $2.55 - 2.59$ all have temperatures of 10,000 K. As

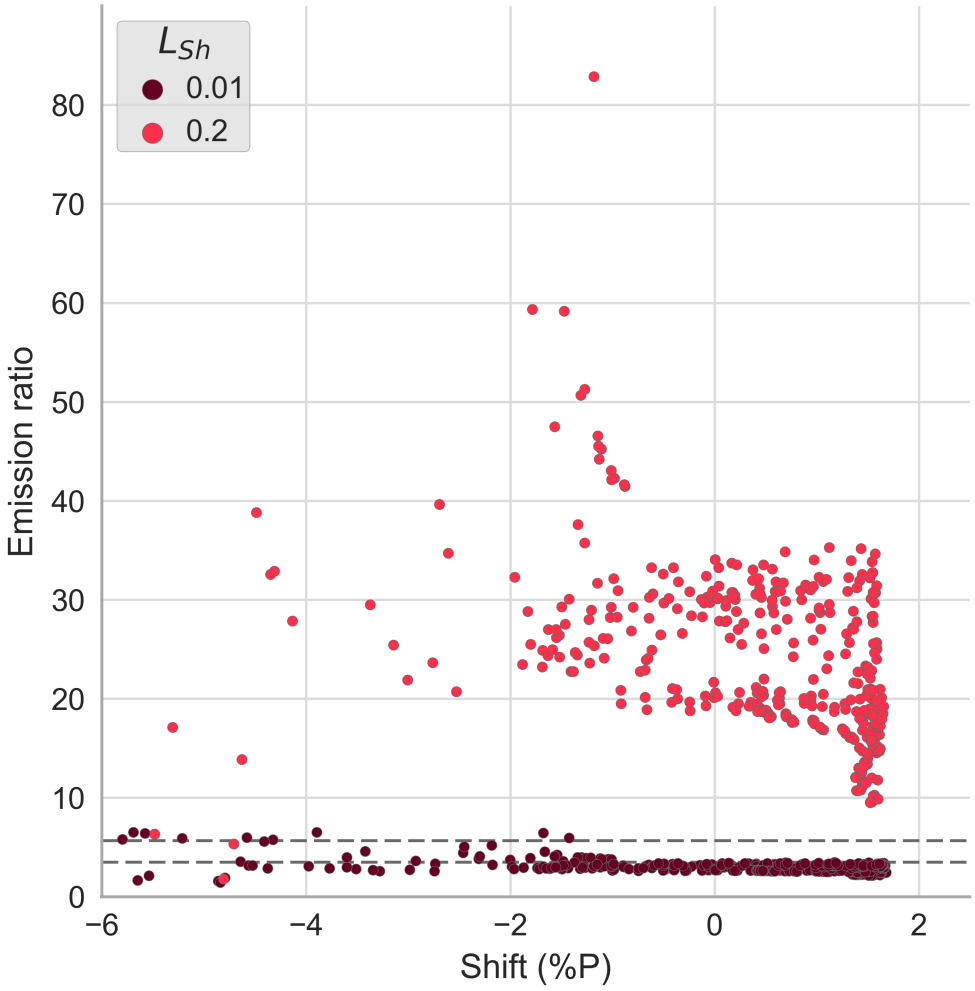

Figure 4.3: The value of the shock luminosity greatly influences the height of the flux emission line, creating two distinct central-source model populations when plotted in polarization shift-emission ratio space. The horizontal dashed grey lines indicate the region of the observed emission ratio for the first epoch of SN 2010jl.

for SN 1997eg, the toroid models among these 8 are restricted to the lower shock luminosity, $L_{\rm Sh} = 0.01$, while the disks have the higher value of $L_{\rm Sh} = 0.2$. Another similarity between the fits for the two SNe is that the value for CSM luminosity $L_{\rm CSM}$ does not appear to be an influential factor in polarization fitting.

I identified 19 models as belonging to a best-fitting cluster with χ^2_ν less then 8.8, all of which are disk models. These models have an average polarization shift of

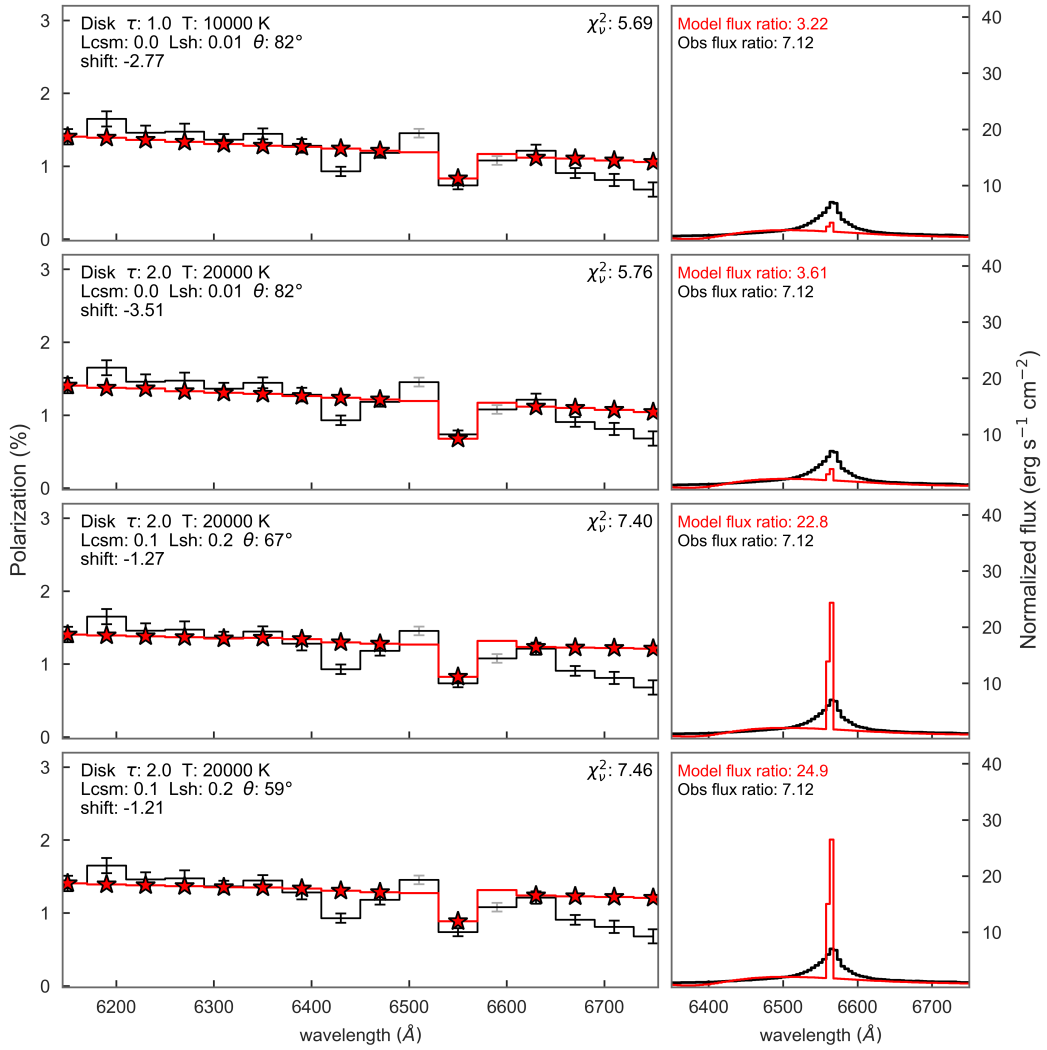

Figure 4.4: Polarization (left) and flux (right) spectra of the four models (red) in the central-source grid that best fit the first comparison epoch of SN 2010jl. The observed spectra of SN 2010jl at Epoch 1 are shown in black. Wavelength points included in the fit are marked by red stars.

$-1.39 \pm 0.19\%$. There are striking similarities between the trends in this cluster and those I identified in the low clusters for all three epochs of SN 1997eg. The cluster can be subdivided into subsets differentiated by high and low shock luminosities and resulting high and low emission ratios, mirroring the behavior of the entire model distribution, see Figure 4.5. The high shock luminosity subgroup is significantly

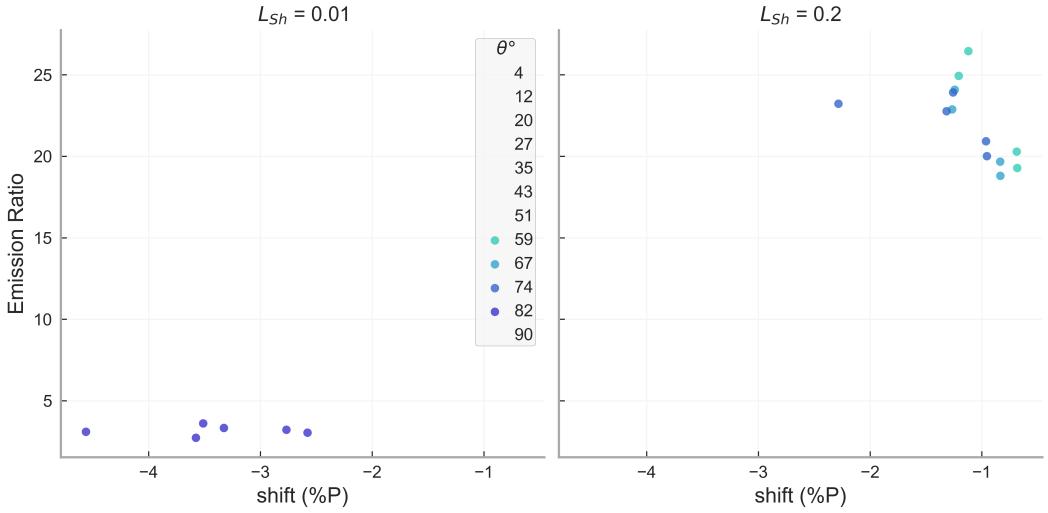

Figure 4.5: Polarization shift vs. emission ratio of models in the low χ^2_ν cluster, separated shock luminosity (columns) and colored according to inclination angle. The low χ^2_ν cluster is comprised only of disk models. Those of low shock luminosity (left) are constrained to inclination of 82°, while those of high shock luminosity (right) range between 59° and 74°.

larger. The low shock luminosity group is restricted to inclinations of 82°; these models are consistent in their emission ratios, which are lower then that of the observed spectrum, but produce much higher and more widely dispersed levels of continuum polarization then those with low shock luminosity, between about $2.5 - 4.5\%$. The high shock luminosity group has a slightly wider range of inclinations, from $59° - 74°$ and varies less in the total amount of polarization shift required $(0.5 - 1.5\%)$, but a larger range of emission ratios between around 18 to almost 30.

4.4.2 Epoch 2

I list the properties of the best-fitting central models for comparison epoch 2 in Table 4.3 and display the spectra of the first four in Fig. 4.6. These models are all disks characterized by optical depths of 1.0 or 2.0. The two with low shock luminosity are both inclined at 82° and produce flux emission ratios lower than observed. Those with higher shock luminosity are inclined between 59° and 74° with emission ratios of $20 - 25$. Models with an optical depth of 2.0 all have temperatures of

Table 4.3: Central Models with Best-Fitting Polarization, Epoch 2 of SN 2010jl

Parameters	Models							
Geometry	disk	disk	disk	disk	disk	disk	disk	disk
Optical Depth	1.0	2.0	2.0	2.0	2.0	1.0	1.0	2.0
$L_{\rm CSM}/L_{\rm SN}$	0.0	0.1	0.1	0.0	0.0	0.1	0.0	0.0
$L_{\rm Sh}/L_{\rm SN}$	0.01	0.2	0.2	0.2	0.01	0.2	0.2	0.2
Temp. (10^3 K)	10	20	20	20	20	10	10	20
Inclination (°)	82	67	59	67	82	74	74	74
ρ (10^{-12} g cm^{-3})	4.79	9.55	9.55	9.55	9.55	4.79	4.79	9.55
$n_{\rm e}$ (10^{12} cm^{-3})	2.83	5.65	5.65	5.65	5.65	2.83	2.83	5.65
Emission Ratio	3.23	22.9	24.9	24.1	3.61	20.0	20.9	23.9
Pol. Shift (%)	-2.45	-0.94	-0.88	-0.91	-3.19	-0.62	-0.63	-0.92
χ^2_ν	3.02	3.21	3.27	3.28	3.36	3.36	3.42	3.43
A^2	0.26	0.21	0.24	0.19	0.30	0.24	0.24	0.17

20,000 K, while those with optical depth 1.0 have a temperature of 10,000 K. Temperature in *SLIP* primarily controls the ionization fraction. Maintaining constant temperature while increasing optical depth necessitates an increase in the number of hydrogen nuclei, effectively increasing the density by proxy. For a constant optical depth, lower temperatures reduce the ionization fraction making more neutral atoms available to absorb line photons. The denser gas permits a greater level of line photon transmission when a larger fraction of the atoms are ionized at a higher temperature. Both of these effects alter the ratio of escaping line photons relative to the amount that are polarized and make the depolarization shallower. Depolarization levels of the line core are quite similar for both cases when the denser CSM is slightly less inclined.

I identified 24 models belonging to a best-fitting cluster with χ^2_ν less then 4.2. These models have an average polarization shift of $-1.35\% \pm 0.19\%$. Trends among the shock luminosity, polarization shift, and emission ratios of models within the cluster are similar to those found in Epoch 1. Most models in the cluster have optical depths of 1.0 or 2.0 and are disks, but there is no identifiable correlation

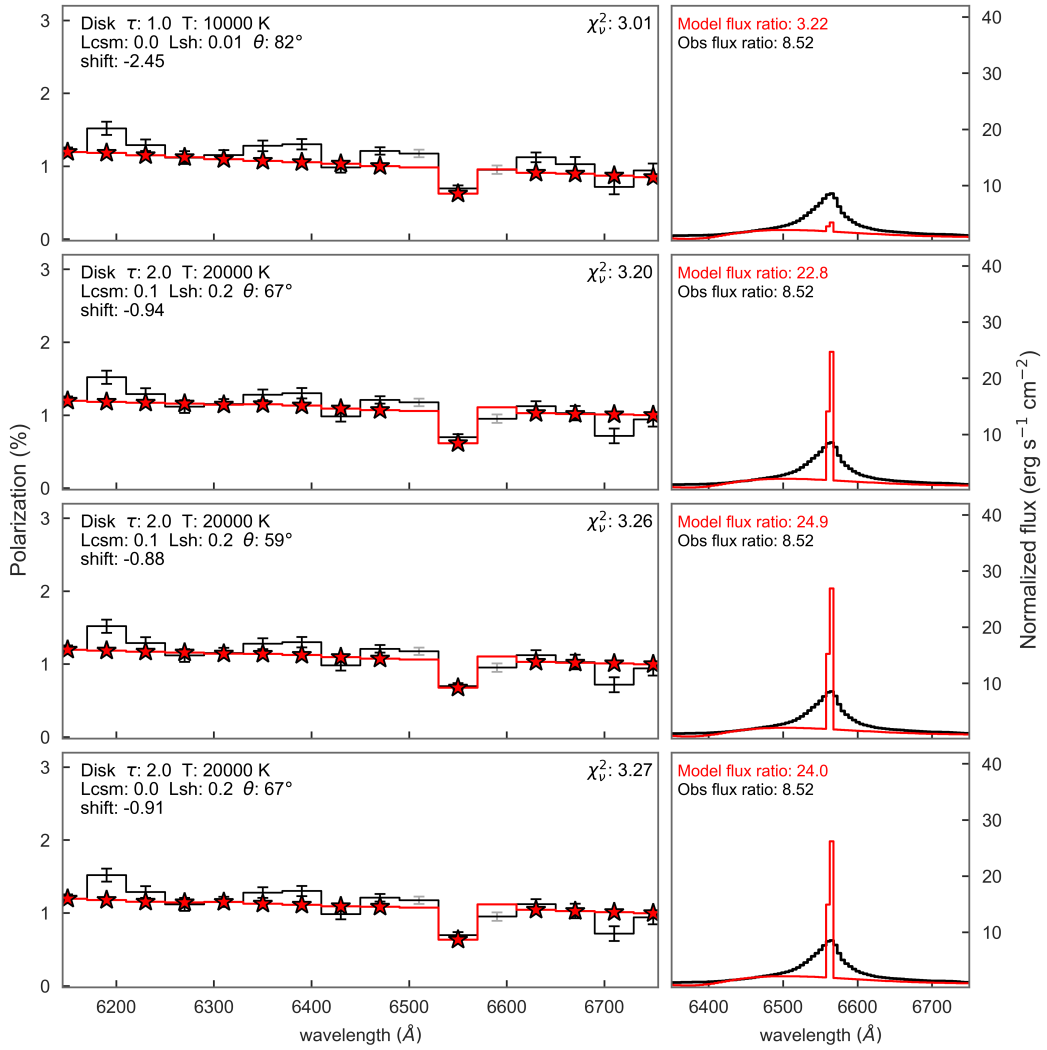

Figure 4.6: Polarization (left) and flux (right) spectra of the four models (red) in the central-source grid that best fit the second comparison epoch of SN 2010jl. The observed spectra of SN 2010jl at Epoch 2 are shown in black. Wavelength points included in the fit are marked by red stars.

between these values with any specific pattern of temperatures, inclinations, or the luminosities of the shock and CSM. Only two models have a temperature of 50,000 K; both have an optical depth of 2.0, but nothing else in common. A result of note is that there are no models in the best-fitting cluster with an edge-on inclination of 90°.

Table 4.4: Central Models with Best-Fitting Polarization, Epoch 3 of SN 2010jl

Parameters	Models							
Geometry	disk	disk	disk	disk	disk	disk	disk	disk
Optical Depth	1.0	2.0	2.0	1.0	2.0	1.0	1.0	1.0
$L_{\rm CSM}/L_{\rm SN}$	0.0	0.0	0.1	0.1	0.1	0.1	0.1	0.0
$L_{\rm Sh}/L_{\rm SN}$	0.01	0.01	0.01	0.01	0.2	0.2	0.2	0.2
Temp. (10^3 K)	10	20	20	10	20	10	10	10
Inclination (°)	82	82	82	82	59	67	59	67
ρ (10^{-12} g cm^{-3})	4.79	9.55	9.55	4.79	9.55	4.79	4.79	4.79
$n_{\rm e}$ (10^{12} cm^{-3})	2.83	5.65	5.65	2.83	5.65	2.83	2.83	2.83
Emission Ratio	3.23	3.61	3.33	3.04	24.9	18.8	19.3	19.7
Pol. Shift (%)	-2.88	-3.64	-3.45	-2.70	-1.32	-0.95	-0.80	-0.95
χ^2_ν	1.96	2.70	2.77	2.78	3.48	3.54	3.58	3.63
A^2	0.36	0.39	0.21	0.23	0.64	0.60	0.50	0.63

4.4.3 Epoch 3

The properties of the best-fitting central models for comparison Epoch 3 are listed in Table 4.4 and display the spectra of the first four in Fig. 4.7. Again, these models are all disks characterized by optical depths of 1.0 or 2.0 and all the parameter trends from Epoch 2 are identically present. Those with low shock luminosity are all inclined at 82° and produce flux emission ratios lower than observed, while those with higher shock luminosity are all inclined between 59° and 67° with emission ratios of $18-25$. Models with an optical depth of 2.0 all have temperatures of 20,000 K, while those with optical depth 1.0 have a temperature of 10,000 K.

15 models are identified as belonging to a best-fitting cluster with χ^2_ν less than 3.9. These models have an average polarization shift of $-1.82\% \pm 0.28\%$. Trends among the shock luminosity, polarization shift, and emission ratios of models within the cluster are the same as those found in both Epochs 1 and 2. Most models in the cluster have optical depths of 1.0 or 2.0 and all are disks, but there is no identifiable correlation between these parameters with any specific pattern of temperatures, inclinations, or the luminosities of the shock and CSM. There are no models with a

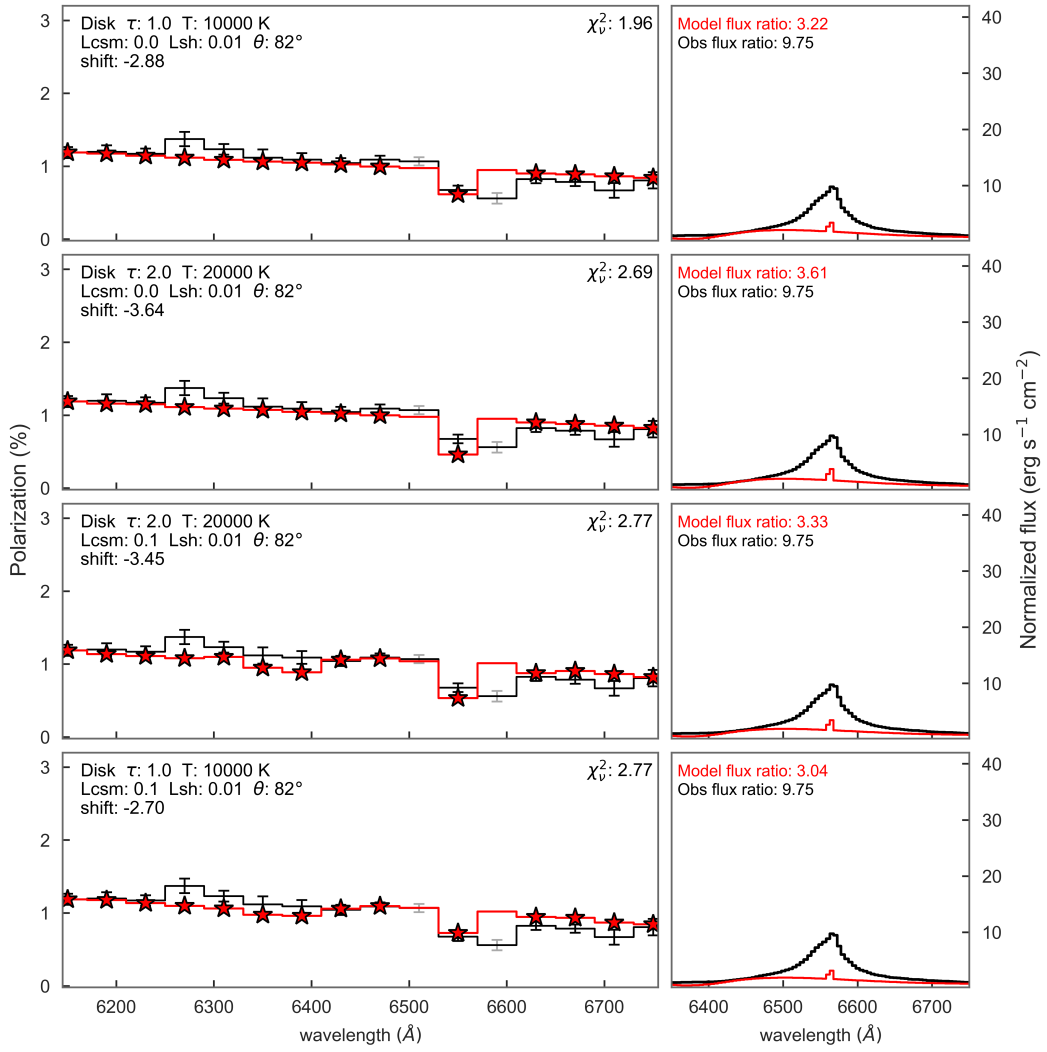

Figure 4.7: Polarization (left) and flux (right) spectra of the four models (red) in the central-source grid that best fit the second comparison epoch of SN 2010jl. The observed spectra of SN 2010jl at Epoch 3 are shown in black. Wavelength points included in the fit are marked by red stars.

temperature of 50,000 K, all are equally split between 10,000 K and 20,000 K. The cluster is also relatively evenly subdivided into groups of high and low shock luminosities that have high and low emission ratio. The low shock luminosity group is restricted to inclinations of 82°; these models are consistent in having emission ratios lower then that of the observed spectrum, and higher polarization shifts then those

with low shock luminosity, between about $2.5 - 3.5\%$. The high shock luminosity group has the same familiar range of inclinations as in Epochs 1 and 2, from $59° - 74°$ and varies less in the total amount of polarization shift required ($0.75 - 1.4\%$), but again has a larger range of emission ratios between around 18 to 26.

4.5 Distributed-source model fits

The distributed-source models discussed in the next three sections form a different set of patterns within the χ^2_ν, emission ratio, and polarization shift space than do the central-source models. All distributed-source models emit the same source spectrum from their shock regions with the same luminosity. The most notable consequence of this is the lack of bimodal subpopulations based on shock luminosity. Equalization of this parameter constrains all models to occupy a similar region in emission ratio space around that of the observed values, between 4 and 13 times the continuum level. As for the central-source models, increasing inclination angle creates larger levels of continuum polarization that necessitate greater negative polarization shifts to match the observed polarized continuum. The spread in continuum polarization is larger for disks than for toroids. Toroids are localized to the polarization shift region between 1.0% and -2.0%, whereas some highly inclined disks have polarization levels as high as 6% greater than observed.

Distributed models do an excellent job of reproducing the gradual linear decrease in polarization from blue to red across the spectrum of SN 2010jl, particularly in Epoch 3. They have difficulty matching the correct amount of depolarization across the line, just line in SN 1997eg, that is seen in all three epochs. A single model with χ^2_ν below the critical value is identified for Epoch 3. However, this fit is driven by the points the in wider regions of the line and not at the line core itself. Development of the physics in distributed models is a work in progress, which I discuss further in Chapter 5.

Table 4.5: Distributed Models with Best-Fitting Polarization, Epoch 1 of SN 2010jl

Parameters	Models							
Geometry	disk	disk	disk	disk	disk	tor.	disk	disk
Optical Depth	2.0	2.0	2.0	2.0	2.0	2.0	1.0	1.0
$L_{\rm CSM}/L_{\rm SN}$	0.0	0.0	0.1	0.1	0.0	0.0	0.0	0.0
$L_{\rm Sh}/L_{\rm SN}$	1.0	1.0	1.0	1.0	1.0	1.0	1.0	1.0
Temp. (10^3 K)	20	20	20	20	20	50	10	10
Inclination (°)	82	90	82	74	74	90	90	82
ρ (10^{-12} g cm^{-3})	9.55	9.55	9.55	9.55	9.55	70.9	4.79	4.79
$n_{\rm e}$ (10^{12} cm^{-3})	5.65	5.65	5.65	5.65	5.65	39.8	2.83	2.83
Emission Ratio	7.80	5.88	7.02	7.44	7.99	12.2	5.53	7.44
Pol. Shift (%)	-2.56	-8.55	-2.23	-1.63	-1.64	-1.67	-4.28	-1.48
χ^2_ν	4.98	5.43	5.63	6.36	7.14	7.15	7.47	7.76
A^2	0.46	0.39	0.60	0.61	0.50	0.66	0.46	0.48

4.5.1 Epoch 1

The parameters of the 8 best-fitting distributed models are listed in Table 4.5, and are predominantly disks with high optical depth of 2.0. There is a single toroid, also with optical depth of 2.0, and a disk with optical depth of 1.0. All are constrained to high inclination between 74° and 90°. This entire group is also rather consistent with the amount of polarization shift, between −1.5% and −2.5%, with two notable exceptions. The two disks inclined at 90° produce extremely high levels of polarization; −8.5% for the one with optical depth of 2.0, and −4.3% for the disk with optical depth of 1.0. In section 3.6 I discuss the potential roles that density and axisymmetry play in the polarization fits. These models indicate that axisymmetry is contributing a considerable role. The disks are less dense then the toroids, but among these 8 models, models with disk CSM inclined at 90° create spectra with far higher levels of polarization then the toroid at the same inclination.

The spectra for the best-fitting 4 are shown in Figure 4.8. There is a characteristic linear decline in polarization from the blue to the red end of the spectrum, with the narrowest region of the line not being depolarized strongly in compari-

son. Rather, there is a slight bit of polarization enhancement in the intermediate width regions. The models that fit best in this Epoch are those that reproduce the continuum and narrow line, but do not create an increase in polarization in the intermediate width. I identified 15 models belonging to a best-fitting cluster with χ^2_ν less than 8.7. These models have an average polarization shift of $-2.71 \pm 0.32\%$. The trends of these models do not differ significantly from the descriptions of the lowest 8.

4.5.2 Epoch 2

The parameters of the 8 best-fitting models for Epoch2 of SN 2010 jl are listed in Table 4.6, the spectra of the 4 with the lowest χ^2_ν values are shown in 4.9. The best-fitting model for Epoch 2, with a wide margin, is a toroid inclined at 90° with high optical depth of 2.0 and high temperature of 50,000 K. Interestingly, this is the only toroid model among these lowest 8 and in the entire cluster, and the same individual distributed toroid model belonging to the low χ^2_ν cluster in Epoch 1. The density of this toroid is much greater then that of disks with the same value, 7.1×10^{-11} g cm^{-3}, almost 2 orders of magnitude higher then a disk of comparable parameters.

Just like in Epoch 1, all models in the low 8 have optical depths of 2.0 and high temperatures, and are inclined between 74° and 90°. 34 models are identified as belonging to a best-fitting cluster with χ^2_ν less than 7.9. These models have an average polarization shift of $-2.82 \pm 0.19\%$. The parameter trends of this low cluster are identical to those of Epoch 1.

4.5.3 Epoch 3

The fits of distributed-source models in this epoch are unique in that they comprise the only data set in the entire work to produce a model with a statistically

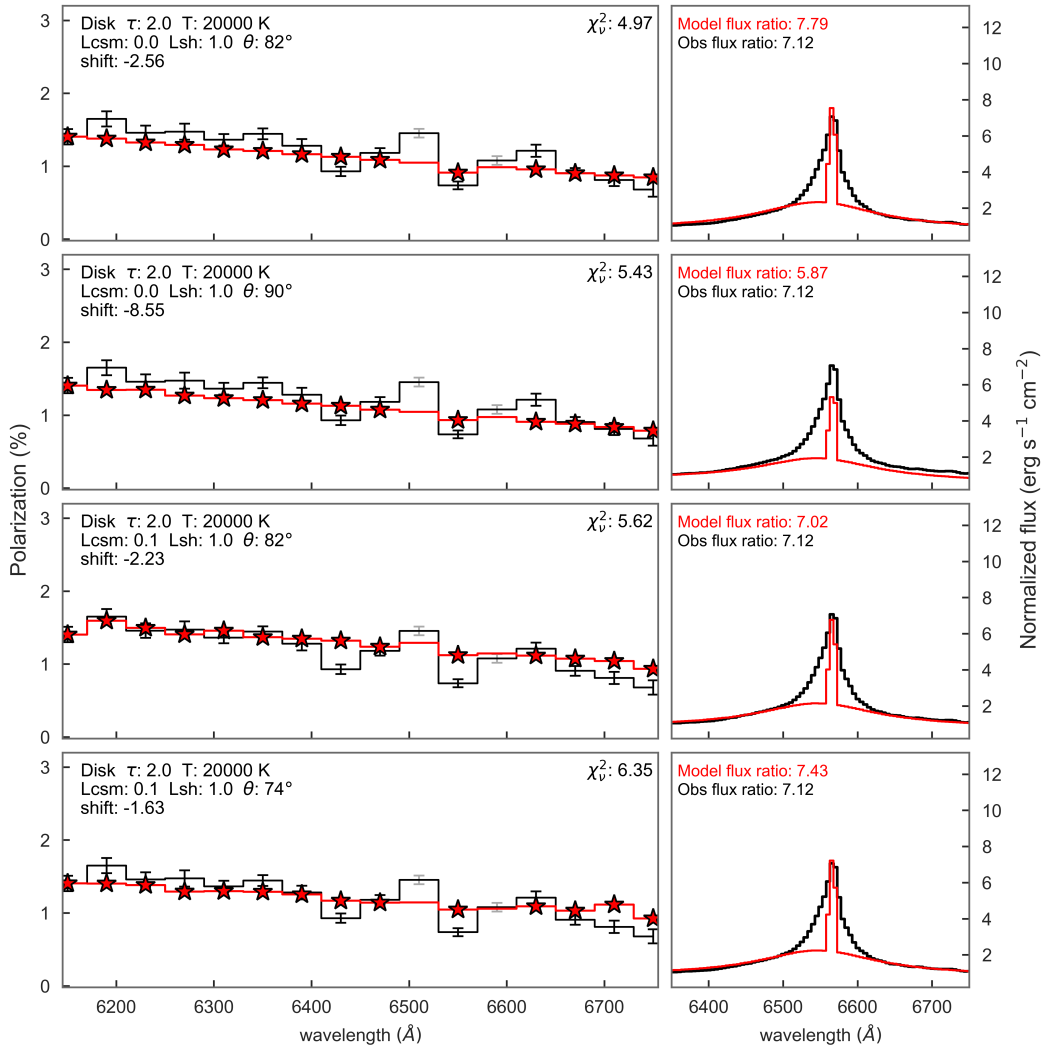

Figure 4.8: Polarization (left) and flux (right) spectra of the four models (red) in the distributed-source grid that best fit the first comparison epoch of SN 2010jl. The observed spectra of SN 2010jl at Epoch 1 are shown in black. Wavelength points included in the fit are marked by red stars.

significant fit below the critical χ^2_ν value of 1.88. This model is a disk with optical depth of 2.0, no CSM luminosity, inclination of 82°. The parameters for the 8 models with the lowest χ^2_ν values are shown in Table 4.7, and the spectra of the best-fitting 4 are plotted in Figure 4.10.

Table 4.6: Distributed Models with Best-Fitting Polarization, Epoch 2 of SN 2010jl

Parameters	Models							
Geometry	tor.	disk	disk	disk	disk	disk	disk	disk
Optical Depth	2.0	2.0	2.0	2.0	2.0	2.0	2.0	1.0
$L_{\rm CSM}/L_{\rm SN}$	0.0	0.0	0.1	0.0	0.1	0.0	0.1	0.0
$L_{\rm Sh}/L_{\rm SN}$	1.0	1.0	1.0	1.0	1.0	1.0	1.0	1.0
Temp. (10^3 K)	50	50	50	20	50	50	20	20
Inclination ($^\circ$)	90	82	74	82	82	74	82	82
ρ (10^{-12} g cm^{-3})	70.9	9.55	9.55	9.55	9.55	9.55	9.55	4.79
$n_{\rm e}$ (10^{12} cm^{-3})	39.8	5.65	5.65	5.65	5.65	5.65	5.65	2.84
Emission Ratio	12.2	7.79	7.27	7.80	6.85	8.00	7.02	7.48
Pol. Shift (%)	-1.34	-4.72	-3.23	-2.26	-4.64	-3.21	-1.93	-3.41
χ^2_ν	2.79	4.59	5.32	5.70	5.94	5.99	6.20	6.27
A^2	0.30	0.21	0.23	0.33	0.31	0.25	0.38	0.45

Table 4.7: Distributed Models with Best-Fitting Polarization, Epoch 3 of SN 2010jl

Parameters	Models							
Geometry	disk	disk	disk	disk	disk	disk	disk	disk
Optical Depth	2.0	2.0	2.0	2.0	1.0	1.0	1.0	2.0
$L_{\rm CSM}/L_{\rm SN}$	0.0	0.0	0.1	0.0	0.0	0.0	0.1	0.0
$L_{\rm Sh}/L_{\rm SN}$	1.0	1.0	1.0	1.0	1.0	1.0	1.0	1.0
Temp. (10^3 K)	20	20	20	20	10	10	10	20
Inclination ($^\circ$)	82	90	82	74	90	82	82	67
ρ (10^{-12} g cm^{-3})	9.55	9.55	9.55	9.55	4.79	4.79	4.79	9.55
$n_{\rm e}$ (10^{12} cm^{-3})	5.65	5.65	5.65	5.65	2.83	2.83	2.83	5.65
Emission Ratio	7.80	5.88	7.02	7.99	5.53	7.44	6.83	7.94
Pol. Shift (%)	-2.67	-8.66	-2.34	-1.75	-4.38	-1.58	-1.55	-1.72
χ^2_ν	1.63	1.92	2.14	2.42	2.57	2.80	2.86	2.87
A^2	0.19	0.22	0.21	0.38	0.54	0.35	0.46	0.34

I identified 40 models belonging to a best-fitting cluster with χ^2_ν less then 5.5. These models have an average polarization shift of $-2.71 \pm 0.5\%$. Unlike Epochs 1 and 2, the distributed fits do not contain any toroidal models in the low χ^2_ν cluster. The fits in this epoch are again, entirely driven by the overall continuum polarization and the lack of strong depolarization across the narrow line in the observed spectrum. All the models in this cluster are disks with optical depths of 1.0 and 2.0. There

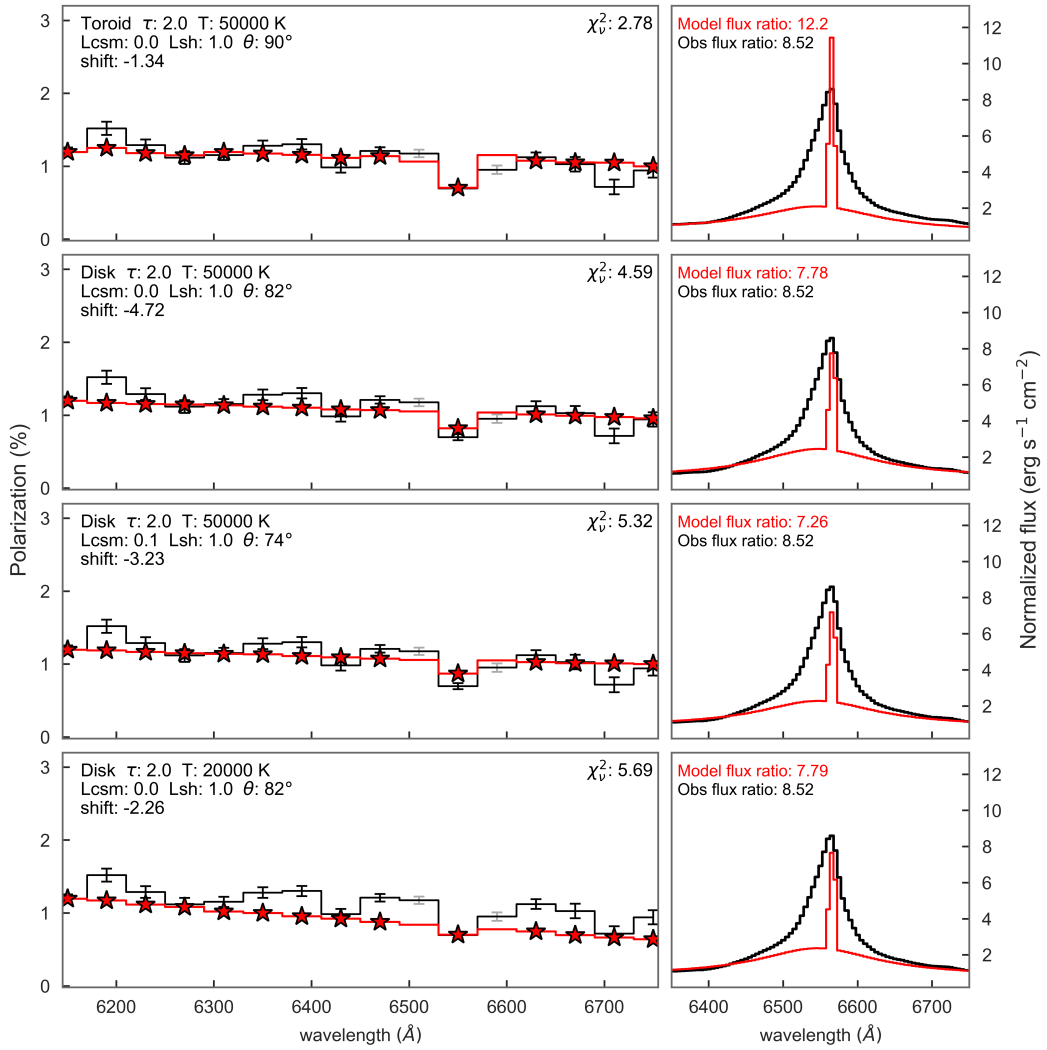

Figure 4.9: Polarization (left) and flux (right) spectra of the four models (red) in the distributed-source grid that best fit the second comparison epoch of SN 2010jl. The observed spectra of SN 2010jl at Epoch 2 are shown in black. Wavelength points included in the fit are marked by red stars.

does not appear to be any preference for the CSM luminosity. There is a wider range of inclinations then among any other epoch or regime of fits for SN 2010jl. Most models are between 59° and 90°, but there are 2 out of the 40 inclined to 51° and a single model inclined to 43°.

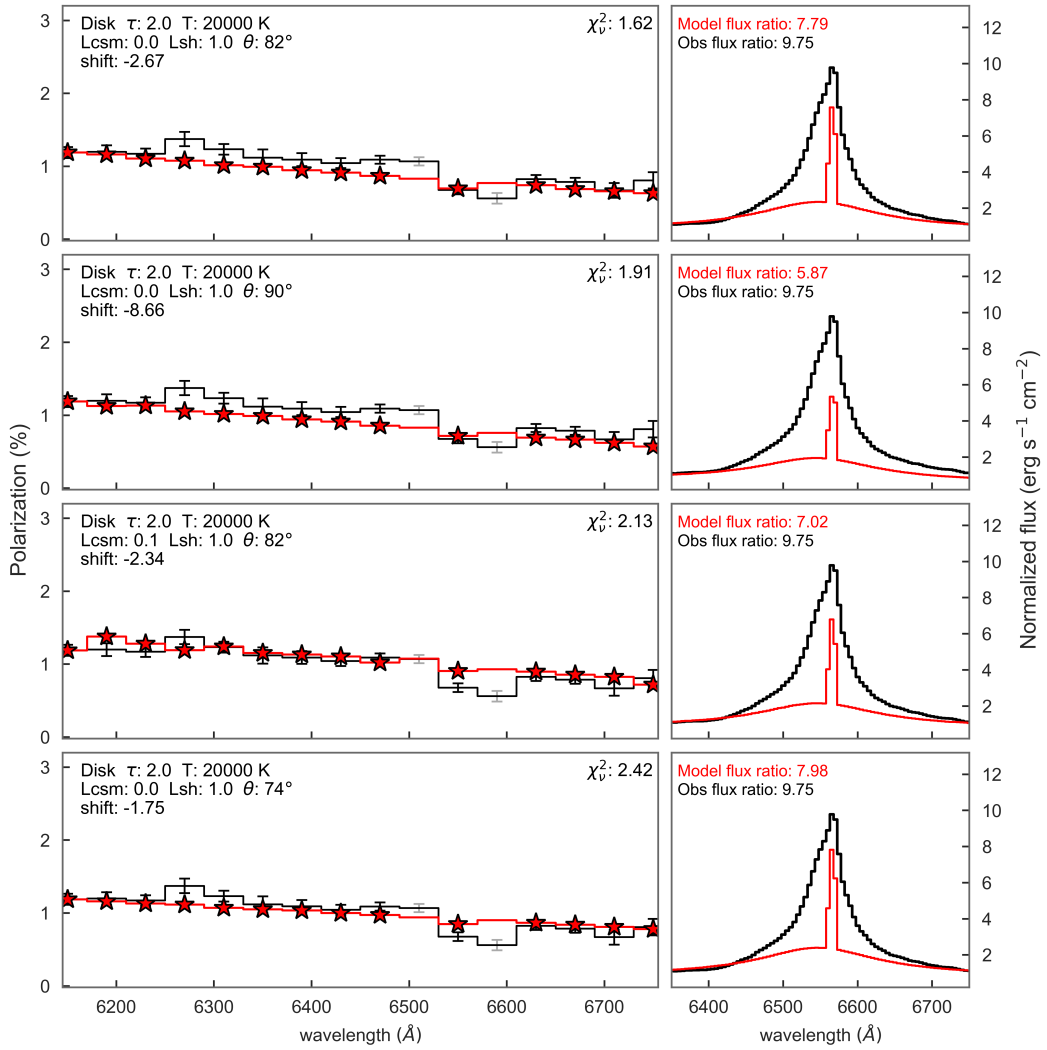

Figure 4.10: Polarization (left) and flux (right) spectra of the four models (red) in the distributed-source grid that best fit the thirdscomparison epoch of SN 2010jl. The observed spectra of SN 2010jl at Epoch 3 are shown in black. Wavelength points included in the fit are marked by red stars.

4.6 Discussion

Distributed source models in the low cluster were shifted by an average of $-2.753 \pm 0.464\%$. All best-fitting distributed models and models in the lowest χ^2_ν cluster that have Gaussian residuals are disks. A single toroid model, with high temperature, optical depth, and inclination has an A^2 value above the critical level

of 0.68. It does not capture the linear drop of polarization across the spectrum, skewing the residuals to higher values on the red end of the line. All the distributed models producing fits to the polarization with the very lowest χ^2_ν values have flux emission ratios below that of observation. Despite fitting very well in polarization, none of these models have an emission line height with enough excess area to feasibly fill in the intermediate width regions of the line under the effect of Doppler shifts from velocity.

There are two subpopulations of central models within the low χ^2_ν group, characterized by different values for emission ratio and polarization shift. One with high shock luminosity has higher emission ratios and lower polarization shifts with less dispersion and the other, characterized by low shock luminosity, contains models which all have emission ratios below that of the observed ratio and require a larger reduction over a wider range in polarization. The lower $L_{\rm Sh}$ emission ratio group contains models of higher inclination constrained at an angle of 82°, while the higher $L_{\rm Sh}$ emission ratio group span between 51° and 74°. These models are disks, with only 2 toroids out of the 24 models present in the low cluster for epoch 2.

The same central model, a disk with low shock and CSM luminosity, low temperature, and inclination of 82°, has the lowest χ^2_ν for all three epochs of SN 2010jl, but is not a model of interest considered in Chapter 5. As a model with low $L_{\rm Sh}$, it does not meet the emission line area criteria. Central-source models in the low cluster were shifted by an average of $-1.662\% \pm 0.463$ over all three epochs. This is considerably higher then the observational estimate of 0.5% discussed in § 4.1. The average shift changes when taken from the two different $L_{\rm Sh}$ subpopulations described above, to $-3.319 \pm 0.463\%$ and $-0.975 \pm 0.463\%$, for low and high values respectively. This places the higher $L_{\rm sh}$ group much closer to observational estimate. Indeed, the high shock luminosity group contains the only models meeting the emis-

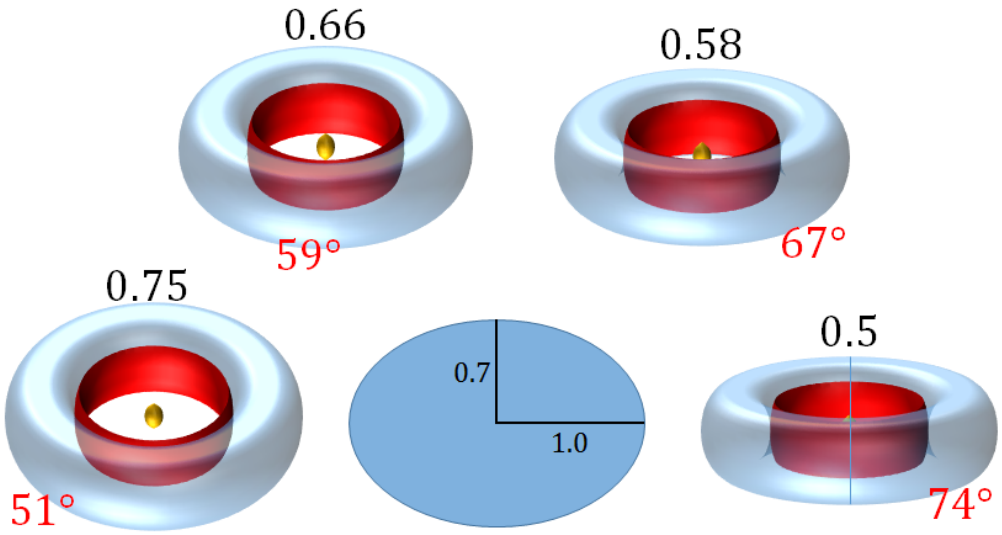

Figure 4.11: An oblate spheroid of axial ratio 0.7 (*center*), proposed by Patat et al. (2011) as a likely geometrical distribution of the CSM in SN 2010jl based on models of their polarimetric data from Day 15 post-maximum (Höflich 1991), is surrounded by cartoon visualizations of *SLIP* disk geometries at the range of inclinations found within the low χ^2_ν clusters at each epoch.

sion line area criteria. The parameters for models of interest used to determine CSM wind characteristics and ISP estimates are contained in Table 5.2

An interesting result for SN 2010jl stems from the polarimetry modeling done by Patat et al. (2011) using models from Höflich (1991). This work predicted an axial ratio of asymmetry of less than or equal to 0.7. Two correctly scaled mock-ups of the disk CSM geometry, tilted at the most common inclination values among the low χ^2_ν cluster models, between 51° and 74°, are illustrated in Figure 4.11. These representative cartoons of the disk CSM are plotted around an ellipsoid of axial ratio 0.7 for comparison. These models are a visual match to the level of axial flattening predicted. The selection of models with high inclination as the best fits is confirmation that the CSM surrounding SN 2010jl is indeed highly asymmetric.

Chapter 5

Conclusions

5.1 Results

In this chapter, I analyze the best-fitting groups of models for SN 1997eg and SN 2010jl, narrowed by the methods described in sections 2.3.2, 3.3, and 4.3, with the goal of constraining their CSM characteristics and placing limits on the ISP contributions and progenitor wind characteristics for each. Each of these models must belong to the lowest χ^2_ν cluster in the χ^2 reduction fits to the polarization spectra, pass an Anderson-Darling test for normally distributed residuals in the polarization fits, and produce a flux emission line ratio matching that of observations.

In all three best-fitting central-source cases for both comparison SNe, two groups of models are present in the low chi-square group (Fig. 5.1). Selecting for emission-line ratios based on the metric discussed at the end of section 2.3.2 laid out by the metric disclearly identifies disk models with higher shock luminosity as the preferred model group for both SNe. I identified several models of interest for epochs 1 and 2 of both SNe with the following combined statistical requirements: a χ^2_ν value that places them in the low cluster, A^2 values below the critical value confirming Gaussian

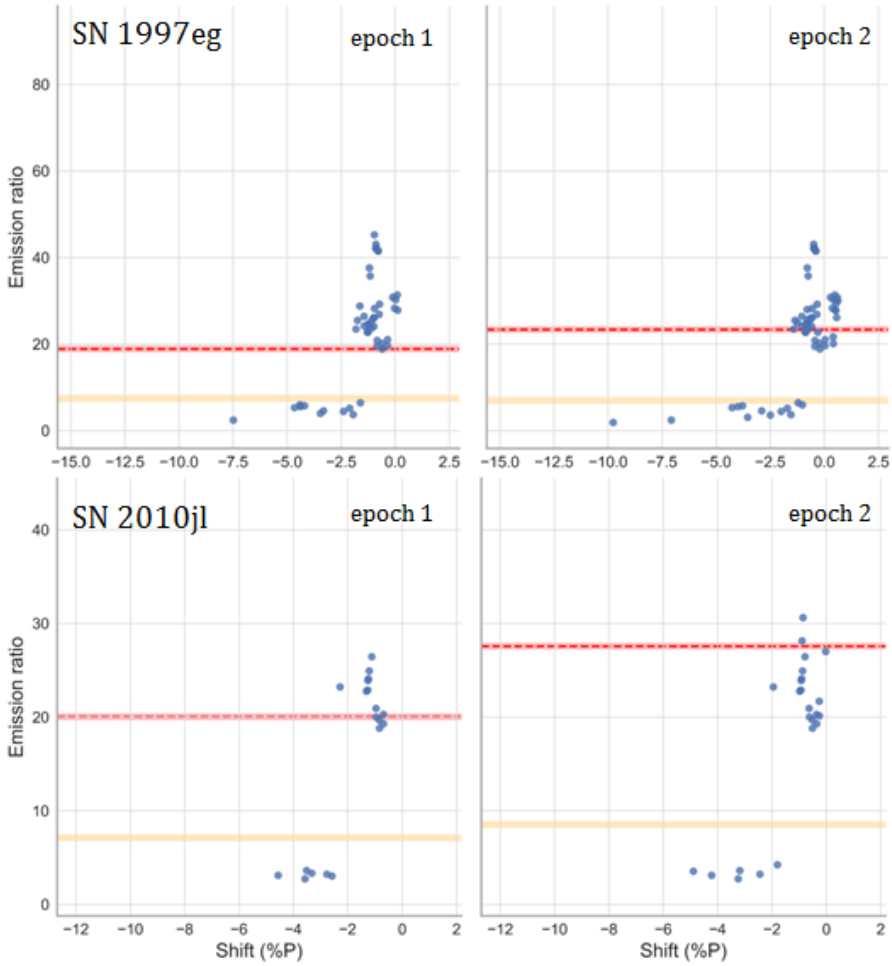

Figure 5.1: Emission line ratio vs. polarization shift for models in the low χ^2_ν cluster for epochs 1 and 2 of SN 1997eg (*top row*) and SN 2010jl (*bottom row*). Orange lines mark the observed emission-line ratio; red lines denote the average emission-line ratio for models meeting the modified criterion $0 \leq I_n - I_{int} \leq 3$ (Fig. 2.6).

residuals, and emission ratios satisfying the line region energy metric. Parameters for these models are tabulated in Tables 5.1 and 5.2.

No models meet the emission-ratio criterion in Epoch 3 for either SN. At late times, the emission lines broaden to such a degree that no models in any grid regime produce narrow emission-line ratios high enough to compensate for their intermediate-width energy. Expanding the range of the shock luminosity parameter to include more and higher values may be required to achieve matches for later

Table 5.1: Models of Interest for SN 1997eg

Parameters	Epoch 1	Epoch 2					
Geometry	disk	disk	disk	disk	disk	disk	disk
Optical Depth	0.5	0.5	0.5	1.0	1.0	0.5	2.0
$L_{\rm CSM}/L_{\rm SN}$	0.1	0.1	0.1	0.1	0.1	0.1	0.1
$L_{\rm Sh}/L_{\rm SN}$	0.2	0.2	0.2	0.2	0.2	0.2	0.2
Temp. (10^3 K)	10	20	50	20	50	20	20
Viewing Angle (°)	67	67	74	74	74	74	74
χ^2_ν	5.33	12.25	12.67	12.71	13.82	15.34	19.51
A^2	0.33	0.57	0.60	0.43	0.56	0.42	0.48
Pol. Shift[a] (%)	-0.60	-0.59	-1.04	-0.89	-1.42	-0.86	-0.30
Emission Ratio [b]	18.9	24.1	24.2	22.8	23.5	22.7	22.8
ρ (10^{-12} g cm^{-3})	2.4	2.4	2.4	4.8	4.8	2.4	9.5
$n_{\rm e}$ (10^{12} cm^{-3})	1.4	1.4	1.4	2.8	2.8	1.4	5.7

[a] Uncertainties on the polarization shift are ~ 0.32 for Epoch 1 and ~ 0.19 for Epoch 2.
[b] Uncertainties on the emission ratios are on order of 0.001.

Table 5.2: Models of Interest for SN 2010jl

Parameters	Epoch 1					Epoch 2	
Geometry	disk	disk	disk	disk	disk	disk	toroid
Optical Depth	1.0	1.0	1.0	1.0	1.0	1.0	0.5
$L_{\rm CSM}/L_{\rm SN}$	0.1	0.0	0.1	0.0	0.0	0.1	0.0
$L_{\rm Sh}/L_{\rm SN}$	0.2	0.2	0.2	0.2	0.2	0.2	0.2
Temp. (10^3 K)	10	10	10	10	10	20	20
Viewing angle (°)	74	74	59	67	59	51	67
χ^2_ν	7.73	7.95	7.99	7.99	8.14	3.93	4.14
A^2	0.62	0.60	0.60	0.58	0.59	0.25	0.17
Pol. Shift[a] (%)	-0.96	-0.96	-0.68	-0.84	-0.69	-0.89	-0.03
Emission Ratio[b]	20.0	20.9	19.3	19.7	20.3	28.2	27.0
ρ (10^{-12} g cm^{-3})	4.8	4.8	4.8	4.8	4.8	4.8	17.8
$n_{\rm e}$ (10^{12} cm^{-3})	2.8	2.8	2.8	2.8	2.8	2.8	10.0

[a] Uncertainties on the polarization shift are ~ 0.42 for Epoch 1 and ~ 0.24 for Epoch 2.
[b] Uncertainties on the emission ratios are on order of 0.001.

time intermediate-width emission spectra, whether or not velocity shifting of photon wavelengths is implemented.

All the models of interest for SN 1997eg are disk models with higher shock and CSM luminosities and inclinations of 67° or 74°. The single model identified for

Epoch 1 has a CSM temperature of 10,000 K, while all those for Epoch 2 have either 20,000 K or 50,000 K. This is interesting as the 10,000 K temperature is the only one of the three values to produce a significant difference in the ionization fraction and emission levels in the CSM, while the ionization fraction and behavior of the 20,000 K and 50,000 K models are very similar. This seems to indicate an increase in the CSM temperature from 10,000 K to between 20,000 K and 50,000 K between Epochs 1 and 2. The average emission ratio is 18.9 for Epoch 1, increasing to 23.4 for Epoch 2.

Models of interest for SN 2010jl also display some interesting trends. In Epoch 1, all are disks viewed between 59° and 74° with higher shock luminosity, optical depth of 1.0, and CSM temperature of 10,000 K, but they show no preference in the value of the CSM luminosity. Their similarities make them entirely consistent in their CSM mass and number densities. In Epoch 2 there are two models of interest, both with high shock luminosity: a disk with parameters similar to those of Epoch 1 but with a slightly lower inclination of 51°, and a toroid with an optical depth of 0.5 and inclination of 67°, both of which have a higher temperature of 20,000 K. This toroid is the only toroid model of interest for either object, but it is also notable because it requires the smallest polarization shift to fit the continuum. This model produces a polarization level very close to matching that of SN 2010jl with no translation required. The CSM for this toroid is about 5 times as dense as that of the disk models and yet fits the observational data well at the same inclination. This result has interesting implications for the evolution of SN 2010jl as well as the ISP estimates for its line of sight. Average emission ratios among these models are 20.0 and 27.6 for Epochs 1 and 2, respectively.

Despite providing good fits to the polarization of SN 2010jl, including a statistically significant fit in epoch 2, distributed models consistently produce emission line ratios far below that of observations. This suggests they do not sufficiently account

for the strong shock-CSM interaction that drives the energy output and produces the multi-component emission lines in strongly interacting SNe IIn. In particular, the assumption of the Hα flux spectrum from Epoch 1 of SN 1997eg as the spectrum emitted by the distributed source does not result in sufficient narrow-line emission. I will investigate and fine-tune this assumption in future work (§ 5.3). In the following analysis, I treat extrapolations to the observed CSM properties made from models that fail to reproduce correct narrow-line flux behavior in flux with greater skepticism, regardless of good polarization fits across the continuum.

5.1.1 Extrapolation to CSM wind characteristics

It is unclear whether models that fit well in polarization do so simply because of the asymmetry intrinsic to their geometrical shape, which becomes prominent in the statistically preferred viewing angle range of $59° - 82°$, or whether some other property of the models is in play. I find a strong preference for disk geometries among the low χ^2_ν cluster models that produce emission ratios consistent with the augmented emission metric. The largest difference between disk and toroid geometries at these viewing angles is the total amount of scattering material in the line of sight; this may provide a constraint on the mass-loss properties of the progenitor. In this section, I investigate the column densities of the best-fitting models and their implications for the geometric and wind characteristics of the CSM in each of the two SNe I studied.

I analytically calculated the longest path length through the model CSM and used this value to determine a column density at each viewing angle. Mass column density σ [g cm^{-2}] is defined the product of the mass volume density ρ and the path length L, and provides a measure of the material along a given line of sight. Observationally, σ (or, more typically, the number column density $N = nL$ [cm^{-2}]) is determined by the ratios of strengths of various spectral lines. The fact that

SLIP models fit best at higher viewing angles may indicate that these angles result in column densities akin to those implied by the observational data.

I calculated number and mass column densities for both CSM geometries at each inclination angle and for each value of optical depth. The model CSM is highly ionized within the parameter range of temperatures, even at the lowest temperature of 10,000 K. For consistency, I averaged the values for the CSM mass volume density and electron number volume density for the three temperatures (Table 2.3). Photons arriving in a given viewing angle bin will have originated from many different locations in the scattering regions, each having a distinct path length. I approximate the path length at each viewing angle as the longest distance through the CSM in the radial direction from the observed line of sight. Taking an average to account for differences in path length would be more realistic, but would not change the result substantially. At $\theta = 90°$, this path length, L_{90}, is the longest distance through the CSM and shock regions that lies tangent to the inner cavity: $L_{90} = 2\sqrt{R_o^2 - R_i^2}$ (Fig. 5.2). To determine L at other angles, I rotated L_{90} by θ around its center through a rectangular slice of CSM with a half-height equal to the toroid and disk height in the z direction. A "critical" value of θ divides two geometrical cases: $\theta crit = \tan^{-1}(L_{90}/2h)$. The resulting path lengths are given by

$$L(\theta) = \begin{cases} \frac{2h}{\cos\theta}, & \theta < \theta_{crit} \\ \sqrt{L_{90}^2 + 4h^2}, & \theta = \theta_{crit} \\ \frac{L_{90}}{2\cos(90°-\theta)} = \frac{L_{90}}{2\sin\theta}, & \theta > \theta_{crit}. \end{cases}$$

Using these values of L and the mass densities calculated by *SLIP*, I calculated mass and number column densities via $\sigma = \rho L$ and $N = nL$. I then applied these σ and N values to larger, scaled-up CSM configurations of several geometries using

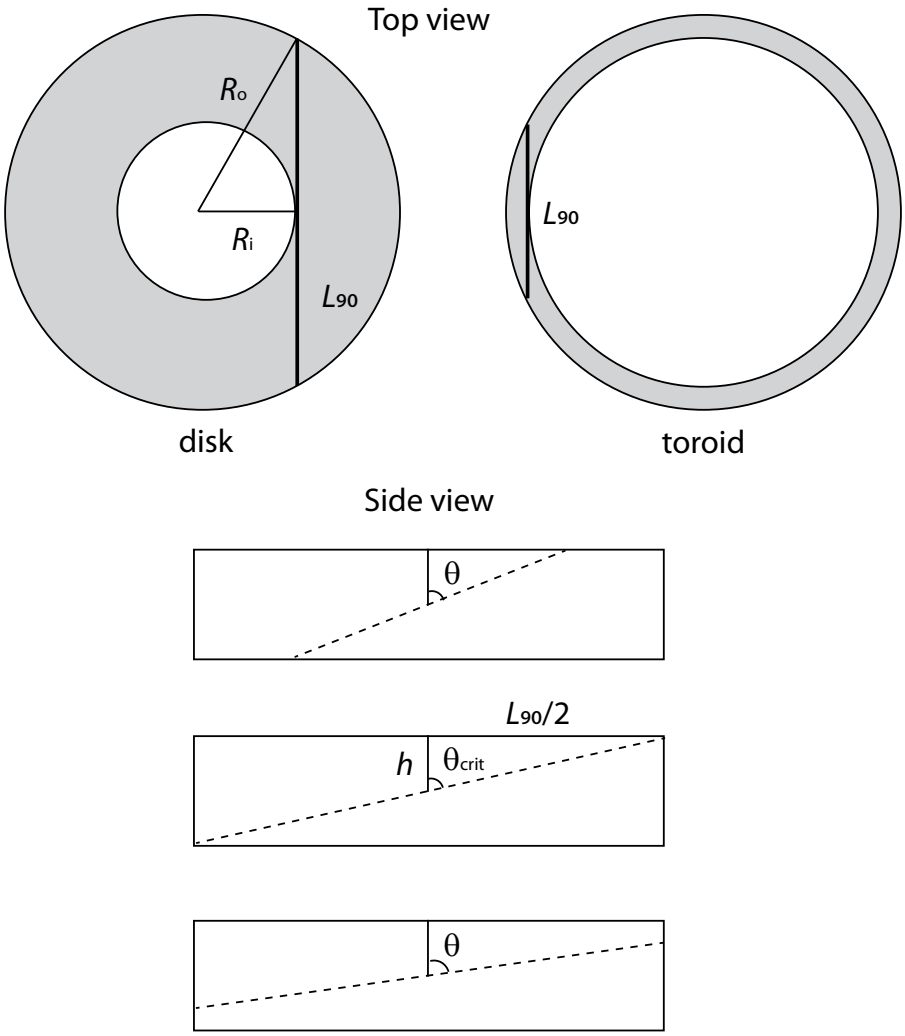

Figure 5.2: Illustration of how the longest path length L through the CSM varies with viewing angle θ. *Upper sketches:* I define L_{90} as the longest continuous horizontal distance through each CSM configuration. Lower sketches: I then express $L(\theta)$ (shown as a dashed line) in terms of L_{90} and the disk half-height h for each of three cases. Top to bottom: θ less than, equal to, and greater than the critical value corresponding to the maximum L. All sketches are to scale.

a range of plausible radii and velocities from the literature for SN 2010jl and SN 1997eg (§§3.1 and 4.1). Finally, I estimated the total mass and mass-loss rates that result from these hypothetical configurations and compared them to observational estimates for both SNe.

5.1.2 Implications for the progenitor of SN 1997eg

For SN 1997eg, Hoffman et al. (2008) proposed a disk-like CSM configuration containing $0.04 - 1.0 M_{\odot}$ with an inner radius of $\lesssim 5.7 \times 10^{15}$ cm, ejected at a rate of $1.5 \times 10^{-3} M_{\odot}$ yr^{-1} at a velocity of ~ 160 km s^{-1}. Using the days when narrow lines are present and the velocity of the shock region, these authors also estimated the outer radius to be ~ 4.2 times that of the inner, 2.5×10^{16} cm, with the mass ejection episode ending ~ 9 years prior to explosion. An alternative scenario in which the initial disappearance of narrow lines is attributed to recombination would place the inner radii at 2.4×10^{16} cm and moves the end of the ejection episode back to 40 years before explosion. In this case, the ratio of the disk radii cannot be determined, but it is likely the result of an eruption and much thinner then the previous scenario. Hoffman et al. (2008) considered ratios of $1.01 - 3$ times the inner radius in their analysis for this case.

I list mass-loss rates and ejected masses for disks of 6 different proportions with the column densities of the models of interest from Table 5.1 in Table 5.3. Disk B has the primary disk proportions considered in Hoffman et al. (2008), while Disk A uses the same lower-limit inner radius but has a thickness proportional to my models. Disks C and F use the second larger inner radius and the outer radii of the limiting thickness cases discussed in Hoffman et al. (2008), while Disks D and E have intermediate thicknesses.

Assuming the bulk of the CSM of SN 1997eg lies within the boundaries of Disk B, the mass-loss rates and total ejected masses for the column density of the Epoch 1 and first Epoch 2 models of interest are approximately $1.2\,M_{\odot}$ and $0.03 - 0.04\,M_{\odot}$ yr^{-1}, well over an order of magnitude higher then observational predictions. Using my model thickness proportions with Disk A brings the mass down considerably, but does not affect the mass-loss rate. Disk F is quite thick; if it arose from an eruption episode, that episode would have lasted ~ 143 years at the

Table 5.3: CSM wind parameters from SN 1997eg best-fit column densities

	R_i (10^{16} cm)	R_o (10^{16} cm)	t_0[a] (yr)	Δt[b] (yr)	M ($M_\odot$)	$\dot{M}$ ($M_\odot$ yr^{-1})
A	0.57	1.14	23	11	0.371	0.0329
B	0.57	2.39	47	36	1.212	0.0336
C	2.40	2.42	48	0.5	0.959	0.0200
D	2.40	2.45	49	1.0	0.982	0.0202
E	2.40	2.52	50	2.4	2.965	1.2480
F	2.40	7.20	143	95	12.226	0.1287
A	0.57	1.14	23	11	$0.371 - 0.526$	$0.0329 - 0.0466$
B	0.57	2.39	47	36	$1.212 - 1.171$	$0.0336 - 0.0476$
C	2.40	2.42	48	0.5	$0.959 - 1.360$	$0.0200 - 0.0283$
D	2.40	2.45	49	1.0	$0.982 - 1.392$	$0.0202 - 0.0287$
E	2.40	2.52	50	2.4	$2.965 - 4.203$	$1.2480 - 1.7691$
F	2.40	7.20	143	95	$12.226 - 17.330$	$0.1287 - 0.1824$
A	0.57	1.14	23	11	$0.743 - 1.053$	$0.0658 - 0.0933$
B	0.57	2.39	47	36	$2.424 - 3.437$	$0.0671 - 0.0952$
C	2.40	2.42	48	0.5	$1.920 - 2.721$	$0.0303 - 0.0567$
D	2.40	2.45	49	1.0	$1.966 - 2.786$	$0.0405 - 0.0574$
E	2.40	2.52	50	2.4	$5.932 - 8.410$	$2.4973 - 3.5400$
F	2.40	7.20	143	95	$24.464 - 34.678$	$0.2574 - 0.3649$

[a] t_0 marks the beginning of the mass-loss episode.
[b] Δt marks the duration of the mass-loss episode.
[c] Values listed for mass column density σ are [g cm^{-2}].
[d] Values listed for number column density N are [10^{23} cm^{-2}].

proposed CSM velocity of 160 km s^{-1}—not exactly episodic in nature. In addition, the column densities of our models at such a size result in an ejected mass greater than $12\,M_\odot$ at a rate of $0.1 - 0.3\,M_\odot$ yr^{-1}, which is far larger then observational constraints suggest. The opposite is true regarding the time span associated with Disk E, but the result is also problematic. Its proportions are too thin and in order to maintain the column density the mass loss rate is driven up higher then is physically reasonable. The proportions of Disks C and D yield the closest matches to the quantities derived under assumption from observations of SN 1997eg. Using the best-fit model column densities, these CSM models suggest a mass-loss episode

lasting roughly 8 months to 1.5 years, ≈ 45 years prior to explosion. Epoch 2 is also fit by an alternative model with a higher optical depth of 1.0 at the same inclinations. For this range, Disk C is still the best approximation to quantities derived from observation in previous work. The CSM parameters associated with Disk C and Disk D, however, are still an order of magnitude higher than previous estimates for $\dot{M}$, and two orders higher for M.

This poses an issue for the goal of placing constraints on the SN 1997eg progenitor. Without a good match to the wind characteristics, it is difficult to conclusively identify the CSM of SN 1997eg as resulting from either a typical LBV wind, an outburst, or an eruptive event. As seen in Fig. 5.3, mass-loss rates from giant eruptions generally have a lower limit of $10^{-2}\,M_{\odot}$ yr^{-1}. All the preferred models are well within this range, but do not come close to the observational estimates derived by Hoffman et al. (2008). At the lower observed limit for mass-loss rate, on order of $\sim 10^{-3}\,M_{\odot}$ yr^{-1}, the CSM models represented by Disks C and D come closest. SN 1997eg was estimated to have a peak magnitude M_V of between -18 and -19, with that of SN 2010jl at approximately -20 Smith et al. (2011a). This would imply a CSM mass of 1/10 to 1/100 the size of the CSM of SN 2010jl, or $1.0 - 0.1\,M_{\odot}$. It is also possible that the radii I assumed here for the CSM are too large. The estimate made via assumptions from observation, 5.7×10^{15} cm, was an upper limit. If the proportion of $R_o/R_i = 2$ is maintained as in Disk B, but R_i reduced by approximately half, the results of the calculations involving the model column densities are quite compelling. Reducing the size of the CSM thus leads to $M = 0.09 - 0.2\ M_{\odot}$. $\dot{M} = \ 0.0165 - 0.0467 M_{\odot}$ yr^{-1} and a mass-loss duration of about 5.5 years.

Either the CSM and wind characteristics derived in previous papers, and the assumptions made in calculating them, are all extreme low limits (or lower then realistic), or the column densities determined by the choice of parameters in the *SLIP* models are too high to accurately capture the wind properties of SN 1997eg.

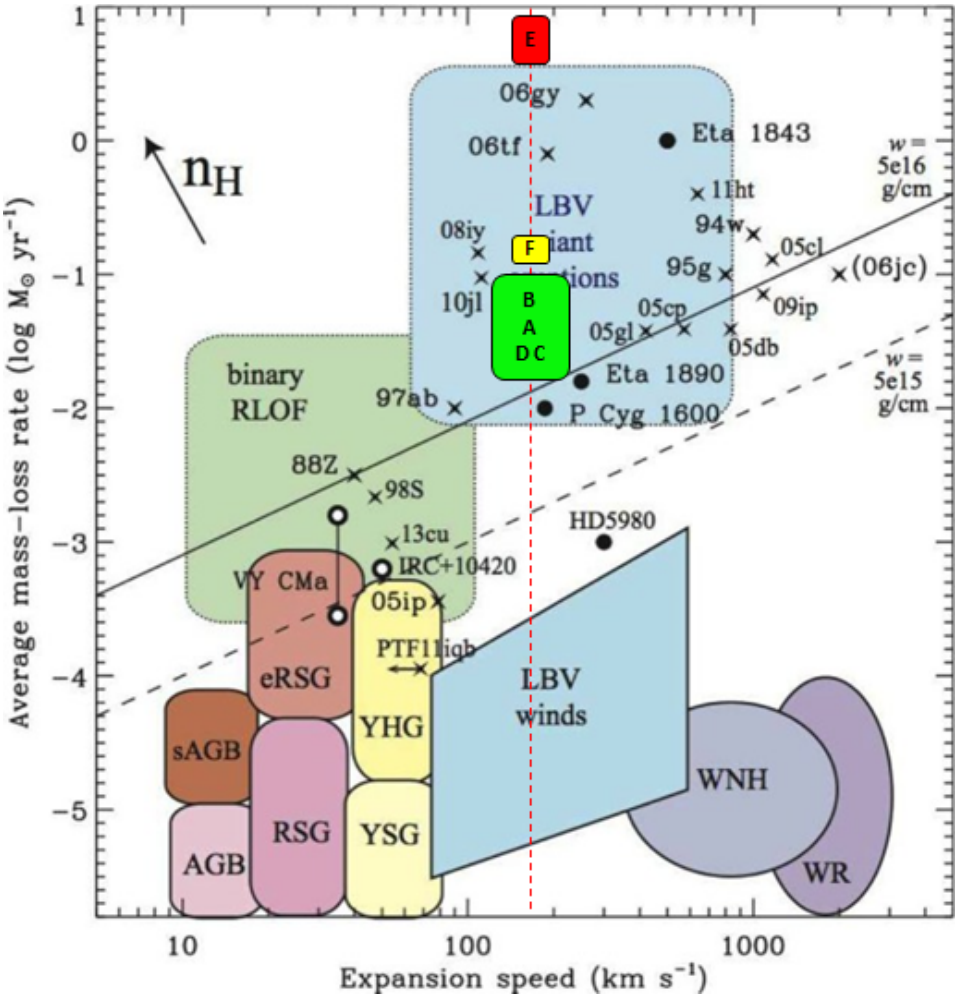

Figure 5.3: Mass-loss rates for the 5 disk models that best fit the SN 1997eg polarization data (labeled A–E), plotted on the diagram of massive star mass-loss properties first presented by Smith (2016). The red dashed line denotes the approximate CSM wind velocity of 160 km s^{-1}. The height of each lettered box roughly represents the range of mass loss rates for the column densities determined by the models of interest. Model E is marked red as mass loss associated with this scenario is not physical.

Assuming the former, then the geometric extent for the CSM of SN 1997eg has been overestimated and its total mass underestimated. Taking the reconsidered values discussed above, and if my *SLIP* models correctly approximate the column density N_e, then the ejection of the CSM around SN 1997eg could be attributed to a relatively weak eruption event on the lower end of LBV eruptions, similar to the 1600 eruption of P Cygni, between 5 to 10 years prior to explosion (Fig. 5.3).

According to Humphreys and Davidson (1994), wind-like mass-loss rates of LBVs in active S Doradus phases are on average around $2 - 3 \times 10^{-4}\, M_{\odot}\mathrm{yr}^{-1}$ (but potentially as high as $\sim 10^{-3}\, M_{\odot}\mathrm{yr}^{-1}$) and occur on timescales of roughly $10 - 40$ years. S Doradus phases cycle on two timescales during a post-RSG evolutionary phase through the S-Dor strip: short (S SD-phases) $\lesssim 10$ and long (L SD-phases) $\gtrsim 20$ years (van Genderen 2001). These authors note that that that all the visible CSM lost during an active SD-phase would not total more than a few solar masses, provided there were no major eruptions. Vink (2012) finds that LBV phenomenon are not restricted to stars of extreme high mass, and can extend down to massive stars with main-sequence masses as low as $25M_{\odot}$. Papers by Cox and Guzik (2009) calculated hydrodynamic models of pulsational instabilities in single stars with super-Eddington luminosity layers, as a potential explanation for the enhanced mass loss during these milder SD-phase outbursts. They find that surface eruptions in these models amount to about 0.0001 of the total model mass.

If one considers a possible progenitor in an S SD-phase with enhanced mass-loss between $2 - 4 \times 10^{-4} M_{\odot}$ yr^{-1} over a period of 5–10 years, it could create a CSM mass of $0.001 - 0.004 M_{\odot}$. If the mass loss is as high as $1 \times 10^{-3} M_{\odot}$ yr^{-1} over the same period, a total of $0.005 - 0.01$ masses can be ejected, which more closely agrees with mass loss estimates derived from observations by Hoffman et al. (2008). The caveat to this is that if only a single SD-phase is traversed prior to explosion, the ratio of the outer and inner radii must be approximately 2, or else multiple periods of mass loss would be completed in between these radii. This issue can be solved if we consider instead a wind-like CSM built up from repeated outbursts over multiple cycles, which would aid in increasing the total CSM mass despite a slightly lower mass-loss rate. If the approximations in Hoffman et al. (2008) are accurate, the channel for the likely production of the CSM around SN 1997eg is narrowed to something along the lines of an LBV of lower initial mass of $25 - 40 M_{\odot}$ in a post-

RSG stage that had just ended an S SD-phase outburst cycle, producing a lower mass, wind-like CSM.

5.1.3 Implications for the progenitor of SN 2010jl

I compiled information from Ofek et al. (2014), Chandra et al. (2015), Fransson et al. (2014), and Borish et al. (2015) as the observational basis for my conclusions about the progenitor of SN 2010jl. There is good agreement among these authors that the velocity of the CSM is $\approx$ 100 km s^{-1}; I adopted the estimate by Ofek et al. (2014) of 105 km s^{-1}. Modeling by Chandra et al. (2015) revealed a distinct break in the power law index of the wind density at $\sim 1.3 \times 10^{16}$ cm, which led these authors to conclude that the bulk of the ejected mass must lie below this value. Alternatively, Fransson et al. (2014) estimated an outer radius of 2×10^{16} cm. Using the 3000 km s^{-1} value for the shock velocity quoted by both Ofek et al. (2014) and Fransson et al. (2014) and an approximate cooling time of $\sim$ 1 year, I found a corresponding inner radius of $\sim 3.5 \times 10^{15}$ cm, about 10 times smaller than the Fransson outer radius. I considered both of these potential CSM sizes in my analysis below.

Aggregating information from all the sources above, I assumed a CSM mass of no less then 3 $M_{\odot}$ (but more likely in the range of $10 - 16$ $M_{\odot}$) ejected at a rate of $0.1 M_{\odot}$ yr^{-1}. The authors cited above agree that models with spherical CSM geometries and these mass-loss characteristics do not yield consistent masses or mass-loss rates. They conclude there is some level of asymmetry in the system, which they attribute to bipolar flows similar to those seen in η Carinae. Despite its large mass and high implied mass-loss rates, the CSM of SN 2010jl has a density profile that is surprisingly wind-like ($\rho \sim r^{-2}$) up to the outer estimated radius (Chandra et al. 2015; Ofek et al. 2014). Ofek et al. (2014) proposed periodic pair-instability pulsations as an alternative to the standard LBV eruption mass-loss mechanism

in this supernova. If they occurred with a short enough period, such pulsations could push off large amounts of mass into a radially thicker wind-like distribution. Thus, for SN 2010jl, I considered both a shell (eruptive) and a solid CSM geometry (periodic pulsations) when calculating model CSM mass and mass-loss rates.

In Table 5.4, I list mass-loss rates and ejected masses for disk and ellipsoidal arrangements of CSM of three different proportions, for both the shell and solid volume, determined from the column densities of the models of interest in Table 5.2. I will refer to the first CSM model in each set as A ($R_o/R_i = 3.7$), the second as B ($R_o/R_i = 10$), and the third as C ($R_o/R_i = 1.3$). Both A and B for each CSM scenario are based on observational estimates from the sources discussed previously. I determined CSM C sizes from the time and duration of a typical LBV eruptive episode given the measured velocity of the CSM. For an eruption lasting 10 years and beginning 40 years prior to explosion, the resulting radii are 9.9×10^{15} cm and 1.3×10^{16} cm. I chose this size as a check on the values for M and $\dot{M}$ when times are constrained to observations of this type of mass-loss mechanism.

The fascinating result here is that *all* the potential CSM wind parameters defined by the column densities of the best-fitting models lie well within the ranges typical of giant LBV eruptions. Comparing size of each CSM and its associated duration with the values for M and $\dot{M}$ can shed light on which CSM geometry is plausible. The lower limit for the mass of the CSM around SN 2010jl from data and modeling based on its magnitude and light curve is $3M_{\odot}$. Right away, all the disk geometries can be eliminated from consideration, as they do not contain enough volume of material for an envelope of that size. In Epoch 1, eruptive shell Ellipsoids B and C reach that lower limit. Ellipsoid C is compelling, because the size is based on eruption durations and its mass loss rate is on order of $10^{-1} M_{\odot}$ yr^{-1}. The Epoch 2 models with column densities from the *SLIP* disk at the lower inclination are not quite high enough in either quantity. The Epoch 2 models based on *SLIP* toroid

Table 5.4: CSM wind parameters from SN 2010jl best-fit column densities

CSM		R_i (10^{16}cm)	R_o (10^{16}cm)	t_0 (yr)	Δt (yr)	M ($M_\odot$)	$\dot{M}$ ($M_\odot$ yr^{-1})
Disk	Eruptive	0.35	1.3	39	29	$0.564 - 1.054$	$0.0198 - 0.0369$
		0.20	2.0	60	54	$1.100 - 2.056$	$0.0203 - 0.0379$
		0.99	1.3	40	10	$1.000 - 1.869$	$0.1011 - 0.1889$
	Steady	-	1.3	39	-	$0.419 - 0.783$	$0.0107 - 0.0200$
		-	2.0	60	-	$0.991 - 1.852$	$0.0164 - 0.0307$
		-	1.3	40	-	$0.432 - 0.807$	$0.0108 - 0.0203$
Ell	Eruptive	0.35	1.3	39	29	$1.253 - 2.342$	$0.0439 - 0.0821$
		0.20	2.0	60	54	$2.445 - 4.569$	$0.0450 - 0.0842$
		0.99	1.3	40	10	$2.223 - 4.154$	$0.2247 - 0.4198$
	Steady	-	1.3	39	-	$0.931 - 1.739$	$0.0237 - 0.0444$
		-	2.0	60	-	$2.203 - 4.117$	$0.0365 - 0.0682$
		-	1.3	40	-	$0.960 - 1.793$	$0.0241 - 0.0450$
Disk	Eruptive	0.35	1.3	39	29	0.462	0.0162
		0.20	2.0	60	54	0.901	0.0166
		0.99	1.3	40	10	0.819	0.0827
	Steady	-	1.3	39	-	0.343	0.0087
		-	2.0	60	-	0.811	0.0134
		-	1.3	40	-	0.353	0.0089
Ell	Eruptive	0.35	1.3	39	29	1.026	0.0359
		0.20	2.0	60	54	2.001	0.0369
		0.99	1.3	40	10	1.819	0.1839
	Steady	-	1.3	39	-	0.762	0.0194
		-	2.0	60	-	1.803	0.0299
		-	1.3	40	-	0.785	0.0197
Disk	Eruptive	0.35	1.3	39	29	2.762	0.0968
		0.20	2.0	60	54	5.389	0.0992
		0.99	1.3	40	10	4.898	0.4950
	Steady	-	1.3	39	-	2.051	0.0523
		-	2.0	60	-	4.855	0.0805
		-	1.3	40		2.115	0.0531
Ell	Eruptive	0.35	1.3	39	29	6.137	0.2151
		0.20	2.0	60	54	11.975	0.2205
		0.99	1.3	40	10	10.885	1.1001
	Steady	-	1.3	39	-	4.558	0.1162
		-	2.0	60	-	10.788	0.1788
		-	1.3	40	-	4.699	0.1180

densities also produce ellipsoidal CSM configurations with target M and $\dot{M}$ much closer to observation. Of note are the same group of models from Epoch 1: eruptive Ellipsoids B and C, and steady ellipsoid B.

Episodic ellipsoid B is on target with a mass-loss rate and ejected mass expected for a giant LBV eruption, as well as agreeing with estimates in the literature derived from observation. However, the size of this ellipsoid hardly qualifies it for a single mass-loss episode, as the duration associated with the thickness is around 50 years. Episodic ellipsoid B gets the timing and mass right, but is about an order of magnitude higher in $\dot{M}$. Interestingly, the steady ellipsoid B is not far off from the values generated by the episodic case, but this is not surprising given the large thickness of CSM B.

It is fairly conclusive that the progenitor of SN 2010jl was an evolved LBV star of quite high mass. The steady ellipsoid scenario with CSM size B may not agree with the time scales for an η Car or P-Cyg like giant eruption, but it is perfectly compatible with the wind-like density profiles inferred from previous observations, and supports the alternative hypothesis posed by (Ofek et al. 2014) for repeated pulsations of a pair-instability driven mechanism for the mass ejection, a phenomenon requiring an initial main-sequence mass of at least $40-60M_{\odot}$, if not higher (Yoshida et al. 2016).

5.1.4 Estimations of the ISP

I list the values of the polarization shift for the models of interest for both SNe in Tables 5.1 and 5.2.

For SN 1997eg, I find that the average shifts of the models constrain the ISP to $0.60\% \pm 0.41\%$ for Epoch 1 and $0.83\% \pm 0.24\%$ for Epoch 2. When averaged, these shifts span a range of $0.24\% - 1.2\%$. Hoffman et al. (2008) proposed three estimates for the total ISP in the direction of the host galaxy NGC 5012: 2.9%,

Table 5.5: ISP estimates for SN 1997eg

	Central-source				Distributed-source			
	1	2	3	avg	1	2	3	avg
All low cluster	-1.53	-1.04	-2.11	-1.56	-2.60	-2.36	-2.96	-2.64
	0.42	0.24	0.26	0.55	0.42	0.24	0.26	0.55
High emission	-0.89	-0.34	-0.32	-0.51	-	-	-	-
	0.42	0.24	0.26	0.55	-	-	-	-
Low emission	-3.63	-3.49	-3.05	-3.39	-	-	-	-
	0.42	0.24	0.26	0.55	-	-	-	-
Obs.ratio match	-	-	-	-	-1.71	-	-	-1.71
	-	-	-	-	0.42	-	-	0.42
Excess E match	-0.60	-0.83	-	-0.72	-	-	-	-
	0.41	0.24	-	0.48	-	-	-	-
Avg. ratio of excess E match	18.89	23.38	-		-	-	-	-

All averages are given as percent polarization with associated uncertainty listed under the reported value. For some criteria a model could not be identified within the low χ^2_ν cluster. For the distributed-source models, separate high and low emission populations do not exist, as well as any models with the correct excess narrow line area. Averages unable to be determined in a given epoch are replaced with dashes.

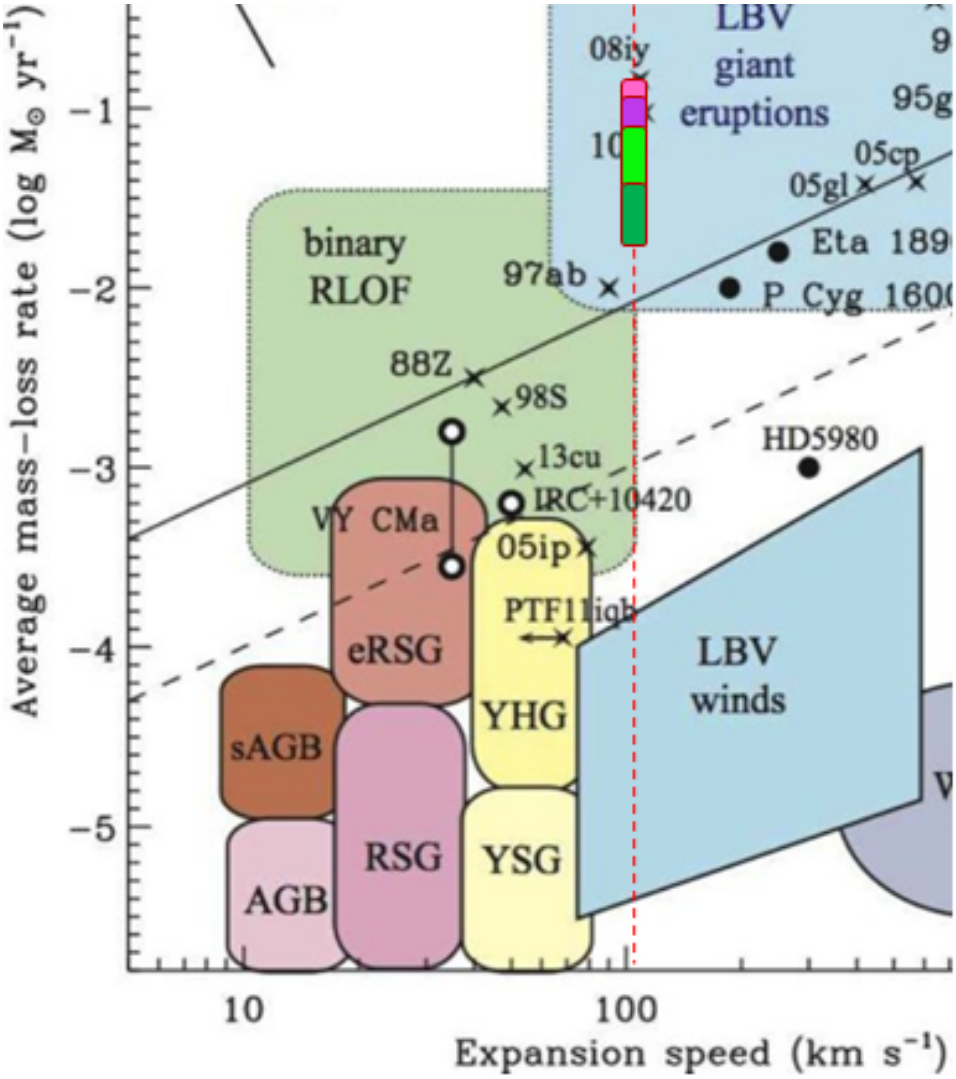

Figure 5.4: Mass-loss rates for 4 CSM models that best fit the SN 2010jl polarization data, plotted on the diagram of massive star mass-loss properties first presented by Smith (2016). The red dashed line denotes the approximate CSM wind velocity of 105 km s^{-1}. The colored boxes represent different model groups: light pink represents Ellipsoid B, the purple Ellipsoid A, light green is Disk B, dark green is Disk A. The height of each box roughly represents the range of mass loss rates for each group of models. Note that *all* the potential wind parameters defined by the model column densities lie well within the range of those of giant LBV eruptions.

2.0%, and 1.4%. They preferred the largest estimate, but also suggested there was a contribution from elongated ejecta that if subtracted would could bring down the estimates to a smaller value. While the polarization shift values I obtain above are

Table 5.6: ISP estimates for SN 2010jl

	Central-source				Distributed-source			
	1	2	3	avg	1	2	3	avg
All low cluster	-1.84	-1.33	-1.82	-1.66	-2.71	-2.82	-2.72	-2.75
	0.32	0.19	0.28	0.46	0.32	0.19	0.28	0.46
High emission	-1.13	-0.70	-1.09	-0.97	-	-	-	-
	0.32	0.19	0.28	0.46	-	-	-	-
Low emission	-3.39	-3.30	-3.27	-3.32	-	-	-	-
	0.32	0.19	0.28	0.46	-	-	-	-
Obs.ratio match	-	-	-	-	-2.18	-2.50	-	-2.34
	-	-	-	-	0.32	0.19	-	0.26
Excess E match	-0.79	-0.46	-	-0.63	-	-	-	-
	0.32	0.19	-	0.46	-	-	-	-
Avg. ratio of excess E match	19.81	27.58	-	23.70	-	-	-	-

All averages are given as percent polarization with associated uncertainty listed under the reported value. For some criteria a model could not be identified within the low χ^2_ν cluster. For the distributed-source models, separate high and low emission populations do not exist, as well as any models with the correct excess narrow line intensity. Averages unable to be determined in a given epoch are replaced with dashes.

below the lowest estimate given by Hoffman et al. (2008), I note that *SLIP* does not yet model the extra contribution they propose; if this were added, it would increase the upper limit of the average polarization shift. Additionally, the lowest level of polarization near the center of the Hα line in the best-fitting *SLIP* models hovers just above 1.5%. These lines of reasoning lead me to conclude that an ISP estimate of 1.4% is the most likely value for SN 1997eg.

In the case of SN 2010jl, the ISP contributions are constrained by the shifts of my best-fit models to an average of 0.79% $\pm$ 0.32% for Epoch 1 and 0.46% $\pm$ 0.19% for Epoch 2. ISP estimates made by Patat et al. (2011) are quite small due to the relatively parallel inclinations of both the Milky Way and the host galaxy. They estimate a Milky Way contribution less than or equal to 0.2% and the host contribution at 0.3%, for a total upper limit of 0.5%. The values obtained in this

work are consistent with those given by Patat et al. (2011), and I therefore agree with these authors. Our uncertainties are wider then the estimated host contribution and cannot be used to make a claim about the Milky Way component at this time.

5.2 Summary

Inclination, optical depth, and radial CSM thickness are the driving factors in selection of best-fitting models via the polarization spectra and the Hα emission line ratio fitting process. This is likely a twofold effect depending both on the global CSM asymmetry and the density of the material for a given geometry/optical depth combination and viewing angle. The initial selection for models within the low χ^2_{nu} cluster strongly favors models with inclinations $> 57°$. The preference across the board for models with high inclination does point to an interesting possible conclusion. Categorization of strongly interacting SNe IIn may *necessitate* an inclination component altogether. Viewed at a different angle, these SNe could appear entirely different.

The secondary selection for models with the correct levels of line emission is not inherently preferential to inclination or density. When performed on the entire set of models without removing those that fit in the polarization, models of all inclinations and optical depths can be found within the limiting criteria. However, the correct levels of emission in the line do influence the level of polarization across the line: those with larger emission spikes should drive the depolarization lower and ultimately affect the fit. Pulling apart the contributions from both of these factors is beyond the scope of this work, and I will consider it in future work.

I find that previous estimates of the radial size of the CSM of SN 1997eg, and mass contained within it, are likely low. The discrepancies between the *SLIP* models I present here and the observed Hα polarization of SN 1997eg suggest several areas of future code development. I present two possible progenitor scenarios to fit the

the wind characteristics of the CSM determined by the modeling in this work, both of which imply a lower mass LBV between $25 - 40 M_{\odot}$:

1. A single P-Cygni-like eruption of $0.09 - 0.2 M_{\odot}$ *or*

2. An extended S SD-phase of $5-10$ years, with a mass-loss rate of $10^{-3} M_{\odot}$ yr^{-1}.

A binary companion could potentially explain the slightly enhanced rate, when compared to rates typical of LBVs in S-Dor like outbursts, and equatorial concentration.

The CSM wind characteristics of SN 2010jl I determine from my modeling are a good match for an LBV of very high initial mass, $60 M_{\odot}$ or higher, driving off $0.15 - 0.2 M_{\odot}$ yr^{-1} over a period of about 60 years. This scenario is physical for a star undergoing pulsations from pair instability in the years leading up to collapse.

The ISP estimates I made from the vertical shifts of the model continuum polarization agree with observational estimates for both objects. In the case of SN 1997eg, I narrow the ISP estimates presented by Hoffman et al. (2008) and suggest that the ISP in the direction of NGC 5012 is $1.2\% - 1.4\%$. In the case of SN 2010j, my estimates agree with the total ISP prediction of 0.5% from Patat et al. (2011), although they cannot conclusively aid in separating the Milky Way and host galaxy components. These results are an indication of the success of this method in constraining ISP determinations, and are quite exciting for their potential as predictors in future work.

5.3 Future Work

The results of this work have shed light on many possible additions and improvements for *SLIP* and improve its accuracy in modeling SNe interaction. The ability to consider ϕ-dependent geometries, including clumps, is already in a working phase post-development. The goal of this project is to model the production of $Q - U$

loops across spectral lines in SNe and thus determine how clumps and geometric asymmetries contribute to observed line polarization behavior.

As multi-component emission lines are the defining feature of SNe IIn, it is vital that *SLIP* become more realistic in reproducing the physics responsible for producing each part. The most immediate priority toward this goal is the addition of Doppler shift capabilities to simulate expanding scattering regions. Photons that are emitted from or interact with material within the shock and CSM regions will build up the intermediate line width and enable us to properly fit this region of the line. Addition and implementation of this physics is already underway.

I plan to investigate splitting the shock region into two thinner layers: a dense, absorbing layer on the interior and one above that that radiates strong emission from the conversion of kinetic energy, proportional to the mass contained in the swept-up layer below. This is particularly important in the case of distributed models, as use of the SN 1997eg spectrum as input in this region was not sufficient to reproduce the amount of energy that should be released in the interaction. Increasing the maximum value of the shock luminosity, in the case of the central-source models, will also be necessary for the creation of output emission flux spectra that reproduce observations.

Increasing the optical depth of the inner shock layer could serve as another way to reproduce the shrouded nature of IIn I attempted to recreate with the distributed models. This has not been attempted previously out of sheer computational difficulty. Signal-to-noise is quite low for such models, resulting in very high run times with distributed regions of high opacity. An augmented scattering method needs to be devised that will reasonably allow enough light to pass through, but with wavelengths altered by scattering in material with high electron optical depth. This would simultaneously reduce the effective path length of the observable column density in order to simulate the opaqueness of the later to photons below and more

effectively reproduce the broadest components of the emission lines and widen the potential fitting region of the line.

I also intend to investigate trading the separate geometry and optical depth parameters for a single ellipsoidal or spherical CSM defined by a density profile in r and θ, with a total estimated CSM mass distributed over its volume. Instead of selecting a density profile for a given geometry, *SLIP* would dynamically calculate the optical depth of the configuration and result in column densities that vary more realistically with viewing angle.

Lastly, I plan to fit the results of these improved models to the spectra of more and more varied SNe of all subtypes. We are in an age where the rate of our observations outstrips the pace of our theoretical understanding for all of astronomy, but especially in the area of massive stars and SNe. I hope to bring *SLIP* into the forefront of this fray to assist in unraveling our understanding of massive stars and their deaths.

Bibliography

Aldering, G., R. M. Humphreys, and M. Richmond

1994. SN 1993J: The optical properties of its progenitor. *AJ*, 107(1):662.

Andrae, R., T. Schulze-Hartung, and P. Melchior

2010. Dos and don'ts of reduced chi-squared. *ArXiv e-prints*, Pp. 1–12.

Arcavi, I., A. Gal-Yam, S. B. Cenko, D. B. Fox, D. C. Leonard, D.-S. Moon, D. J. Sand, A. M. Soderberg, M. Kiewe, O. Yaron, A. B. Becker, R. Scheps, G. Birenbaum, D. Chamudot, and J. Zhou

2012. Caltech Core-Collapse Project (CCCP) Observations of Type II Supernovae: Evidence for Three Distinct Photometric Subtypes. *ApJ*, 756(2):L30.

Aretxaga, I., S. Benetti, R. J. Terlevich, A. C. Fabian, E. Cappellaro, M. Turatto, and M. della Valle

1999. SN 1988Z: spectro-photometric catalogue and energy estimates*. *MNRAS*, 309:343–354.

Arnett, W. D.

1969. Exploding Star Models and Supernovae. In *Explod. Star Model. Supernovae*, P. Brancazio and A. G. W. Cameron, eds., P. 89, New York City. Gordon and Breach.

Arnett, W. D., J. N. Bahcall, R. P. Kirshner, and S. E. Woosley

1989. Supernova 1987A. *ARA&A*, 27(1):629–700.

Baade, W. and F. Zwicky

1934. On Super-novae. *Proc. Nat. Acad. Sci.*, 20(5):254–259.

Bauer, F. E., P. Zelaya, A. Clocchiatti, and J. Maund

2012. Spectropolarimetry of Type IIn SN2010jl: Peering Into the Heart of a Monster. In *Death Massive Stars Supernovae Gamma-Ray Bursts*, P. Roming, N. Kawai, and E. Pian, eds., number 279 in IAU Symposium, Pp. 325–326.

Benetti, S., F. Bufano, J. Vinko, G. H. Marion, T. Pritchard, J. C. Wheeler, E. Chatzopoulos, and M. Shetrone

2010. Supernova 2010jl in UGC 5189A. *Central Bureau Electronic Telegrams*, 2536.

Bilinski, C., N. Smith, W. Li, G. G. Williams, W. Zheng, and A. V. Filippenko

2015. Constraints on Type IIn Supernova Progenitor Outbursts from the Lick Observatory Supernova Search. *MNRAS*, 450(1):246–265.

Borish, H. J., C. Huang, R. A. Chevalier, B. M. Breslauer, A. M. Kingery, and G. C. Privon

2015. Near-infrared Spectroscopy of the Type IIn SN 2010jl: Evidence for High Velocity Ejecta. *ApJ*, 801(1):11.

Bose, S., F. Sutaria, B. Kumar, C. Duggal, K. Misra, P. J. Brown, M. Singh, V. Dwarkadas, D. G. York, S. Chakraborti, H. C. Chandola, J. Dahlstrom, A. Ray, and M. Safonova

2015. SN 2013ej: A Type IIL Supernova with Weak Signs of Interaction. *ApJ*, 806(2):160.

Burbidge, E. M., G. R. Burbidge, W. A. Fowler, and F. Hoyle

1957. Synthesis of the elements in stars. *Rev.Mod.Phys.*, 29(4):547–650.

Chandra, P., R. A. Chevalier, N. Chugai, C. Fransson, and A. M. Soderberg

2015. X-Ray and Radio Emission from Type IIn Supernova SN 2010jl. *ApJ*, 810:32.

Chugai, N. N., S. I. Blinnikov, R. J. Cumming, P. Lundqvist, A. Bragaglia, A. V. Filippenko, D. C. Leonard, T. Matheson, and J. Sollerman

2004. The type IIn supernova 1994W: evidence for the explosive ejection of a circumstellar envelope. *MNRAS*, 352:1213–1231.

Claeys, J. S. W., S. E. de Mink, O. R. Pols, J. J. Eldridge, and M. Baes

2011. Binary progenitor models of type IIb supernovae. *A&A*, 528:A131.

Clarke, D.

2009. Stellar Polarimetry.

Cohen, M. H.

2005. *The LRIS Polarimeter (Keck Observatory Instrument Manual).*

Cox, A. N. and J. A. Guzik

2009. Pulsation and convection in Luminous Blue Variable stars. *Communications in Asteroseismology*, 158:259.

Dessart, L. and D. J. Hillier

2011. Synthetic line and continuum linear-polarization signatures of axisymmetric Type II supernova ejecta. *MNRAS*, 415:3497–3519.

Dwarkadas, V.

2011. On Luminous Blue Variables as the Progenitors of Core Collapse Supernovae, especially Type IIn supernovae. *MNRAS*, 412(3):1639–1649.

Elias-Rosa, N., S. D. Van Dyk, W. Li, A. A. Miller, J. M. Silverman, M. Ganeshalingam, A. F. Boden, M. M. Kasliwal, J. Vinkó, J.-C. Cuillandre, A. V. Filippenko, T. N. Steele, J. S. Bloom, C. V. Griffith, I. K. W. Kleiser, and R. J. Foley

2010. The Massive Progenitor of the Type II-linear Supernova 2009kr. *ApJ*, 714(2):L254–L259.

Fewell, M. P.

1995. The atomic nuclide with the highest mean binding energy. *AJPh*, 63(7):653–658.

Filippenko, A. V.

1997. Optical Spectra of Supernovae. *ARA&A*, 35(1):309–355.

Fransson, C., M. Ergon, P. J. Challis, R. A. Chevalier, K. France, R. P. Kirshner, G. H. Marion, D. Milisavljevic, N. Smith, F. Bufano, A. S. Friedman, T. Kangas, J. Larsson, S. Mattila, S. Benetti, R. Chornock, I. Czekala, A. Soderberg, and J. Sollerman

2014. High-density Circumstellar Interaction in the Luminous Type IIn SN 2010jl: The First 1100 Days. *ApJ*, 797:118.

Gal-Yam, A., S. B. Cenko, D. W. Fox, D. C. Leonard, D.-S. Moon, D. J. Sand, and A. M. Soderberg

2005. The Caltech Core-Collapse Project (CCCP). In *1604-2004: Supernovae as Cosmological Lighthouses*, M. Turatto, S. Benetti, L. Zampieri, and W. Shea, eds., volume 342 of *ASPConf.Ser.*, P. 305.

Gal-Yam, A., D. C. Leonard, D. B. Fox, S. B. Cenko, A. M. Soderberg, D.-S. Moon, D. J. Sand, Caltech Core Collapse Program, W. Li, A. V. Filippenko, G. Aldering, and Y. Copin

2007. On the Progenitor of SN 2005gl and the Nature of Type IIn Supernovae. *ApJ*, 656(1):372–381.

Hauschildt, P. H. and E. Baron

1999. Numerical solution of the expanding stellar atmosphere problem. *J. Comput. Appl. Math*, 109(1-2):41–63.

Heger, A., C. L. Fryer, S. E. Woosley, N. Langer, and D. H. Hartmann

2003. How Massive Single Stars End Their Life. *ApJ*, 591(1):288–300.

Henney, W. J.

1994. Polarization profiles of scattered emission lines. I. General formalism for optically thin Rayleigh scattering. *ApJ*, 427(1):288–304.

Hoffman, J. L., D. C. Leonard, R. Chornock, A. V. Filippenko, A. J. Barth, and T. Matheson

2008. The Dual Axis Circumstellar Environment of the Type IIn Supernova 1997eg. *ApJ*, 688(2):1186–1209.

Höflich, P. A.

1991. Asphericity Effects in Scattering Dominated Photospheres. *A&A*, 246(2):481.

Humphreys, R. M. and K. Davidson

1994. The luminous blue variables: Astrophysical geysers. *PASP*, 106:1025–1051.

Iglewicz, B. and D. C. Hoaglin

1993. *How to Detect and Handle Outliers*, volume 16. ASQC/Quality Press.

Inserra, C., M. Turatto, A. Pastorello, S. Benetti, E. Cappellaro, M. L. Pumo, L. Zampieri, I. Agnoletto, F. Bufano, M. T. Botticella, M. Della Valle, N. Elias Rosa, T. Iijima, S. Spiro, and S. Valenti

2011. The Type IIP SN 2007od in UGC 12846: From a bright maximum to dust formation in the nebular phase. *MNRAS*, 417(1):261–279.

Irwin, J.

2007. *Astrophysics: Decoding the Cosmos*. Wiley.

Jackson, J. D.

1998. *Classical Electrodynamics, 3rd Edition*. Wiley.

Jeffery, D. J.

1987. The polarization spectrum of supernova 1987A interpreted in terms of shape asymmetry. *Nature*, 329(6138):419–421.

Kasen, D., P. Nugent, L. Wang, D. A. Howell, J. C. Wheeler, P. Höflich, D. Baade, E. Baron, and P. H. Hauschildt

2003. Analysis of the Flux and Polarization Spectra of the Type Ia Supernova SN 2001el: Exploring the Geometry of the High-Velocity Ejecta. *ApJ*, 593(2):788–808.

Kiewe, M., A. Gal-Yam, I. Arcavi, D. C. Leonard, J. Emilio Enriquez, S. B. Cenko, D. B. Fox, D.-S. Moon, D. J. Sand, and A. M. Soderberg

2012. Caltech Core-Collapse Project (CCCP) Observations of Type IIn Supernovae: Typical Properties and Implications for Their Progenitor Stars. *ApJ*, 744(1):10.

Leloudas, G., E. Y. Hsiao, J. Johansson, K. Maeda, T. J. Moriya, J. Nordin, T. Petrushevska, J. M. Silverman, J. Sollerman, M. D. Stritzinger, F. Taddia, and D. Xu

2015. Supernova spectra below strong circumstellar interaction. *A&A*, 574:A61.

Leonard, D. C. and A. V. Filippenko

2000. Evidence for Asphericity in the Type IIN Supernova SN 1998S. *ApJ*, 536:239–254.

Leonard, D. C., A. V. Filippenko, M. Ganeshalingam, F. J. D. Serduke, W. Li, B. J. Swift, A. Gal-Yam, R. J. Foley, D. B. Fox, S. Park, J. L. Hoffman, and D. S. Wong

2006. A non-spherical core in the explosion of supernova SN 2004dj. *Nature*, 440:505–507.

Maund, J. R., J. C. Wheeler, F. Patat, L. Wang, D. Baade, and P. A. Höflich

2007. Spectropolarimetry of the Type IIb Supernova 2001ig. *ApJ*, 671(2):1944–1958.

Miller, A. A., J. M. Silverman, N. R. Butler, J. S. Bloom, R. Chornock, A. V. Filippenko, M. Ganeshalingam, C. R. Klein, W. Li, P. E. Nugent, N. Smith, and T. N. Steele

2010. SN 2008iy: an unusual Type IIn Supernova with an enduring 400-d rise time. *MNRAS*, 404(1):305–317.

Miller, J. S. and R. P. S. Stone

1993. Lick Observatory Technical Report. Technical report, Univ. of California, Santa Cruz.

Modjaz, M., L. Kewley, J. S. Bloom, A. V. Filippenko, D. Perley, and J. M. Silverman

2011. Progenitor Diagnostics for Stripped Core-Collapse Supernovae: Measured Metallicities At Explosion Sites. *ApJ*, 731(1):L4.

Nakano, S. and M. Aoki

1997. Supernova 1997eg in NGC 5012. *IAUCirc.*, 6790.

Newton, J. and T. Puckett

2010. Possible Supernova in UGC 5189A. *IAUCirc.*, 2532.

Ofek, E. O., A. Zoglauer, S. E. Boggs, N. M. Barriére, S. P. Reynolds, C. L. Fryer, F. A. Harrison, S. B. Cenko, S. R. Kulkarni, A. Gal-Yam, I. Arcavi, E. Bellm, J. S. Bloom, F. Christensen, W. W. Craig, W. Even, A. V. Filippenko, B. Grefenstette, C. J. Hailey, R. Laher, K. Madsen, E. Nakar, P. E. Nugent, D. Stern, M. Sullivan, J. Surace, and W. W. Zhang

2014. SN 2010jl: Optical to Hard X-Ray Observations Reveal an Explosion Embedded in a Ten Solar Mass Cocoon. *ApJ*, 781:42.

Osterbrock, D. E. and G. J. Ferland

2006. *Astrophysics of Gaseous Nebulae and Active Galactic Nuclei*, 2nd edition. University Science Books.

Patat, F., E. Cappellaro, J. Danziger, P. A. Mazzali, J. Sollerman, T. Augusteijn, J. Brewer, V. Doublier, J. F. Gonzalez, O. Hainaut, C. Lidman, B. Leibundgut, K. Nomoto, T. Nakamura, J. Spyromilio, L. Rizzi, M. Turatto, J. Walsh, T. J. Galama, J. van Paradijs, C. Kouveliotou, P. M. Vreeswijk, F. Frontera, N. Masetti, E. Palazzi, and E. Pian

2001. The Metamorphosis of SN 1998bw. *ApJ*, 555(2):900–917.

Patat, F., S. Taubenberger, S. Benetti, A. Pastorello, and A. Harutyunyan

2011. Asymmetries in the type IIn SN 2010jl. *A&A*, 527:L6.

Reilly, E., J. R. Maund, D. Baade, J. C. Wheeler, J. M. Silverman, A. Clocchiatti, F. Patat, P. Höflich, J. Spyromilio, L. Wang, and P. Zelaya

2016. Spectropolarimetry of the Type Ib supernova iPTF 13bvn: Revealing the complex explosion geometry of a stripped-envelope core-collapse supernova. *MNRAS*, 457(1):288–303.

Rybicki, G. B. and A. P. Lightman

1986. *Radiative Processes in Astrophysics*. Wiley.

Salamanca, I., R. J. Terlevich, and G. Tenorio-Tagle

2002. The circumstellar material around SN IIn 1997eg: another detection of a very narrow P Cygni profile. *MNRAS*, 330(4):844–854.

Schinzel, F. K., G. B. Taylor, C. J. Stockdale, J. Granot, and E. Ramirez-Ruiz

2009. SN 2001em: Not So Fast. *ApJ*, 691(2):1380–1386.

Serkowski, K.

1973. Interstellar Polarization. In *Interstellar Dust and Related Topics*, J. M. Greenberg and H. C. van de Hulst, eds., volume 52 of *IAU Symposium*, P. 145.

Smartt, S. J.

2009. Progenitors of Core-Collapse Supernovae. *ARA&A*, 47(1):63–106.

Smith, N.

2016. Interacting Supernovae: Types IIn and Ibn. ArXiv e-prints. arXiv:1612.02006.

Smith, N., R. Chornock, W. Li, M. Ganeshalingam, J. M. Silverman, R. J. Foley, A. V. Filippenko, and A. J. Barth

2008. SN 2006tf: Precursor Eruptions and the Optically Thick Regime of Extremely Luminous Type IIn Supernovae. *ApJ*, 686(1):467–484.

Smith, N., W. Li, A. V. Filippenko, and R. Chornock

2011a. Observed fractions of core collapse supernova types and initial masses of their single and binary progenitor stars. *MNRAS*, 412(3):1522–1538.

Smith, N., W. Li, J. M. Silverman, M. Ganeshalingam, and A. V. Filippenko

2011b. Luminous blue variable eruptions and related transients: diversity of progenitors and outburst properties. *MNRAS*, 415(1):773–810.

Smith, N., J. M. Silverman, R. Chornock, A. V. Filippenko, X. Wang, W. Li, M. Ganeshalingam, R. J. Foley, J. Rex, and T. N. Steele

2009. Coronal Lines and Dust Formation in SN 2005ip: Not the Brightest, but the Hottest Type IIn Supernova. *ApJ*, 695(2):1334–1350.

Stephens, M. A.

1974. Edf statistics for goodness of fit and some comparisons. *Journal of the American Statistical Association*, 69:730–737.

Stevance, H. F., J. R. Maund, D. Baade, P. Höflich, F. Patat, J. Spyromilio, J. C. Wheeler, A. Clocchiatti, L. Wang, Y. Yang, and P. Zelaya

2016. Spectropolarimetry of the Type IIb SN 2008aq. *MNRAS*, 461(2):2019–2024.

Stoll, R., J. L. Prieto, K. Z. Stanek, R. W. Pogge, D. M. Szczygieł, G. Pojmański, J. Antognini, and H. Yan

2011. SN 2010jl in UGC 5189: Yet Another Luminous Type IIn Supernova in a Metal-poor Galaxy. *ApJ*, 730:34.

Tan, P., M. Steinbach, and V. Kumar

2005. Addison-Wesley.

Tanaka, M., K. Maeda, P. A. Mazzali, K. S. Kawabata, and K. Nomoto

2017. Three-Dimensional Explosion Geometry of Stripped-Envelope Core-Collapse Supernovae. II. Modelling of Polarization. *ApJ*, 387(2):105.

Tinsley, B. M.

1975. What stars become supernovae. *PASP*, 87(520):837.

Turatto, M.

2003. Classification of Supernovae. In *Supernovae Gamma-Ray Bursters*, K. Weiler, ed., volume 598 of *Lecture Notes in Physics, Berlin Springer Verlag*, Pp. 21–36.

Turatto, M., S. Benetti, and E. Cappellaro

2003. Variety in Supernovae. In *From Twilight to Highlight: The Physics of Supernovae*, W. Hillebrandt and B. Leibundgut, eds., P. 200.

Turatto, M., S. Benetti, and A. Pastorello

2007. Supernova classes and subclasses. In *Supernova 1987A: 20 Years After: Supernovae and Gamma-Ray Bursters*, S. Immler, K. Weiler, and R. McCray, eds., volume 937 of *AIPConf.Proc.*, Pp. 187–197.

Van Dyk, S. D., P. M. Garnavich, A. V. Filippenko, P. Höflich, R. P. Kirshner, R. L. Kurucz, and P. Challis

2002. The Progenitor of Supernova 1993J Revisited. *PASP*, 114(802):1322–1332.

Van Dyk, S. D., W. Li, and A. V. Filippenko

2003. On The Progenitor of the Type II-Plateau Supernova 2003gd in Messier 74. *PASP*, 115(1996):1289–1295.

van Genderen, A. M.

2001. S Doradus variables in the Galaxy and the Magellanic Clouds. *A&A*, 366:508–531.

Vink, J. S.

2012. Eta Carinae and the Luminous Blue Variables. In *Eta Carinae and the Supernova Impostors*, K. Davidson and R. M. Humphreys, eds., volume 384 of *Astrophysics and Space Science Library*, P. 221.

Vink, J. S., T. J. Harries, and J. E. Drew

2005. Polarimetric line profiles for scattering off rotating disks. *A&A*, 430:213–222.

Wang, L. and J. C. Wheeler

2008. Spectropolarimetry of supernovae. *ARA&A*, 46(1):433–474.

Wang, L., J. C. Wheeler, and P. Höflich

1997. Polarimetry of the Type IA Supernova SN 1996X. *ApJ*, 476(1):L27–L30.

Whitney, B. A.

2011. Monte Carlo radiative transfer. *BASI*, 39:101–127.

Wood, K., B. A. Whitney, and J. Bjorkman

1996. Introduction to Monte Carlo Radiation Transfer.

Yoshida, T., H. Umeda, K. Maeda, and T. Ishii

2016. Mass ejection by pulsational pair instability in very massive stars and implications for luminous supernovae.

Zhang, T., X. Wang, C. Wu, J. Chen, J. Chen, Q. Liu, F. Huang, J. Liang, X. Zhao, L. Lin, M. Wang, M. Dennefeld, J. Zhang, M. Zhai, H. Wu, Z. Fan, H. Zou, X. Zhou, and J. Ma

2012. Type IIn Supernova SN 2010jl: Optical Observations for over 500 Days after Explosion. *AJ*, 144:131.

Zwicky, F.

1964. Basic results of the international search for Supernovae. *Ann. dAstr*, 27:300.

Appendix A

Model grid distribution figures

This appendix presents additional figures from the sets discussed in Chapters 3 and 4 containing the distribution of central-source model grid fits to SN 1997eg and SN 2010jl. The plots examine how the fits are driven by the various parameter values as a function of the amount of vertical polarization shifting and the ratio of flux emission in the line to that in the continuum.

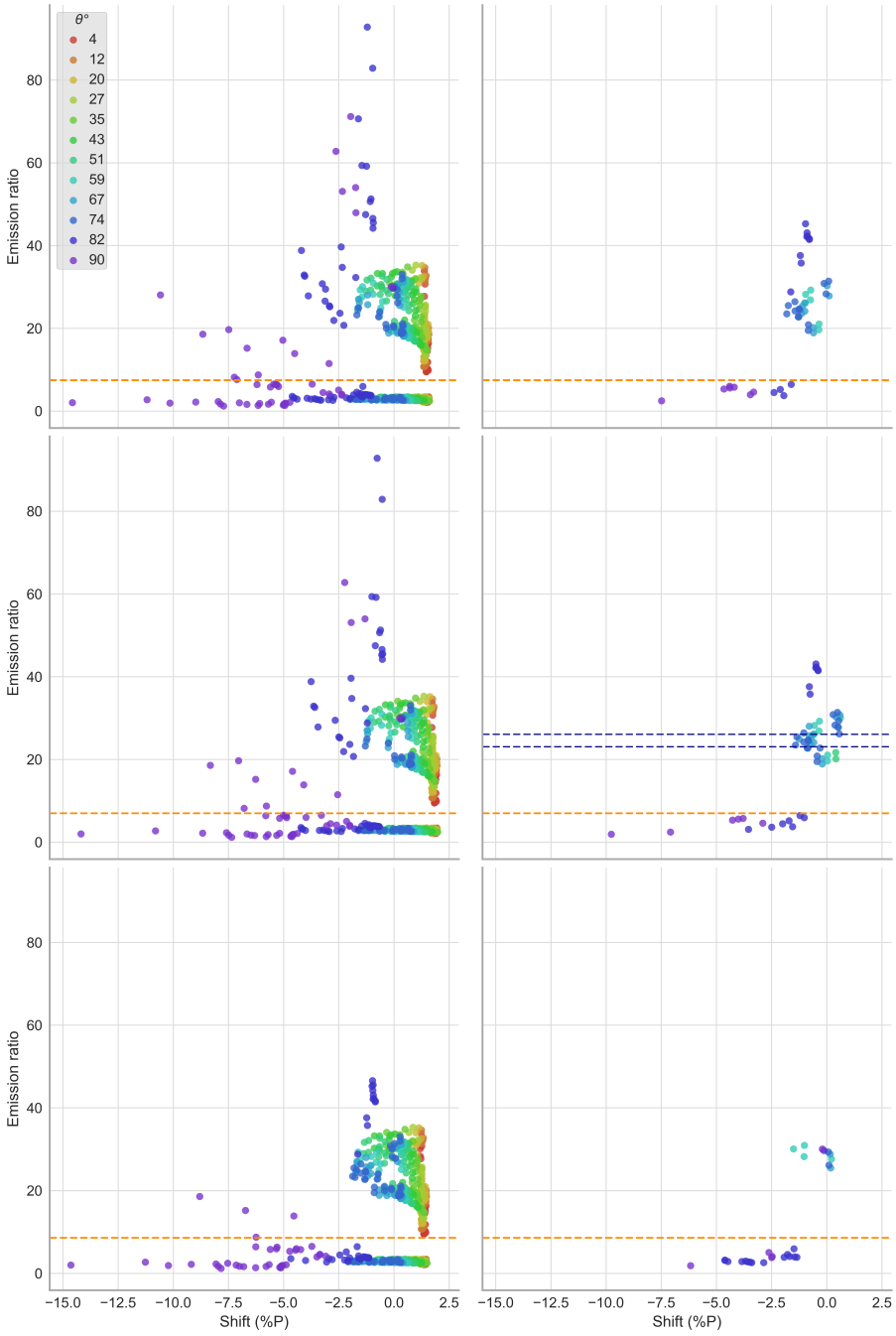

Figure A.1: Inclination of central model grid fits for all three epochs (top to bottom) of SN 1997eg, plotted as polarization shift vs flux emission ratio. Models in the low χ^2_ν cluster are plotted in the right column. The orange dashed lines mark the emission ratio of observed data. The blue dashed lines mark the range of emission ratios for models where the excess intensity at the line core closely matches the intensity deficit in the intermediate line. No model meeting this criteria was identified for Epoch 3.

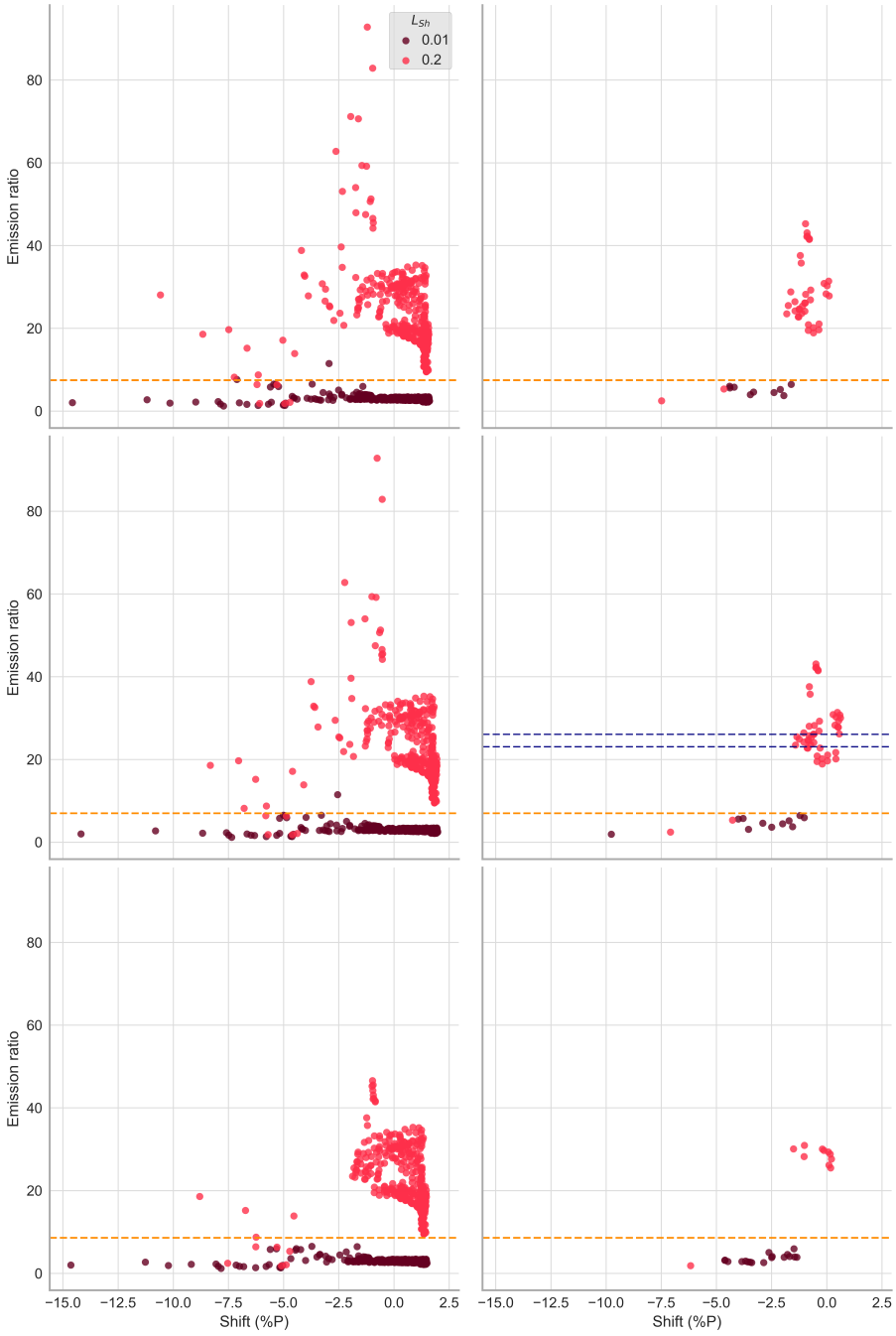

Figure A.2: Inclination of central-source model fits for all three epochs (top to bottom) of SN 1997eg, plotted as polarization shift vs. flux emission ratio. Models in the low χ^2_ν cluster are plotted in the right column. The orange dashed lines mark the emission ratio of observed data. The blue dashed lines mark the range of emission ratios for models where the excess intensity at the line core closely matches the intensity deficit in the intermediate line. No model meeting these criteria was identified for Epoch 3.

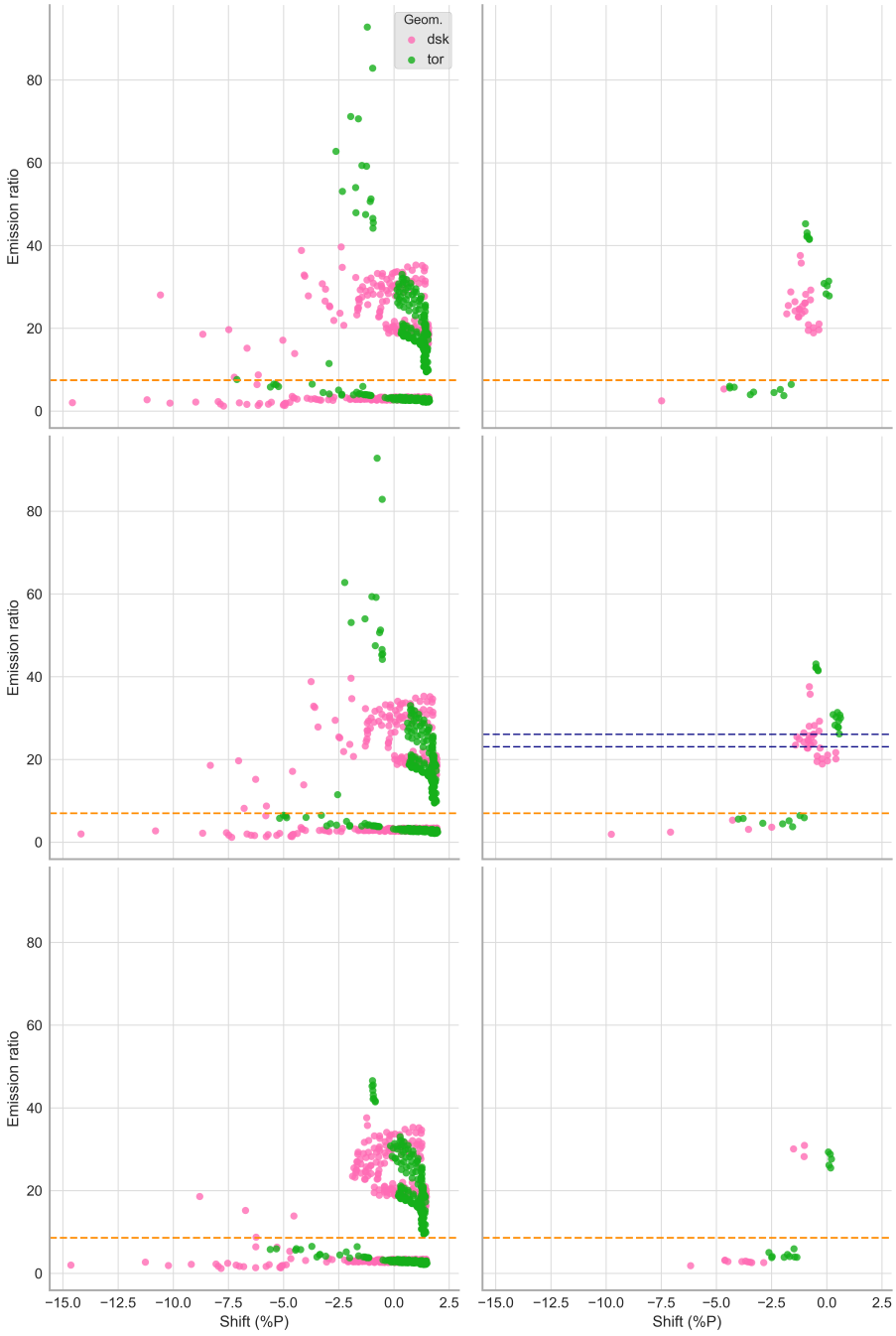

Figure A.3: Inclination of central-source model fits for all three epochs (top to bottom) of SN 1997eg, plotted as polarization shift vs. flux emission ratio. Models in the low χ^2_ν cluster are plotted in the right column. The orange dashed lines mark the emission ratio of observed data. The blue dashed lines mark the range of emission ratios for models where the excess intensity at the line core closely matches the intensity deficit in the intermediate line. No model meeting these criteria was identified for Epoch 3.

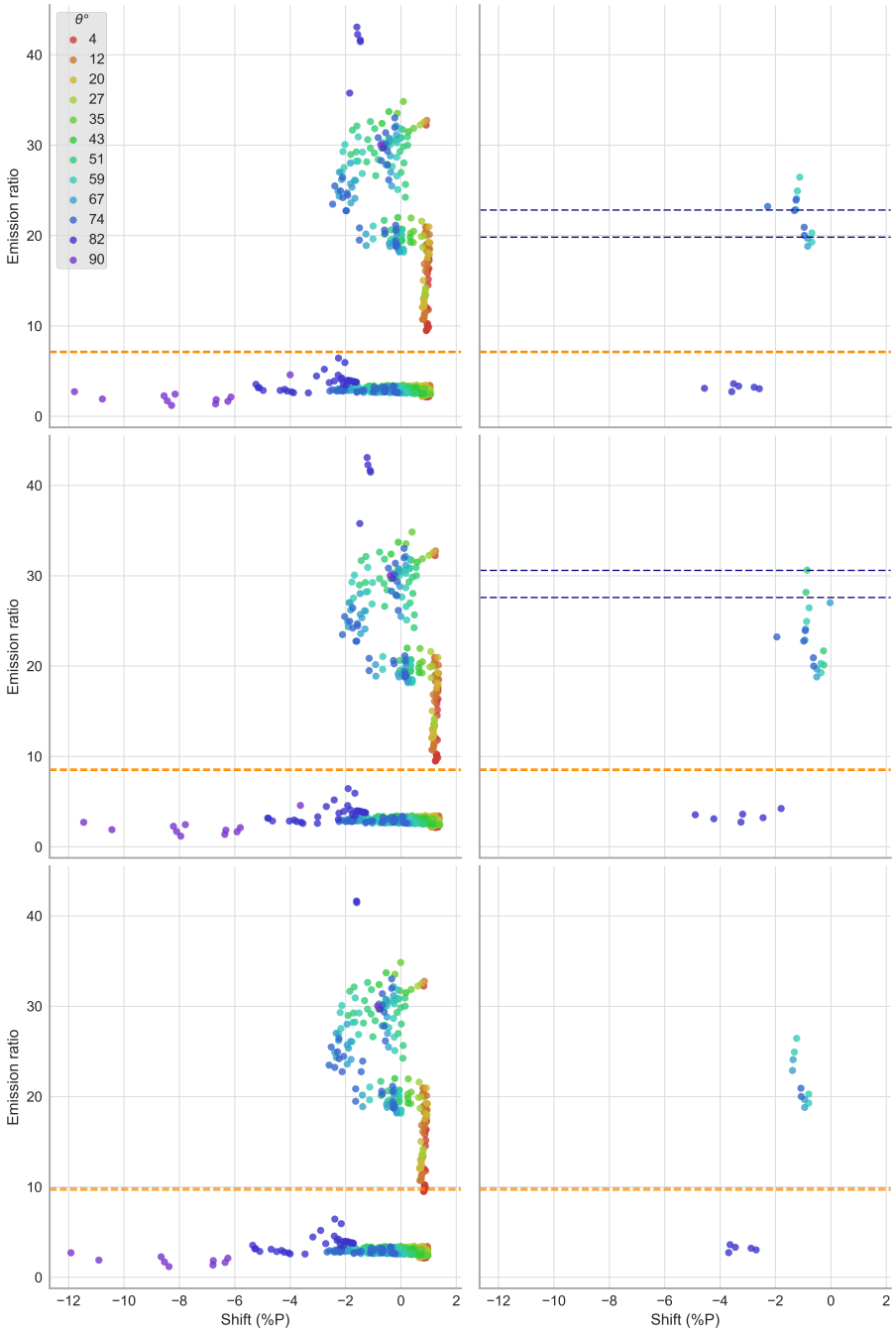

Figure A.4: Inclination of central-source model fits for all three epochs (top to bottom) of SN 2010jl, plotted as polarization shift vs. flux emission ratio. Models in the low χ^2_ν cluster are plotted in the right column. The orange dashed lines mark the emission ratio of observed data. The blue dashed lines mark the range of emission ratios for models where the excess intensity at the line core closely matches the intensity deficit in the intermediate line. No model meeting these criteria was identified for Epoch 3.

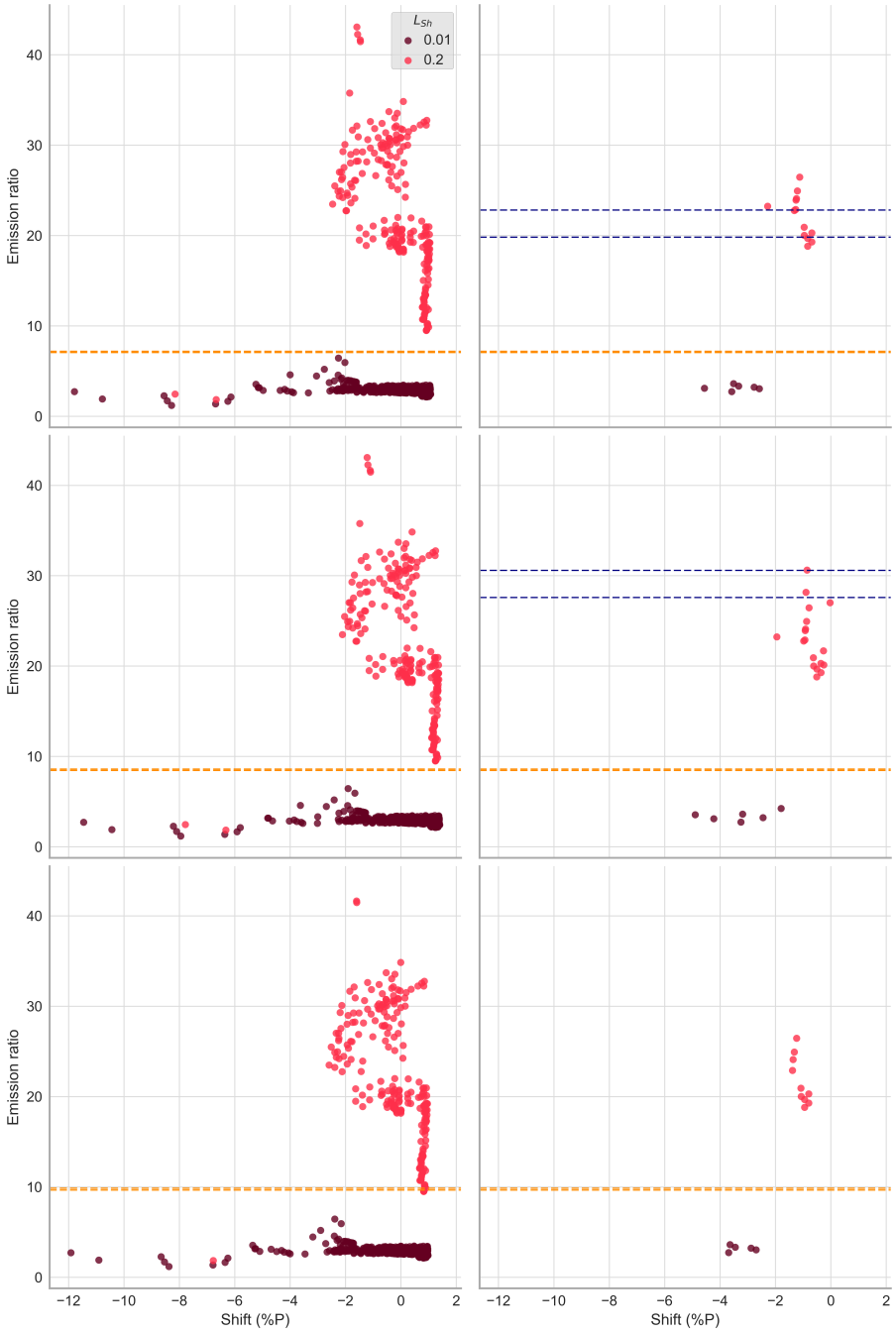

Figure A.5: Inclination of central-source model fits for all three epochs (top to bottom) of SN 2010jl, plotted as polarization shift vs. flux emission ratio. Models in the low χ^2_ν cluster are plotted in the right column. The orange dashed lines mark the emission ratio of observed data. The blue dashed lines mark the range of emission ratios for models where the excess intensity at the line core closely matches the intensity deficit in the intermediate line. No model meeting these criteria was identified for Epoch 3.

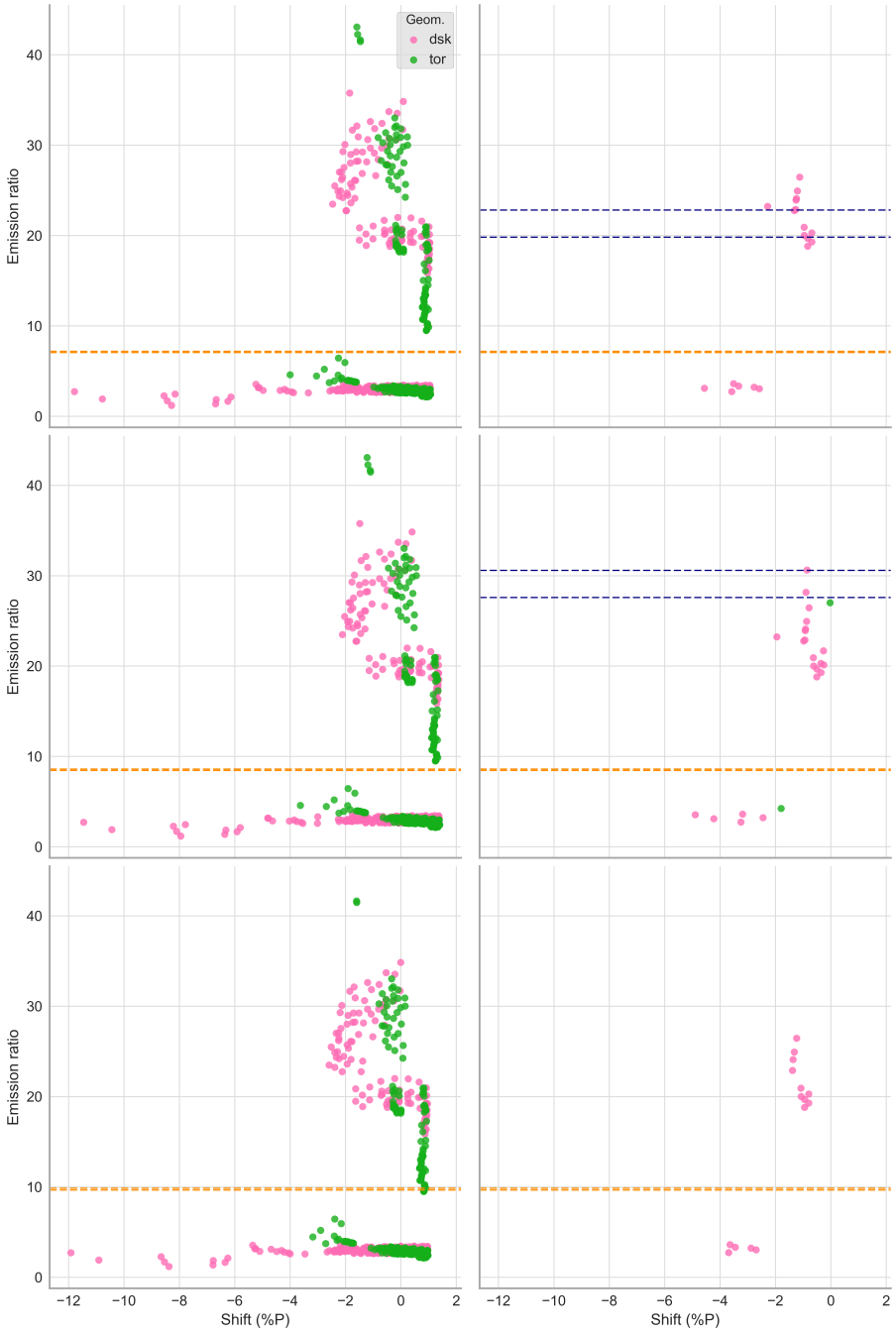

Figure A.6: Inclination of central-source model fits for all three epochs (top to bottom) of SN 2010jl, plotted as polarization shift vs. flux emission ratio. Models in the low χ^2_ν cluster are plotted in the right column. The orange dashed lines mark the emission ratio of observed data. The blue dashed lines mark the range of emission ratios for models where the excess intensity at the line core closely matches the intensity deficit in the intermediate line. No model meeting these criteria was identified for Epoch 3.

Appendix B

FORTRAN application: Discrete binning of narrow Gaussian spectral lines

This appendix contains the *SLIP* subroutine augmented for proper discretization of emission lines arising from the shock and CSM regions of the models. Emission lines arising from a warm gas are broadened by the thermal kinetic motion of the particles. These lines are described by a continuous Gaussian function ϕ_λ

$$\phi_\lambda = \frac{1}{\sigma\sqrt{2\pi}}\, e^{\frac{-(\lambda_0-\lambda)^2}{2\sigma^2}} \qquad \text{where } \sigma = \frac{\lambda_0}{c}\sqrt{\frac{2kT}{m}}$$

centered on the rest wavelength of the atomic transition λ_0, and a full width at half-maximum $\Delta\lambda = 2\sqrt{2\ln 2}\sigma$ that depends on the velocity distribution of the material and in this case depends on the composition and temperature of the gas.

This Gaussian line shape is a continuous distribution, but my models and all observational data are measured using wavelength bins of discrete width, the resolution of which depends on the instrument. I chose a resolution of 5 Å to match

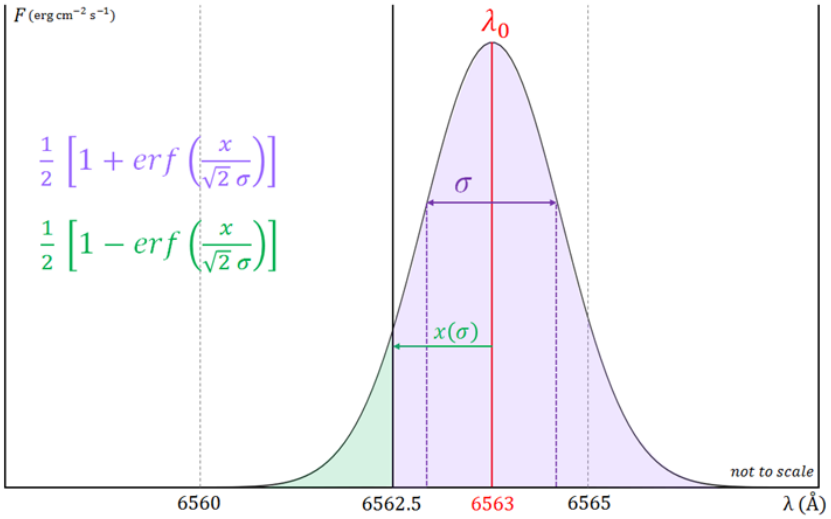

Figure B.1: Emission lines with a continuous Gaussian profile must be discretized when they fall near the boundary separating two wavelength bins. When bisected at a fractional σ distance from its center, a Gaussian is split into regions each with area determined by the *erf* function.

the resolution of the observational data for SN 1997eg. In my models, the rest wavelength of Hα, 6563 Å lies very close to the edge of one of these bins and the energy contained in it must be correctly distributed between them. This is achieved by calculating the area under the partial Gaussians on either side of the bin edge, as seen in Fig. B.1. The area is found from 2 *erf* functions calculated using the distance between the bin edge and rest wavelength as a fraction of σ.

```
 subroutine hemnew

!Reads in H diffuse emission table from "hinew.in", interpolates
!in log space to get appropriate spectrum for input temperature.
!"hdiff" array has first frequency (decreasing), then T=500K, 1000K,
!etc., as in hinew. No interpolation in this version; instead setting
!input T to closest temperature.

!Reads in and interpolates H line emission coefficients from "hlnew.in",
!updated for higher T from Pengelly; interpolation OK here, esp at
!higher T.

!Combines all H contributions into one spectrum, at the same resolution
!as the input stellar spectrum.

!2005/04/20 (jlh) written
!2005/04/22 (jlh) added spectrum interpolation (see sampspec.f)
!2005/07/29 (jlh) added line emission coefficients
!2005/08/15 (jlh) combined spectral components
!2012/05/30 (jlh) copied from hi.in and updated for new table
!2017/02/22 (lnh) area method to discretize Gaussian line intensity

 implicit none

 common /mpivar/ mytid, nproc,ierr
 integer :: mytid, nproc,ierr

 include 'ds.txt'
 include 'opacin.txt'

```

```
 real*8 tk,tkp,tk2(8),dtk,ldiff,fdiff,frac,fl1,larr(5,8),hbeta(7)
 real*8 pi,cms,line(5,nlin),fspec(nlin),fedge(nlin+1),l1,l2,stk
 real*8 stkp,edge,area,distl(nlin+1),x1

 real tfer(12),tdiff,ctfer
 integer i,j,k,l,iopar,ilines,jt,distmin(1),distint

 character sfile*15,lfile*15
 data iopar /11/

 pi=4.d0*datan(1.d0)
 cms=3.d8

! the first half of this routine has been removed for brevity
! this second half contains the new method to
! discretize the Gaussian emission line intensities

! create an array of the bin edge locations
 fedge(nlin+1)=cms*1.d10/(specin(1,nlin)+2.5d0)
 do i=1,nlin
   fspec(i)=cms*1.d10/specin(1,i)
   fedge(i)=cms*1.d10/(specin(1,i)-2.5d0)
 end do

 do l=1,5
  ! find the bin edge that each line center is closest to
   do i=1,nlin
      line(l,i)=0.d0
      distl(i)=abs(balmer(l,3)-fedge(i))
   end do
```

```
61    distl(nlin+1)=abs(balmer(l,3)-fedge(nlin+1))
62    distmin=minloc(distl)
63    distint=distmin(1)
64    edge=fedge(distint)
65    x1=distl(distint)
66
67   !calculate the area between the distances -x1 and +x1
68    area=erf((2.d0*x1*sqrt(log(2.d0)))/balmer(l,4))
69
70   ! if the line is within the bounds of the spectrum, do this:
71   ! if line is less than edge i, bin i gets "less" and i-1 gets "more"
72    if ((balmer(l,3).lt.maxval(fedge)).and.(balmer(l,3).gt.
73  &     minval(fedge))) then
74       if (distint.eq.1) then
75            line(l,distint)=line(l,distint)+0.5d0*(1.d0+area)
76         else if (distint.eq.(nlin+1)) then
77            line(l,distint-1)=line(l,distint-1)+0.5d0*(1.d0+area)
78       else
79            if (balmer(l,3).lt.edge) then
80               line(l,distint)=line(l,distint)+0.5d0*(1.d0+area)
81               line(l,distint-1)=line(l,distint-1)+0.5d0*(1.d0-area)
82            else
83            line(l,distint)=line(l,distint)+0.5d0*(1.d0-area)
84            line(l,distint-1)=line(l,distint-1)+0.5d0*(1.d0+area)
85            end if
86        end if
87    else
88
89   ! if the line is outside the spectrum it must lie within a
90   ! a bin width for partial inclusion in the bounding bins
```

```
91       if (distint.eq.1) then
92          if (x1.gt.(fedge(1)-fedge(2))) then
93             go to 42
94            else
95              line(l,distint)=line(l,distint)+0.5d0*(1.d0-area)
96            end if
97            else if (distint.eq.(nlin+1)) then
98              if (x1.gt.(fedge(nlin)-fedge(nlin+1))) then
99             go to 42
100             else
101            line(l,distint)=line(l,distint)+0.5d0*(1.d0-area)
102             end if
103           end if
104      end if
105
106 42     continue
107      ! Emission strength coefficient factored in
108       do i=1,nlin
109        if (line(l,i).gt.0.d0) then
110           line(l,i)=line(l,i)*balmer(l,5)
111        end if
112       end do
113
114  end do
115
116 !balmer line components all added to continuum
117  do i=1,nlin
118    hspec(i)=nspeche(2,i)+line(1,i)+line(2,i)+line(3,i)
119 &          +line(4,i)+line(5,i)
120  end do
```

Appendix C

Python and IDL routines for data analysis

This appendix contains code I wrote for the model reduction and analysis process. I wrote the first routine, ModelVariant.pro, in IDL for the purpose of evaluating whether the level of uncertainty for a given model was low enough to compare against observed data and other models. I developed the second routine, dochigridPol.py, in Python from a routine originally written in IDL. It utilizes the numpy and xarray packages to handle simultaneous calculations on the 8-dimensional array created from every model in each grid regime. Xarray, like the pandas package, allows for named slicing and indexing of large datasets, but supports higher dimensionality. This routine contains sections for data reduction and selection as well as the χ^2 fits, and utilizes the scipy package for outlier removal and the hierarchical clustering algorithm, as well as the seaborn package for visualization.

```
pro ModelVariant,model,path,epoch

# this routine creates a noise model of each model polarization spectrum
# drawn a Gaussian distribution based on the uncertainties at each point
# to test the stability of the resulting chi-square values

path= 'C:\Users\Desktop\'
file= path + model+'_40-f.out'
efile= path + model+'_40-ef.out'

ofile='C:\Users\Desktop\Research\observedspectrum.txt'
readcol,ofile,waveo,Io,Qo,Qoe,Uo,Uoe,/silent

fitvec=fltarr(12,2)
binvec=intarr(12,1)

first=4
eps=[19,20,20]
last=eps(epoch-1)

;determine degrees of freedom
points = last-first
params = 1
dof = points - params -1

for bin=1,12 do begin

  sk=4+((bin-1)*27)
  readcol,file,cost,wave,I,Q,U,V,skipline=sk,numline=27,/silent
  readcol,efile,cost,wave,Ie,Qe,Ue,Ve,skipline=sk+1,numline=27,/silent
```

```
31
32    wave=wave(first:last) & cost=cost(first:last)
33    I=I(first:last) & Q=Q(first:last) & U=U(first:last)
34    Ie=Ie(first:last) & Qe=Qe(first:last) & Ue=Ue(first:last)
35
36    Pgrid = fltarr(n_elements(Qe),1001)
37    Pegrid = fltarr(n_elements(Qe),1001)
38
39    P = sqrt(Q^2+U^2)
40    Pe = sqrt((Qe*Q)^2+(Ue*U)^2)/P
41
42    Po = sqrt(Qo^2+Uo^2)
43    Poe = sqrt((Qoe*Qo)^2+(Uoe*Uo)^2)/Po
44
45    ;make the variation distribution for each data point
46
47    PVar = findgen(n_elements(P))
48    ModelVar = fltarr(n_elements(PVar),1001)
49
50    for k = 0,1000 do begin
51            if k eq 0 then begin
52              ModelVar(*,0)=P
53      endif else begin
54              randomvec = fltarr(n_elements(P))
55                     for j = 0,n_elements(P)-1 do begin
56                        randomvec(j) = randomu(seed, /NORMAL)
57                        PVar(j) = P(j) + (randomvec(j) * Pe(j) )
58                        ModelVar(j,k) = PVar(j)
59           endfor
60             endelse
61    endfor
```

```
62
63    ;calculate chi2 between variations in array and data
64
65    chi2Var=fltarr(1000)
66
67    range=(Max(Po)-Min(Po))
68    normgrid1=(findgen(201)/200.) * range
69    normgrid2=(findgen(201)/(-200.)) * range
70    normgrid=[normgrid2,normgrid1]
71    normgrid=normgrid[SORT(normgrid)]
72
73    chi2grd=findgen(n_elements(normgrid))
74
75  for k = 0,999 do begin
76          for m = 0,n_elements(chi2grd)-1 do begin
77              resids = ModelVar(*,k) - (Po + normgrid(m))
78              eresids = Poe
79              chi2 = total((resids/eresids)^2)
80              chi2grd(m) = chi2
81      endfor
82
83      chi2 = min(chi2grd,c)
84      chi2nu = chi2/dof
85      norm = normgrid(c)
86
87      resids = Po-(ModelVar(*,k)+norm)
88      eresids = Poe
89      Residuals = resids/eresids
90
91      chi2Var(k) = chi2nu
92
```

```
93      fitvec(bin-1,0) = chi2Var(0)
94      fitvec(bin-1,1) = stddev(chi2Var)
95          endfor
96  endfor
97
98  ;print variation chi2 values to console
99  for bin=1,12 do print, fitvec(bin-1,0)
100         print, ''
101         print,'rchi2 std. dev'
102         for bin=1,12 do print, fitvec(bin-1,1)
103       print,''
104       print,'original rchi2: '+strtrim(chi2Var(0),2)
105       print,'minimum rchi2: '+strtrim(min(chi2Var),2)
106       print,'maximum rchi2: '+strtrim(max(chi2Var),2)
107       print,'mean rchi2: '+strtrim(mean(chi2Var),2)
108       print,'standard dev rchi2: '+strtrim(stddev(chi2Var),2)
109
110 end
```

```
# dochigridPol.py
import numpy as np
import xarray as xr
import seaborn as sns
import Ffunctions
import Sfunctions
from scipy import stats
from scipy.cluster.hierarchy import fcluster, set_link_color_palette
from scipy.cluster.hierarchy import dendrogram, linkage
from collections import OrderedDict

SN = 'SN 1997eg'
regime = 'dist'
eps = [1,2,3]

resolution = np.array([5,40])
geometry = np.array(['dsk','tor'])
tau = np.array(['05','1','2'])
ncsm = np.array(['0','1'])
temp = np.array(['10','20','50'])
bins = np.arange(1,13,1)
thetas = np.ones(len(bins))*(0.99767,0.97908,0.94226,0.88789,0.81697,0.73084,
                             0.63109,0.51958,0.39840,0.26980,0.13617,0.00000)
deg  = np.round( (np.arccos(thetas) * (180./np.pi)), 0)

for z in range(0,len(eps)):
    epoch = eps[z]
    if regime == 'central':
        nsh = np.array(['01','2'])
    if regime == 'dist':
        nsh =  np.array(['100'])

        n_geom = len(geometry)
```

```
34          n_tau = len(tau)
35          n_ncsm = len(ncsm)
36          n_nsh = len(nsh)
37          n_temp = len(temp)
38          n_thet = len(bins)
39          n_models = n_geom * n_tau * n_ncsm * n_nsh * n_temp * n_thet
40
41      for r in range(0,len(resolution)):
42          if resolution[r] == 5:
43              n_lin = 217
44              npoints = 121
45          if resolution[r] == 20:
46              n_lin = 53
47              npoints = 31
48          if resolution[r] == 40:
49              n_lin = 27
50              npoints = 16
51
52              n_lines = (np.arange(0,npoints)*resolution[r])+6150
53          n_lam = (np.arange(0,n_lin)*resolution[r])+5950
54          n_total = n_lin * n_t
55
56          # Read in observed files, insert into arrays ###
57          obs_columns= ['lambda','I','Ie','Q','Qe','U','Ue','P','Pe','v']
58          obsfile = FFunctions.findobsfile(SN,epoch,resolution[r])
59
60          obsdata = FFunctions.readinObs(obsfile)
61          obspolcol = SFunctions.computeP(
62                      obsdata[:,3],obsdata[:,4],obsdata[:,5],obsdata[:,6])
63          vocol = SFunctions.vspace(obsdata[:,0],6563.)
64          obssheet = np.column_stack((obsdata,obspolcol[0],obspolcol[1],vocol
65
66          modelsheet = np.zeros((n_total,12))
```

```
67          modelcube = np.zeros((n_geom,n_tau,n_ncsm,n_nsh,n_temp,n_thet,n_lin,12))
68          shifts = np.zeros((n_geom,n_tau,n_ncsm,n_nsh,n_temp,n_thet))
69
70          if resolution[r] == 5:
71              obsframe = xr.DataArray(obssheet,
72                                      coords=[n_lines,obs_columns],
73                                      dims=['wave','spectra'])
74          if resolution[r] == 40:
75              obsframe_40 = xr.DataArray(obssheet,
76                                      coords=[n_lines,obs_columns],
77                                      dims=['wave','spectra'])
78
79          # Read in all model files, insert into arrays
80          # Read in column data for models, stacked by theta viewing angle
81          i,j,k,l,m,n = 0,0,0,0,0,0
82
83          for i in range (0,n_geom):
84             for j in range (0,n_tau):
85                 for k in range (0,n_ncsm):
86                     for l in range (0,n_nsh):
87                         for m in range (0,n_temp)
88
89                             root = FFunctions.findmodelfile(
90                                    geometry[i], tau[j], ncsm[k], nsh[l], temp[m])
91                             if resolution[r] == 5:
92                                 model = root
93                             else:
94                                 model = root + '_'+str(resolution[r])
95
96                             sheet = FFunctions.readinModel(path,model,n_total)
97                             polcol = SFunctions.computeP(sheet[:,4], sheet[:,5],
98                                      sheet[:,6], sheet[:,7])
99                             vcol = SFunctions.vspace(sheet[:,1],6563.)
```

```
100                         angle  = np.round( np.arccos(sheet[:,0]) * (180./np.pi), 0)
101                         modelsheet = np.column_stack((sheet, polcol[0], polcol[1],
102                                     vcol, angle))
103
104                       # unstack angle bins, place in 'n' dimension
105                         for n in range (0, n_thet):
106                                 modelname = root + '-' + str(bins[n])
107                                 specsheet = np.zeros((n_lin, modelsheet.shape[1]))
108                                 specsheet = FFunctions.binchop(
109                                       modelsheet, n, n_total, thetas)
110
111                         # insert individual bin spectra into cube of data
112                           modelcube[i,j,k,l,m,n,:,:] = specsheet[:,:]
113
114         columns = ['cost','lambda','I','Ie','Q','Qe','U','Ue','P','Pe','v','angle']
115         if resolution[r] == 5:
116             modelframe = xr.DataArray(modelcube,
117             coords=[geometry,tau,ncsm,nsh,temp,bins,n_lam,columns],
118             dims=['geometry','tau','ncsm','nsh','temp','incbin','wave','spectra'])
119         if resolution[r] == 40:
120             modelframe_40 = xr.DataArray(modelcube,
121             coords=[geometry,tau,ncsm,nsh,temp,bins,n_lam,columns],
122             dims=['geometry','tau','ncsm','nsh','temp','incbin','wave','spectra'])
123
124     ###============================================================================###
125
126     # stack models into single dimension of model name (i,j,k,l,m,n) for ease of
127     # processing over all dimensions
128     modelstack = modelframe.stack(
129                 Nmodel=('geometry','tau','ncsm','nsh','temp','incbin'))
130     modelstack_40 = modelframe_40.stack(
131                    Nmodel=('geometry','tau','ncsm','nsh','temp','incbin'))
132
```

```
    # normalize flux in 5A spectra
    fac = (obsframe.sel(spectra='I').isel(wave=0) /
           modelstack.sel(spectra='I').isel(wave=0)).drop('spectra')
    modelstack.loc[dict(spectra='I')] = modelstack.sel(spectra='I') * fac
    modelstack.loc[dict(spectra='Ie')]= modelstack.sel(spectra='Ie') * fac

    # trim all models to same wavelength range as observed data - 16 data points
    modelstack = modelstack.where( (modelstack.wave >= 6150.)
                                & (modelstack.wave <= 6750.) , drop=True)
    modelstack_40 = modelstack_40.where( (modelstack_40.wave >= 6150.)
                                & (modelstack_40.wave <= 6750.) , drop=True)

    # set models to the bluest point of observed data by shifting in P
    specshift = (obsframe.sel(spectra=tofit).isel(wave=0)
               - modelstack.sel(spectra=tofit).isel(wave=0))
    modelstack.loc[dict(spectra=tofit)] = (
                   modelstack.sel(spectra=tofit) + specshift)
    sigshift = np.sqrt(
               (obsframe.sel(spectra='Pe').isel(wave=0))**2
             + (modelstack.sel(spectra='Pe').isel(wave=0))**2)

    specshift40 = (obsframe_40.sel(spectra=tofit).isel(wave=0)
                 - modelstack_40.sel(spectra=tofit).isel(wave=0) )
    modelstack_40.loc[dict(spectra=tofit)] = (
                  modelstack_40.sel(spectra=tofit) + specshift40)
    sigshift40 = np.sqrt(
                (obsframe_40.sel(spectra='Pe').isel(wave=0))**2
              + (modelstack_40.sel(spectra='Pe').isel(wave=0))**2)

    specshift = specshift.drop('wave').drop('spectra')
    specshift40 = specshift40.drop('wave').drop('spectra')
    sigshift = sigshift.drop('wave').drop('spectra')
    sigshift40 = sigshift40.drop('wave').drop('spectra')
```

```
166
167     # remove wavelength points we don't wish to include in the fit
168     # intermediate width line from +/- 1000 to 3000 km/s
169     BN_modelstack = modelstack.where(
170                     (abs(modelstack.sel(spectra='v').isel(Nmodel=0)) >= 3000.)|
171                     (abs(modelstack.sel(spectra='v').isel(Nmodel=0)) <= 1000.),
172                     drop=True)
173     BN_obsframe   = obsframe.where(
174                     (abs(obsframe.sel(spectra='v')) >= 3000.)|
175                     (abs(obsframe.sel(spectra='v')) <= 1000.),
176                     drop=True)
177     BN_modelstack_40 = modelstack_40.where(
178                     (abs(modelstack_40.sel(spectra='v').isel(Nmodel=0)) >= 3000.)|
179                     (abs(modelstack_40.sel(spectra='v').isel(Nmodel=0)) <= 1000.),
180                     drop=True)
181     BN_obsframe_40 = obsframe_40.where(
182                     (abs(obsframe_40.sel(spectra='v')) >= 3000.)|
183                     (abs(obsframe_40.sel(spectra='v')) <= 1000.),
184                     drop=True)
185
186   # remove enchanced blue scattering wing region only for SN 1997eg
187   # Iron line in 5A models only
188         if SN == 'SN 1997eg':
189             BN_modelstack = BN_modelstack.where(
190                         (BN_modelstack.sel(spectra='v').isel(Nmodel=0) > -8587.00)|
191                         (BN_modelstack.sel(spectra='v').isel(Nmodel=0) < -8817.00),
192                         drop=True)
193         BN_obsframe = BN_obsframe.where(
194                         (BN_obsframe.sel(spectra='v') > -8587.00)|
195                         (BN_obsframe.sel(spectra='v') < -8817.00),
196                         drop=True)
197         BN_obsframe = BN_obsframe.where(
198                         (BN_obsframe.sel(spectra='lambda') > 6430)|
```

```
                    (BN_obsframe.sel(spectra='lambda') < 6350),
                    drop=True)
        BN_modelstack = BN_modelstack.where(
                     (BN_modelstack.sel(spectra='lambda').isel(Nmodel=0) > 6430)|
                     (BN_modelstack.sel(spectra='lambda').isel(Nmodel=0) < 6350),
                     drop=True)
        BN_modelstack_40=BN_modelstack_40.where(
                     (BN_modelstack_40.sel(spectra='lambda').isel(Nmodel=0)>6430)|
                     (BN_modelstack_40.sel(spectra='lambda').isel(Nmodel=0)<6350),
                     drop=True)
        BN_obsframe_40 = BN_obsframe_40.where(
                      (BN_obsframe_40.sel(spectra='lambda') > 6430)|
                      (BN_obsframe_40.sel(spectra='lambda') < 6350),
                      drop=True)

        dof5 = len(BN_modelstack.wave) - params - 1
        dof40 = len(BN_modelstack_40.wave) - params - 1

    ###=========================================================================###

    # perform chisquare fitting
    tofit ='P'
        dof = len(BN_modelstack_40.wave) - params - 1
        allF = BN_modelstack_40.sel(spectra=tofit)
        allFcoords = allF.coords
        allF = allF.drop('spectra')
        allFe = BN_modelstack_40.sel(spectra=(tofit+'e')).isel(wave=0)
        allFe = allFe.drop('spectra')

    Fo = BN_obsframe_40.sel(spectra=tofit)
    Fo = Fo.drop('spectra')
    Foe = BN_obsframe_40.sel(spectra=(tofit+'e'))
    Foe = Foe.drop('spectra')
```

```
232
233     nshift = 200.
234     shiftrange =  np.max(Fo) - np.min(Fo)
235     eshift = np.sqrt( (np.max(Foe)**2) + (np.min(Foe)**2) )
236     shiftgrid = (np.arange(-nshift,nshift,1.0) / nshift)
237     ngrid = xr.DataArray( shiftgrid,
238            dims='shifts',
239            coords=[np.arange(0,len(shiftgrid),1)] )*shiftrange
240     resids  = Fo - (allF + ngrid)
241     eresids = Foe
242
243     R = resids/eresids
244     c = (resids/eresids)**2
245     grid = c.sum(dim='wave')
246
247     minloc = grid.argmin('shifts')
248     chi2grid = grid.min(dim='shifts')      # lowest shifted chi2
249     rchi2grid = chi2grid / dof40           # lowest rchi2
250
251     norm = np.zeros( (len(minloc)) )
252     for n in range ( 0, len(minloc) ):
253         norm[n] = float( ngrid[ int(minloc[n]) ] )
254     norms = xr.DataArray(norm, coords=chi2grid.coords)
255
256     #R = R.transpose('wave','spectra','Nmodel')
257     Residuals = np.zeros( (len(R.wave), len(minloc) ) )
258     ad = np.zeros(( len(minloc) ))
259     acrit = np.zeros((len(minloc),5))
260     asig = np.zeros((len(minloc),5))
261     for n in range ( 0, len(minloc) ):
262         oneresid = R.sel(shifts=minloc[n]).isel(Nmodel=n).drop('shifts')
263         Residuals[:,n] = oneresid[:]
264         ad[n] = (stats.anderson(Residuals[:,n], 'norm')[0])
```

```
265             acrit[n,:] = (stats.anderson(Residuals[:,n], 'norm')[1])
266             asig[n,:] = (stats.anderson(Residuals[:,n], 'norm')[2])
267         residuals = xr.DataArray(Residuals, coords=allFcoords)
268         residuals = xr.concat([residuals], dim='spectra')
269         A2 = xr.DataArray(ad, coords=chi2grid.coords)
270         Acrit = acrit[0]
271         Asig = asig[0]
272 
273         BNmodelstack_40 = xr.concat( [BN_modelstack_40, residuals], dim='spectra')
274         BNmodelstack_40['spectra'] = (['cost','lambda','I','Ie','Q','Qe','U','Ue',
275                                        'P','Pe','v','angle','residuals'])
276 
277         ###============================================================================###
278 
279         # calculate emission ratios and estimate excess narrow line intensity
280         allI = BN_modelstack.sel(spectra='I')
281         allI = allI.drop('spectra')
282         allIe = BN_modelstack.sel(spectra='Ie')
283         allIe = allIe.drop('spectra')
284 
285         Io = BN_obsframe.sel(spectra='I')
286         Io = Io.drop('spectra')
287         Ioe = BN_obsframe.sel(spectra=('Ie'))
288         Ioe = Ioe.drop('spectra')
289 
290         Aex = ((allI.loc[6560] - BN_obsframe.sel(spectra='I').loc[6560])
291              + (allI.loc[6565] - BN_obsframe.sel(spectra='I').loc[6565] )
292                ).drop('spectra')
293         sigAex = np.sqrt(
294                  (allIe.loc[6560])**2
295                 +(BN_obsframe.sel(spectra='Ie').loc[6560])**2
296                 + (allIe.loc[6565])**2
297                 +(BN_obsframe.sel(spectra='Ie').loc[6565])**2 )
```

```
298       a = (BN_obsframe.sel(spectra='I').loc[6540:6555]
299          - allI.loc[6540:6555] )
300       siga = np.sqrt(
301             (BN_obsframe.sel(spectra='Ie').loc[6540:6555]**2).sum(dim='wave')
302            +(allIe.loc[6540:6555]**2).sum(dim='wave') )
303       b = (BN_obsframe.sel(spectra='I').loc[6570:6600]
304          - allI.loc[6570:6600] )
305       sigb = np.sqrt(
306             (BN_obsframe.sel(spectra='Ie').loc[6570:6600]**2).sum(dim='wave')
307            +(allIe.loc[6570:6600]**2).sum(dim='wave')  )
308
309       Aint = (a.sum('wave') + b.sum('wave')).drop('spectra')
310       sigAint = np.sqrt( siga**2 + sigb**2  )
311       Adiff = Aex-Aint
312       sigAdiff = np.sqrt( sigAex**2 + sigAint**2 ).drop('spectra').drop('wave')
313
314       # determine emission line ratio using all 10 first points
315       Iratio = allI.sel(wave=6565.) / allI.isel(wave=slice(0,10))
316       Ieratio = np.abs(Iratio) * np.sqrt(
317                (allIe.isel(wave=slice(0,10))/allI.isel(wave=slice(0,10)))**2
318              + (allIe.sel(wave=6565.)/allI.sel(wave=6565.))**2 )
319       Ioratio = Io.sel(wave=6565.) / Io.isel(wave=slice(0,10))
320       Ioeratio = np.abs(Ioratio) * np.sqrt(
321                 (Ioe.isel(wave=slice(0,10))/Io.isel(wave=slice(0,10)))**2
322               + (Ioe.sel(wave=6565.)/Io.sel(wave=6565.))**2 )
323
324       Iratio = Iratio.mean(dim='wave')
325       Ieratio = (1.0/10.0)*np.sqrt( (Ieratio**2).sum(dim='wave'))
326       Ioratio = Ioratio.mean(dim='wave')
327       Ioeratio = (1.0/10.0)*np.sqrt( (Ioeratio**2).sum(dim='wave'))
328
329       Ioplus = Ioratio+Ioeratio+1
330       Iominus = Ioratio-Ioeratio-1
```

```
331     print Ioratio, Ioeratio
332
333     sig = np.where( np.logical_and(Iratio<Ioplus, Iratio>Iominus) ==True)
334
335     ###============================================================================###
336
337     # order grid of fit information for each model by reduced chi-square value
338     fitgrid = xr.concat([chi2grid, rchi2grid, specshift, norms, totalshift,
339                          sigshift, Iratio, Ieratio, A2, Aex, Aint, Adiff, sigAdiff],
340                          dim='fitinfo')
341     fitgrid['fitinfo'] = (['chi2','rchi2','norm','shift','total','sigtotal','ratio',
342                            'sigratio','A2', 'Aex', 'Aint', 'Adiff','sigAdiff'])
343     fitgrid2 = fitgrid.where(fitgrid.sel(fitinfo = 'chi2') != 0.0, drop=True)
344
345     models     = (modelstack.where(fitgrid2.sel(fitinfo = 'chi2')
346               != 0.0, drop=True).drop('fitinfo') )
347     models40   = (modelstack_40.where(fitgrid2.sel(fitinfo = 'chi2')
348               != 0.0, drop=True).drop('fitinfo') )
349     modelsBN   = (BN_modelstack.where(fitgrid2.sel(fitinfo = 'chi2')
350               != 0.0, drop=True).drop('fitinfo') )
351     models40BN = (BNmodelstack_40.where(fitgrid2.sel(fitinfo = 'chi2')
352               != 0.0, drop=True).drop('fitinfo') )
353
354     minimize = fitgrid2.sel(fitinfo = 'rchi2').argsort()
355
356     fitgrid_sort = fitgrid2.isel(Nmodel = minimize)
357     models = models.isel(Nmodel = minimize)
358     models40 = models40.isel(Nmodel = minimize)
359     modelsBN = modelsBN.isel(Nmodel = minimize)
360     models40BN = models40BN.isel(Nmodel = minimize)
361
362     critchi = stats.chi2.isf(q=0.05,df=dof)
363     critrchi2 = critchi/dof
```

```
364     significant = fitgrid_sort.where(
365                 (fitgrid_sort.sel(fitinfo='chi2') <= critchi), drop=True)
366
367     ###============================================================================###
368
369     # populations of models based on hierarchical clustering of reduced chi-square
370     # function to find outliers that are too high to consider for clustering
371     def MADs(y,thresh):
372       # warning: this function does not check for NAs nor does it address
373       # issues when more than 50\% of your data have identical values
374       m = np.median(y)
375
376       ## uncomment for 2 sided
377       # abs_dev = np.abs(y - m)
378       # left_mad = np.median(abs_dev[y <= m])
379       # right_mad = np.median(abs_dev[y >= m])
380       # y_mad = left_mad * np.ones(len(y))
381       # y_mad[y > m] = right_mad
382
383       ## uncomment for 1 sided values above median
384       abs_dev = 1e-10* np.ones(len(y))
385       abs_dev[y > m] = np.abs(y[np.where(y > m)] - m)
386       right_mad = np.median(abs_dev[y >= m])
387       y_mad = np.ones(len(y))
388       y_mad[y > m] = right_mad
389
390       modified_z_score = 0.6745 * abs_dev / y_mad
391       modified_z_score[y == m] = 0
392       return modified_z_score > thresh
393
394     # plots a dendrogram with distances and heights plotted at junctions
395     def fancy_dendrogram(*args, **kwargs):
396             max_d = kwargs.pop('max_d', None)
```

```
397         if max_d and 'color_threshold' not in kwargs:
398                 kwargs['color_threshold'] = max_d
399         annotate_above = kwargs.pop('annotate_above', 0)
400 
401         ddata = dendrogram(*args, **kwargs)
402 
403         if not kwargs.get('no_plot', False):
404                 plt.title('Hierarchical Clustering Dendrogram (truncated)')
405                 plt.xlabel('sample index or (cluster size)')
406                 plt.ylabel('distance')
407             for i, d, c in zip(ddata['icoord'],ddata['dcoord'],ddata['color_list']):
408                     x = 0.5 * sum(i[1:3])
409                     y = d[1]
410                     if y > annotate_above:
411                         plt.plot(x, y, 'o', c=c)
412                         plt.annotate("\%.3g" \% y, (x, y), xytext=(0, -5),
413                                 textcoords='offset points',
414                                 va='top', ha='center')
415             if max_d:
416                     plt.axhline(y=max_d, c='k')
417             return ddata
418 
419     # remove outliers from fit values
420     chi2s = fitgrid_sort.sel(fitinfo='rchi2').values
421     outlier = MADs(chi2s,3.5)
422     outliers = chi2s[outlier]
423     inliers = chi2s[np.where(outlier==False)]
424     cut = (outliers.min() + inliers.max())/2
425 
426     palette = sns.xkcd_palette(['cornflower','dark pastel green','salmon',
427              'golden yellow','liliac','pale orange','light teal','pale brown'])
428     palette = (palette)+(palette)
429 
```

```
    # create linkage matrix using UPGMC 'centroid' method
    set_link_color_palette(map(rgb2hex,  palette[1:])) # palette[2:None:-1]))
    inliers = np.reshape(inliers,(-1,1))
    Z1 = linkage(inliers, 'centroid')

    # plot dendrogram for user input on cutoff distance
    fig = plt.figure(figsize=(8.5, 5)) #
    gs=gridspec.GridSpec(1,1)
    ax9 = plt.subplot(gs[0])
    fancy_dendrogram(Z1, truncate_mode='lastp', p=40, leaf_rotation=45.,
                     show_contracted=True, annotate_above=2)
    plt.show()
    cutoff = input('choose cutoff: ')
    plt.close()

    # determine the number of clusters, locations in group belonging to each,
    # the cutoff fit value separating the low cluster and their min/max/avg.
    # if either of the edge clusters have only one or two models, merge them
    # with their closest neighbor
    clusters = fcluster(Z1, cutoff, criterion='distance')
    n = list(OrderedDict((element, None) for element in clusters))
    n = np.array((n))
    clusters2 = np.array(clusters)

    if len(clusters2[np.where(clusters2 == n[0])]) <= 4:
        if len(clusters2[np.where(clusters2 == n[1])]) <= 4:
            clusters2[np.where(clusters2 == n[1])] = n[2]
            clusters2[np.where(clusters2 == n[0])] = n[2]
            N = np.array(n[2:])
        else:
            clusters2[np.where(clusters2 == n[0])] = n[1]
            N = np.array(n[1:])
    elif len(clusters2[np.where(clusters2 == n[len(n)-1])]) <= 3:
```

```
463         clusters2[np.where(clusters2 == n[len(n)-1])] = n[len(n)-2]
464         N = np.array(n[:(len(n)-2)])
465     else:
466         N = np.array(n)
467     Nmod = np.zeros((len(N)))
468     C = np.zeros((len(inliers),len(N)))
469     means = np.zeros((len(N)))
470     minmax = np.zeros((len(N),2))
471 
472     for i in range(len(N)):
473             C[:,i] = (clusters2 == N[i])
474             Nmod[i] = len(clusters2[np.where(clusters2 == N[i])])
475             means[i] = np.mean(inliers[np.where(clusters2==N[i])])
476             minmax[i,:] = np.min(inliers[np.where(clusters2==N[i])]),
477                       np.max(inliers[np.where(clusters2==N[i])])
478     lowest = int( (np.where(minmax[:,0] == minmax[:,0].min()))[0])
479     lowcut = minmax[lowest,1]
480     lowchi2s = inliers[np.where(inliers <= lowcut)]
```